

# Incommensurate Valence Bond Density Waves in the Glassy Phase of Underdoped Cuprates

Author: Liang Ren Niestemski

Persistent link: <http://hdl.handle.net/2345/2626>

This work is posted on [eScholarship@BC](#),  
Boston College University Libraries.

---

Boston College Electronic Thesis or Dissertation, 2011

Copyright is held by the author, with all rights reserved, unless otherwise noted.

Boston College

The Graduate School of Arts and Sciences  
Department of Physics

INCOMMENSURATE VALENCE  
BOND DENSITY WAVES IN THE  
GLASSY PHASE OF UNDERDOPED  
CUPRATES

A Dissertation by  
LIANG REN NIESTEMSKI

submitted in partial fulfillment of the requirements for  
the degree of Doctor of Philosophy

May 2011

© *Copyright 2011 by Liang Ren Niestemski*

# Incommensurate Valence Bond Density Waves in the Glassy Phase of Underdoped Cuprates

Liang Ren Niestemski

Advisor: Ziqiang Wang

## Abstract

One of the most unconventional electronic states in high transition temperature cuprate superconductors is the pseudogap state. In the temperature versus doping phase diagram, the pseudogap state straddles across the antiferromagnetic (AF) state near half filling and the superconducting (SC) dome on the hole doped side above the transition temperature  $T_c$ . The relationship between the pseudogap state and these two well known states - the AF state and the SC state is believed to be very important for understanding superconductivity and the emergent quantum electronic matter in doped Mott insulators. The pseudogap is characterized by the emergence of a soft gap in the single-particle excitation spectrum in the normal state in the temperature range between  $T_c$  and a characteristic temperature  $T^*$ , i.e.  $T_c < T < T^*$ . The most puzzling feature of the pseudogap is the nodal-antinodal dichotomy. Observed by ARPES in momentum space, the Fermi surface is gapped out in the antinodal region leaving a Fermi arc of gapless excitations near the nodes. Whether the pseudogap is an incoherent superconducting gap (one-

gap scenario) or it is a different gap governed by other mechanisms, other than superconductivity, (two-gap scenario) is still under debate. In this thesis I study the particle-particle channel and the particle-hole channel of the valence bond fluctuations away from half filling. Based on a strong-coupling analysis of the  $t - J$  model, I argue that the superexchange interaction  $J$  induced incommensurate bond centered density wave order is the driving mechanism for the pseudogap state. Low energy density of states (DOS) are eliminated by multiple incommensurate scatterings in the antinodal region at the Fermi level. I show that the interplay between the incommensurate bond centered d-wave density wave instability and the intrinsic electronic inhomogeneity in real cuprate materials is responsible for the observed pseudogap phenomena. Utilizing the spatially unrestricted Gutzwiller approximation, I show that the off-stoichiometric doping induced electrostatic disorder pins the low-energy d-wave bond density fluctuations, resulting in a VBG phase. The antinodal Fermi surface (FS) sections are gapped out, giving rise to a genuine normal state Fermi arc. The length of the Fermi arc shrinks with underdoping below the temperature  $T^*$  determined by thermal filling of the antinodal pseudogap. Below  $T_c$ , the d-wave superconducting gap due to singlet pairing coexists and competes with the VBG pseudogap. The spatial, momentum, temperature and doping dependence of these two gaps are consistent with recent ARPES and STM observations in underdoped and chemically substituted cuprates. The temperature versus doping phase diagram captures the salient properties of the pseudogap phenomena and provides theoretical

support for the two-gap scenario. In addition to resolving the complexities of the quantum electronic states in hole-doped cuprates, my unified theory elucidates the important role of the interplay between the strong electronic correlation and the intrinsic electronic disorder in doped transition metal oxides.

*For my family*

---

# Contents

<b>Abstract</b>	<b>ii</b>
<b>Acknowledgements</b>	<b>x</b>
<b>Preface</b>	<b>xii</b>
<b>1 Introduction</b>	<b>1</b>
1.1 The Very Beginning . . . . .	1
1.2 The Discovery of the Superconductor . . . . .	1
1.3 Cuprates-the Copper Family of High Temperature Supercon- ductors . . . . .	6
1.3.1 Crystal Structure of Cuprates . . . . .	6
1.3.2 Electronic Structure of Cuprates . . . . .	8
1.4 A Mystery in Cuprates: The Pseudogap Phenomena . . . . .	11
1.4.1 What is a Pseudogap . . . . .	11
1.4.2 Pseudogap Experimental Evidence: First Experiments	12
1.4.3 Pseudogap Experimental Evidence: ARPES . . . . .	15

1.4.4	Pseudogap Experimental Evidence: STM . . . . .	21
1.4.5	Pseudogap Experimental Evidence: Specific Heat . . . . .	24
1.4.6	Pseudogap Experimental Evidence: Raman Scattering . . . . .	26
1.5	The Origin of the Pseudogap State . . . . .	28
1.5.1	One-Gap Scenario . . . . .	29
1.5.2	Two-Gap Scenario . . . . .	31
1.5.3	My Concentration . . . . .	31
<b>2</b>	<b>Renormalized Mean Field Theory for High <math>T_c</math> Cuprates</b>	<b>33</b>
2.1	Emergence of the t-J Model . . . . .	33
2.1.1	Three-Band p-d Model . . . . .	34
2.1.2	From the Two-Band Model to Effective One-Band t-J Model . . . . .	37
2.2	The Renormalized Mean Field Method with Gutzwiller Ap- proximation . . . . .	41
2.2.1	Uniform Gutzwiller Approximation . . . . .	42
2.2.2	Spatially Unrestricted Gutzwiller Approximation . . . . .	43
2.2.3	The Mean Field Decoupling of $\mathbf{S} \cdot \mathbf{S}$ Superexchange Term in the t-J Model . . . . .	50
2.2.4	The Renormalized Mean Field Hamiltonian with SUGA . . . . .	54
2.2.5	Two Valence Bond Channels with the Same Origin Become Different Away from Half Filling . . . . .	55

2.3	The Bridge Between the Theory and Experiment – Using Retarded Green’s Function to Describe One Particle Properties as Seen in Experiments . . . . .	58
<b>3</b>	<b>The Incommensurate Bond Density Wave State of Cuprates</b>	<b>65</b>
3.1	The Visualization of Bond Density Waves in Cuprates . . . . .	65
3.2	Incommensurate Multiple Scattering in Underdoped Cuprates	68
3.3	Renormalized Mean Field Hamiltonian in Momentum Space .	74
3.4	Uniform Normal State without Symmetry Breaking . . . . .	84
3.5	Commensurate Bond Density Wave State . . . . .	90
3.6	The Emergence of the Fermi Arc: From the Commensurate Bond Density Wave State to the Incommensurate Bond Density Wave State . . . . .	93
3.7	Doping Dependence of the Incommensurate Bond Density Wave State . . . . .	96
3.8	Nematic Order and Symmetry Breaking . . . . .	99
<b>4</b>	<b>Valence Bond Glass Theory in the Pseudogap Regime</b>	<b>102</b>
4.1	Interplay of Incommensurate Valence Bond Order and Electronic Disorder . . . . .	102
4.2	Unified Theory of the Doping Induced Electronics Disorder and the Incommensurate Bond Density Wave Pseudogap States . . . . .	108

4.3	Extended t-J Model with Spatially Unrestricted Gutzwiller Approximation . . . . .	109
4.4	Normal State and Pseudogap Phase . . . . .	115
4.4.1	The Fermi Arc and “V” Shaped Density of States . . . . .	115
4.4.2	Understanding the Role of Disordered Potential . . . . .	119
4.4.3	Doping Dependence of the Pseudogap . . . . .	121
4.4.4	Temperature Dependence of the Pseudogap . . . . .	124
4.4.5	Nodal Antinodal Dichotomy in the Spectral Function . . . . .	125
4.4.6	Quantitative Evaluation of the Glassy Bond Order and the Pseudogap . . . . .	127
4.5	Superconducting Phase . . . . .	129
4.5.1	The First Glance of the Coexistence of Two Gaps . . . . .	130
4.5.2	Temperature Dependence of the Pseudogap and the Superconducting Gap . . . . .	132
4.5.3	The Momentum Dependence of the Two Coexisting Gaps	133
4.5.4	The Spatial Dependence of the Two Gaps . . . . .	137
4.5.5	The Theoretical Phase Diagram . . . . .	138
<b>A From Hubbard Model to t-J Model</b>		<b>140</b>
<b>Bibliography</b>		<b>144</b>

# Acknowledgements

*Years ago I came to Boston College in pursuit of knowledge, but looking back I realize that I have captured much more. I would like to acknowledge the people who have been part of my life during these years at Boston College. Without them, this part of my journey would not be complete. Some of them nurtured me with their mentorship and some of them guided me with their insightful advice. Some of them warmed my heart with their friendship, some of them helped me with their selfless gestures and some of them supported me without any doubts. I am truly thankful to all of them.*

*First I would like to thank my advisor Professor Ziqiang Wang. He is everything I aspire to be as a physicist. He is always there for me with his knowledge, guidance and his insight. He encouraged me to take on tough tasks and pushed me through difficulties. He inspired me with his passion for physics and shaped my mind with challenges. I am grateful to be his student. Besides my advisor, I also want to thank all the professors I know at Boston College especially Professor Madhavan, Professor Ding, and Professor Padilla for fruitful discussions on cuprates and various research projects.*

*Their experimental data also provided me the ultimate test for my theory. I am thankful to Professor Graf and Professor Ren who accommodated me in their labs during the summers. I also want to thank all the professors who taught me in class and whom I worked for as a teaching assistant: Professor Herczynski, Professor Broido, Professor Kalman, Professor Kempa, Professor Bedell, Professor Di Bartolo, Professor Engelbrecht, and Professor Uritam.*

*During the years, I have made great friends in Boston College. I shared not only my office and work, but also stories and laughs with my research group members: Sen Zhou, Chunhua Li, Meng Gao, Feng Cai, Yuanming Lu. I have many joyful memories with them and my other fellow graduate students and their families.*

*There is one person I would like to thank especially, my husband, Francis. He supports me with his love and he supports my theory with his good experimental data! Lastly, I want to thank my parents. It is their unconditional support and love that makes me who I am.*

*I dedicate this thesis to my dear family.*

# Preface

Parts of this thesis are based on unpublished and published articles by myself in collaboration with others.

## Chapter 3:

Liang Ren Niestemski, Ziqiang Wang. **Incommensurate Bond Density Wave State in Underdoped Cuprates** Unpublished version

## Chapter 4:

Liang Ren Niestemski, Ziqiang Wang. **Valence Bond Glass Theory of Electronic Disorder and the Pseudogap State of High-Temperature Cuprate Superconductors** Phys. Rev. Lett. 102, 107001 (2009)

[Link to published paper](#)

# Chapter 1

## Introduction

### 1.1 The Very Beginning

Most materials can be classified by the band theory of solids. For a particular material, if band theory predicts a gap then the material is likely an insulator. There are notable exceptions though where the band theory of solids fails though. In the quantum hall state the material is an insulator without a gap. For strongly correlated systems, sometimes the gap defines the material and sometimes not, the gap must be interpreted. In this thesis I will introduce and explain a specific type of gap, the pseudogap, and talk about its interpretation in the field of high transition temperature superconductivity - a typical strongly correlated electronic system.

### 1.2 The Discovery of the Superconductor

The history of the superconductor is very rich and has taken several interesting turns since it was first discovered by Kammerlingh Onnes in 1911. Indeed, the initial discovery itself is wrapped in legend. The discovery of helium liquification allowed resistance measurements to be taken at temperatures never taken before (4 K and lower). It was proposed that at the lowest temperatures these materials would exhibit insulating properties. The first

observations did not show insulating behavior however, but an anomalous zero resistance. At first observation of this zero resistance state in mercury it has been told that the reading was blamed on equipment failure (perhaps the common thing to attribute a surprising result to). Later it became clear that this truly was a zero resistance phenomena and a new state of matter. This was the discovery of superconductivity. Superconductivity can loosely be defined as a zero resistance state below some critical temperature known as  $T_c$ . Above  $T_c$  no superconductivity exists, that temperature is high enough to destroy the superconductivity. It was also found that superconductors have a relationship with magnetic field. Meissner subjected superconductors to strong magnetic fields and noticed that the magnetic fields were be expelled. This perfect diamagnetism exists up to a limit of magnetic field strength,  $H_c$ , and is a trait of all superconductors. Because of this fact, no field can exist within the inside volume of a superconductor (as long as the field is less than  $H_c$ . [1]). Though Meissner's discovery was and important the microscopic mechanism for what makes superconductivity possible was still a mystery at that point.

In 1935, brothers Fritz and Heinz London began to work on some theory to shed insight on this superconducting phenomena. Though phenomenological, these so called London equations were able to describe the magnetic field expulsion witnessed by Meissner [2]. Fifteen years later, another phenomenological theory was proposed by Ginzburg and Landau. This theory is based largely on thermodynamic arguments. One important aspect of this theory is the study of the properties of a superconducting material with respect to temperature. Two major successes of these Ginzburg Landau equations are in the parametrization of the characteristic quantities: the coherence length and the penetration depth. The coherence length relates to the size of thermodynamic fluctuations in the material while the penetration depth refers to the depth in which magnetic fields can penetrate. [3]. Though relevant this was not a microscopic theory and offers no insight into the inner workings of

what makes a superconductor function.

The microscopic theory was eventually tackled by the team of J.Bardeen, L.N. Cooper, and J.R.Schrieffer in the mid 1950's. This is considered to be one of the most important contributions in condensed matter physics in the last century. For this theory they would win the Nobel prize. Under this theoretical frame work, electrons form two electron pairs which have come to be called Cooper pairs after the founder. This pairing is stable and energetically favorable to two separate electrons. To break these cooper pairs apart actually requires some energy. ( $\Delta$  is half the energy needed to break this cooper pair). This pairing is brought on by an attractive interaction, due to the virtual exchange of phonons. This pairing turns two fermions of opposite spin and momentum into an effective boson free to condense into a coherent ground state. This coherent state is superconductive. This created framework fully and unambiguously explains the observed loss of electrical resistance [4].

Probably what helped the BCS team realize the true nature of pairing was the specific heat data taken on vanadium. It's exponential dependence pointed to an absence of electrons at certain energies in the electronic density of states [5]. This so called energy gap was surprising. It was unclear where these electrons went and why they went at all. At present, in the case of mercury, lead and the other materials the BCS team studied, it is well known that this gap is a consequence of pairing. ( I will soon discuss that this is not the case with all superconducting materials.) All of the electrons centered  $\Delta$  radius from the Fermi energy disappear in the single particle density of states. They have disappeared since they do not contribute to the specific heat measurement. They are, of course, still in the material. They are now just paired up and now synthetic bosons.

At the time of its discovery, the BCS solution was indeed good for all superconductors and the previous question was thought to be answered: The gap does imply pairing. This certainty would change though. About thirty

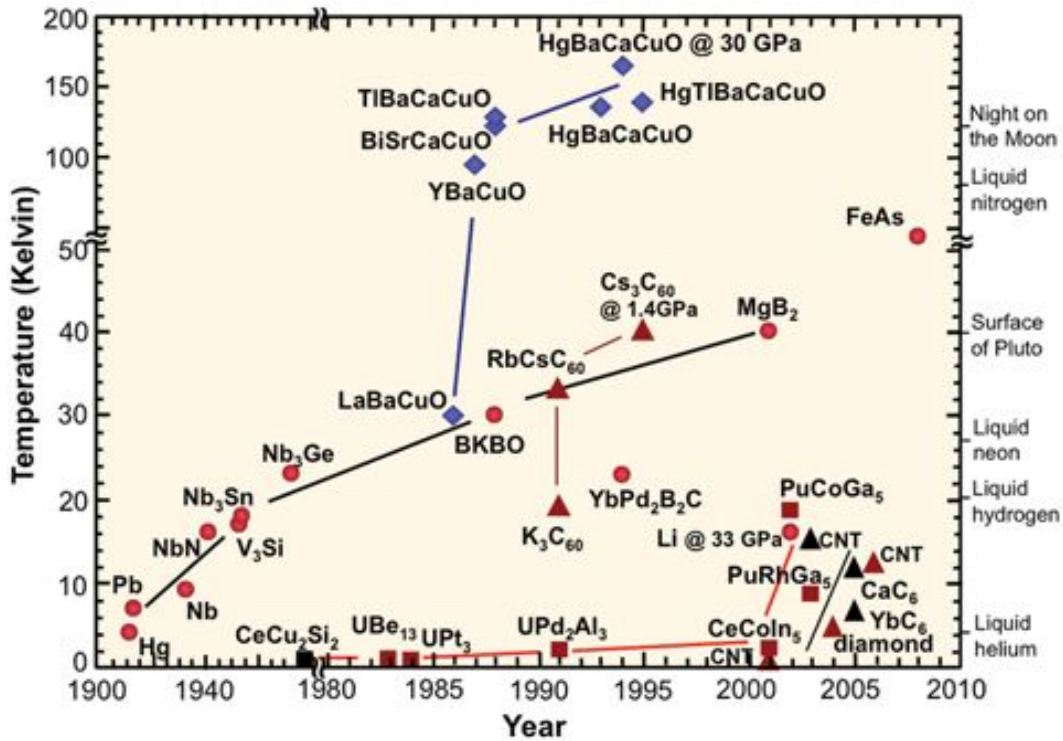


Figure 1.1: A road map of discoveries in superconductivity, from <http://www.ccas-web.org/img/superconductivity/sc0.gif>

years later a surprising result shocked the community. In 1986, Benorcz and Muller discovered a new phenomenon in the material lanthanum barium copper oxide (LBCO)[6]. With sufficient chemical doping, the critical temperature of this material could reach as high as 35 K. Soon later in 1987, M.K.Wu et al. found superconductivity in a similar material, only hotter, with a transition temperature of 90K (well above liquid nitrogen temperature) [7]. Why is this fascinating? It is because it was generally accepted that McMillan's theory was true and that the maximum  $T_c$  a material could have was around 40 K [8]. So at 90 K (more than twice McMillan's prediction and almost five times more than the previous  $T_c$  record holder) it was clear something was drastically different. Perhaps it is Mother Nature's joke on the world but it

seems that the record holder for the highest transition temperature superconductivity comes from a ceramic (an insulator). No current theories were equipped to explain this strange fact. These discoveries kindled a whole new era of study about this general class of materials referred to as high transition temperature ( $T_c$ ) superconductors .

The past two and a half decades have shown an extreme effort and satisfactory progress into the field of high  $T_c$ , but unfortunately the most fundamental questions have not been answered. As more materials were developed, more theories were developed. With more materials certain commonalities were formed. What these materials had in common were they were all were made of copper, and they were all layered materials. But if the high  $T_c$  field teaches us anything it is to keep an open mind and never rule anything out. The community learned that once in 1986 and learned it again in 2008 with the introduction of the pnictide superconductors when Kamihara [9] discovered a superconductor without copper and without a layered structure Our basic understanding of superconductivity is once again challenged.

But really our basic understanding was not that firm prior to the pnictides. Twenty-five years on the strictly copper superconductors had not yielded the answers to some basic questions. One very basic question concerns pairing. In the BCS case the gap in the density of states implied the creation of cooper pairs. But does the creation of a gap ALWAYS imply pairing? Or is it governed by a totally different mechanics? In the high temperature superconductor case this question has not been answered and is the subject of this thesis.

## 1.3 Cuprates-the Copper Family of High Temperature Superconductors

### 1.3.1 Crystal Structure of Cuprates

In most of the high  $T_c$  materials it is the copper and oxygen that facilitates the interesting physics. The oxygen 2p orbital hybridizes with Copper's 3d electrons which are doubly ionized to form a 2-d plane. Copper-oxygen high temperature superconductors are called cuprates. All cuprates are layered perovskites. They all have one or more of these copper oxide planes per unit cell. Single layer materials have one  $CuO_2$  plane per unit cell, multi layer materials have two or three  $CuO_2$  planes per unit cell. The  $CuO_2$  planes are interweaved by other blocks of elements which serve as charge reservoirs. Cuprates can be categorized into different families. Families differ from each other by having different elements in these blocks, such as *Bi* family, *La* family, *Tl* family, *Y* family, *Hg* family, etc.

A typical single layer Cuprates parent compound is  $La_2CuO_4$ . Its crystal structure is shown in Fig. 1.2. Each Copper is surrounded by six oxygens to form an octahedron. The Cu ions in the  $CuO_2$  plane form a square lattice with a  $Cu - Cu$  distance of 3.8 Å. The  $Cu - O$  distance along the  $c - axis$  is 2.4Å, slightly larger than the ones in the plane. This distance can be larger in other materials. The  $CuO_2$  plane is well separated by  $LaO$  plane.

Depending on the material, the copper oxygen plane can be linked with additional oxygen. The square oxygen lattice (among the copper sites) can have this so called apical oxygen either directly above or below the four oxygens. This is referred to as the  $CuO_6$  octahedron. In the single layer compounds the octahedron is unmodified with the apical oxygen above and below. In the double layer structures it is split in half to form two separated

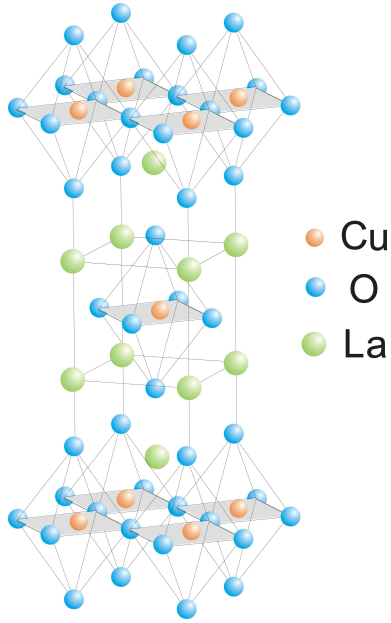


Figure 1.2: *The crystal structure of  $La_2CuO_4$*

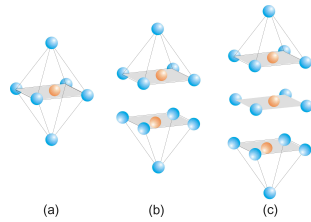


Figure 1.3: *The copper oxygen structure in the (a)single, (b)bilayer, (c)trilayer cuprate parent compounds*

pyramids. In the tri-layer structure the split in half pyramids have a single  $CuO_2$  plane sandwiched in between them. The basic copper oxygen structures in cuprates are summarized in Fig. 1.3. Experimentally it is observed that the  $T_c$  of a material is related to the number of layers. So this octahedron structure is examined in terms of its influence on superconducting behavior.

### 1.3.2 Electronic Structure of Cuprates

The unique nature of the cuprates originates from the basic electronic structure of this class of materials. Copper has the electron configuration of  $[Ar]3d^{10}4s^1$ . This is contrary to the ordinary filling order of  $4s$  before  $3d$ . The electron configuration creates a more stable half filled shell and leaves completely filled subshells. In this case copper behaves like an electron donor while oxygen behaves like a hole donor. When copper loses 2 electrons and becomes  $Cu^{2+}$ , the outer subshell has a  $3d^9$  configuration. According to crystal field theory, in the octahedral symmetry, the five degenerate  $d$ -orbitals split into two sets, where the  $d_{xy}, d_{xz}$  and  $d_{yz}$  orbitals will be lower in energy than the  $d_{z^2}$  and  $d_{x^2-y^2}$  orbitals. The former set is referred to as  $t_{2g}$  and the latter set is referred to as  $e_g$ . The  $e_g$  orbital degeneracy is lifted further due to the distortions away from a perfect octahedron (two apical oxygens are further away than usual). The field splitting is demonstrated in Fig. 1.4. In this case the  $d^9$  configuration gives us a half filled  $3d_{x^2-y^2}$  orbital, i.e., one electron (electron picture) or one hole (hole picture) per site. From band theory, half filling results in a metal. Strong interactions dominate the energy and the band is split into the upper Hubbard band and the lower Hubbard band. The lower Hubbard band is filled while the upper Hubbard band is empty. This forms a Mott insulator [10]. Cu  $3d_{x^2-y^2}$  and O  $2p$  orbitals form a covalent bond. In terms of the hole picture, the copper site is occupied by one hole with spin  $S = \frac{1}{2}$  while the oxygen site is empty. The nearby copper sites have opposite spins. This lowers the energy. This results in a ground state which is antiferromagnetic (AF) at half filling. A more detailed discussion will be included in later chapters.

Precisely at half filling the cuprates show antiferromagnetism, but the material does not always have to be at half filling. More electrons can be added or removed to change the filling factor. This is called doping. If extra electrons are removed this is called hole-doping and if extra electrons are added this is called electron doping. When the material is doped away from

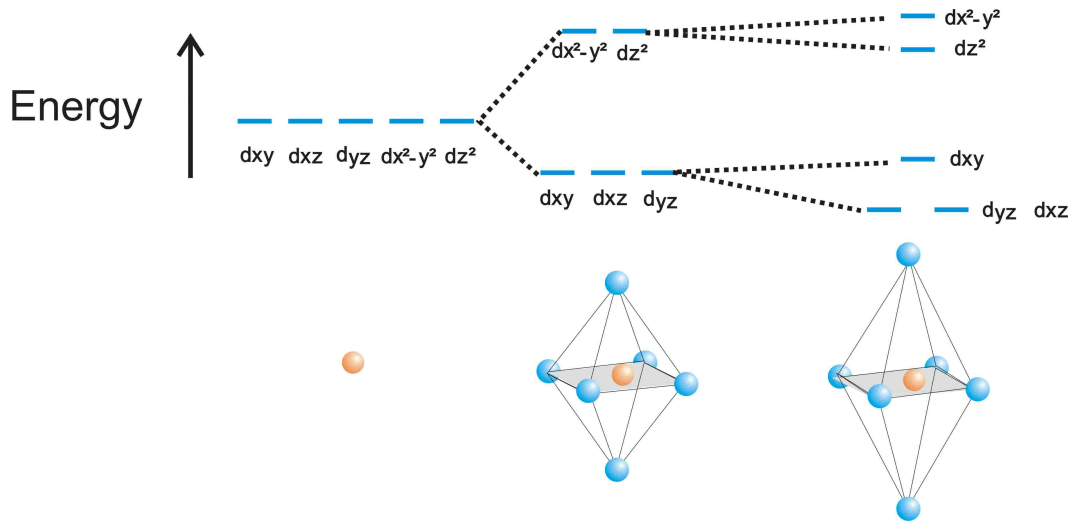


Figure 1.4: *Octahedron crystal field splitting for copper*

half filling, different states can emerge other than antiferromagnetism. If the parent compound contains cations of  $n+$  valence, substituting  $x$  percent of it with cations of  $(n - 1)+$  valence can result in a hole doped cuprate; And similarly, substituting  $x$  percent of it with cations of  $(n + 1)+$  valence can result in an electron doped cuprate.

I focus on the hole doped side of the cuprates. From half filling, with the increase of doping, AF order gets suppressed. With a greater increase in doping, superconductivity appears and gets stronger in terms of the  $T_c$  value. This increase lasts until the point called optimal doping where  $T_c$  is at a max, beyond which superconductivity begins to get weaker in terms of the  $T_c$  value and eventually disappears. As previously discussed there are other ways to destroy the superconductive states such as increasing temperature and increasing magnetic field. With an increase of temperature the superconductivity gets quenched in a parabolic shape following doping. Because of this shape it is referred to as the dome of superconductivity. The standard way to view this area, where the superconductivity can live. is to look at the

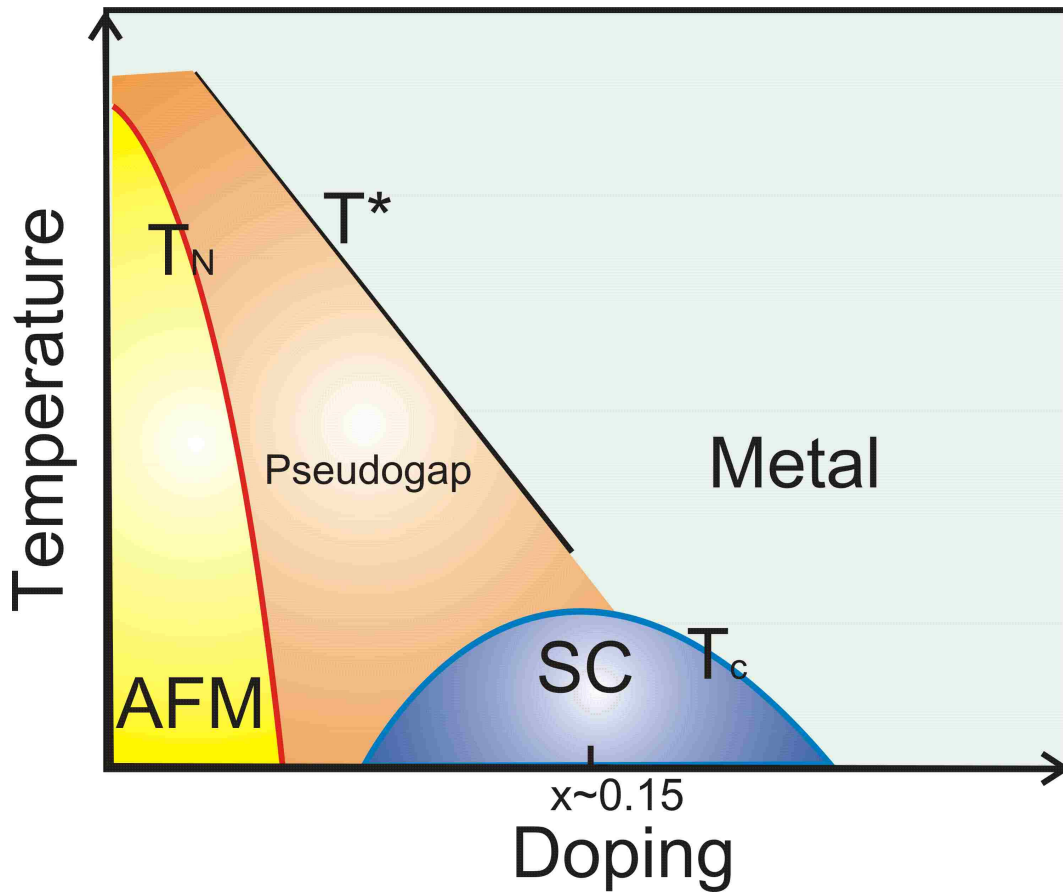


Figure 1.5: *The temperature vs. doping phase diagram of the cuprates.*

temperature vs. doping phase diagram. (see Fig. 1.5). This tracks out the area where the material is superconductive.

Besides resistivity other experimental probes can give clues about this superconductivity. Sometimes though the probes disagree and some confusions exist. One place of extreme confusion is the area spaced between the superconducting dome and AF order. This is called the pseudogap and the subject of this thesis.

## 1.4 A Mystery in Cuprates: The Pseudogap Phenomena

### 1.4.1 What is a Pseudogap

The pseudogap is a gap in the density of states as recorded by many experiments. It is known that in the regime where the pseudogap exists the material is not a superconductor. It could still be a pairing gap, though. It was seen in the low temperature BCS case that electrons paired leaving behind a superconductive gap of size  $2\Delta$ . In the BCS case this is unambiguously known to be a cause of pairing. Of course not all gaps are consequences of pairing. Insulators, semiconductors and the quantum Hall effect are examples of gaps not caused by the pairing of electrons. So is the pseudogap a consequence of pairing or something else? This is unclear and the source of great debate. It is the general feeling that it is probably one of two things though. The first idea is that the pseudogap is related to superconductivity and that it is, a pairing gap due to pairing of electrons into cooper pairs. For some reason though, these cooper pairs are not able to achieve coherence and thus do not become truly superconductive. The second idea is that the gap is something else entirely. Perhaps some other ordering that is not related to superconductivity and it competes with it. This debate is referred to as the pre-formed pairs vs. competing order debate. We will give more details on this debate in the last section of this chapter. In studying this problem the terms  $T_c$  and  $T^*$  are used. Below  $T_c$  the material is superconductive. Above  $T^*$  the material behaves like a “normal metal”. The pseudogap is a suppression of density of states in the regime  $T_c < T < T^*$  in the underdoped cuprates. In the following sections I will review the experimental evidence and interpretation of many different experiments performed in the pseudogap region.

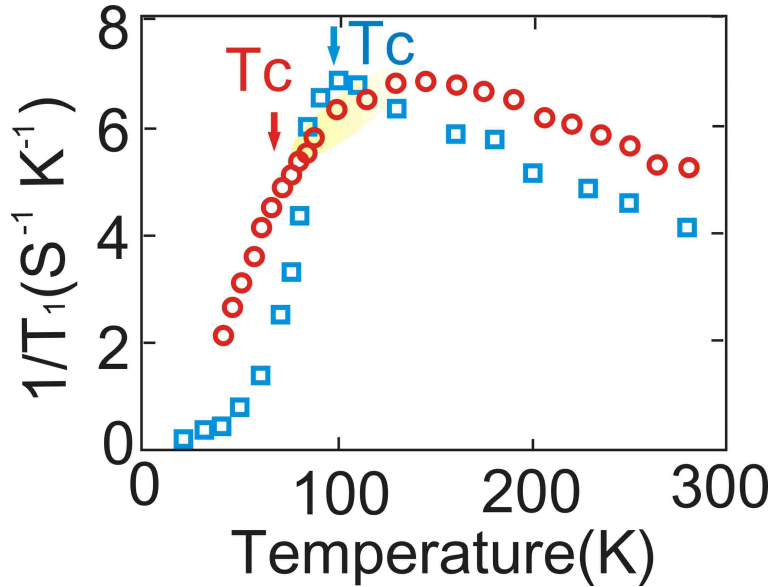


Figure 1.6: *Planar  $^{63}\text{Cu}$  spin-lattice relaxation rate in optimally doped  $\text{YBa}_2\text{Cu}_3\text{O}_{6.95}$  (squares) and underdoped  $\text{YBa}_2\text{Cu}_3\text{O}_{6.64}$  (circles). The pseudogap causes a suppression in the relaxation rate well above  $T_c$  in the underdoped material.*

#### 1.4.2 Pseudogap Experimental Evidence: First Experiments

In BCS superconductors, pair formation will affect the spin response. When the free spins bind together to make cooper pairs at  $T_c$ , the spin response decreases due to the lack of free spins. This decrease was expected in high temperature superconductors at the transition temperature  $T_c$  and it did indeed happen. The experiments measuring such phenomena are the Nuclear Magnetic Resonance (NMR) measurements. NMR is a local probe to explore the spin channel of electronic state at different nuclear sites in the lattice. It has an advantage in that it does not require large samples for measurements so it is usually one of the first techniques used on a newly discovered material.

In 1989, Warren et al. used NMR to study in  $\text{YBa}_2\text{Cu}_3\text{O}_{6+\delta}$  in the underdoped regime at  $\delta = 0.64$  with  $T_c = 60$  K, and compared the result with

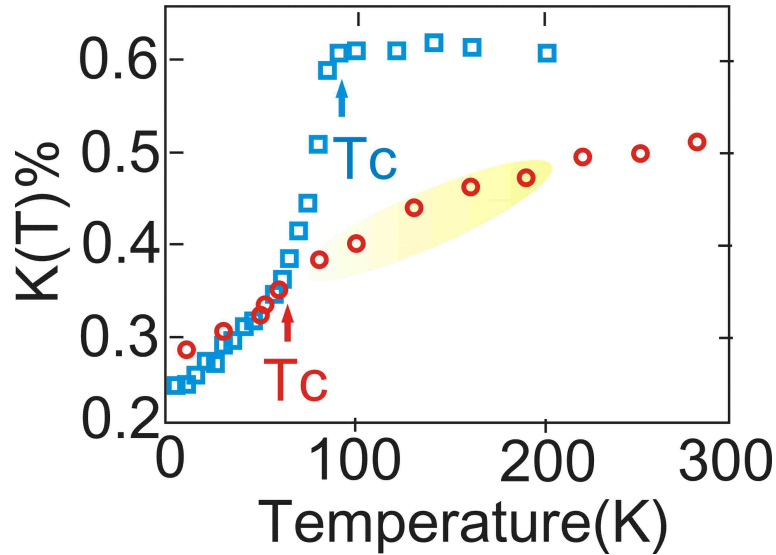


Figure 1.7: *Planar  $^{63}\text{Cu}$  Knight shift in optimal doped  $\text{YBa}_2\text{Cu}_3\text{O}_{6.95}$  (squares) and underdoped  $\text{YBa}_2\text{Cu}_3\text{O}_{6.64}$  (circles). The normal-state susceptibility is temperature independent in the optimally doped compound but decreases with temperature in the underdoped compound.*

the same measurement in the optimal doped regime at  $\delta = 0.95$ ,  $T_c = 92$  K. They found that the spin relaxation rate (the imaginary part of the low frequency dynamic spin susceptibility) began to be reduced at a temperature much higher than  $T_c$  in the underdoped sample, while it only starts to drop at  $T_c$  in the optimal doped sample on the contrary [11] (See Fig.1.6).

In 1990, Walstedt et al. measured the Knight shift also in underdoped and optimal doped YBCO [12]. (see Fig. 1.7). This technique finds a characteristic shift,  $K_s$ , which is proportional to spin susceptibility  $\chi_s$ . In the context of Fermi liquid it is proportional to the density of states at the Fermi surface. At high enough temperature,  $\chi_s$  is a constant as in a normal metal. Upon decreasing the temperature, very different temperature dependent behavior is observed in these two different compounds. In the optimal doped case, the polarization of electrons in the magnetic field starts to decrease dramatically because Cooper pairs start to form below the transition temperature,

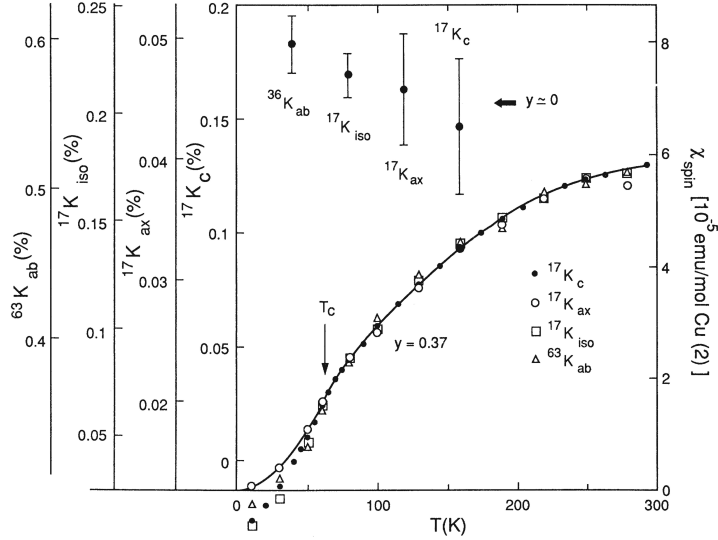


Figure 1.8: Various components of the Cu and O Knight shift are plotted against temperature with different vertical scales and origins. The  $T$ -dependent values of spin Knight shifts in the  $y \approx 0$  material are also plotted with the same vertical scales.

this is consistent with the classic superconductors. But in the underdoped case, way above the transition temperature  $T_c = 60$  K, a suppression of spin susceptibility has already occurred. Such suppression persists upon further decreasing temperature. These results were similar to results taken earlier by Aloul et al.[13]. It was found that all the nuclei (not just copper) show the same evidence of the pseudogap. It was also found that different sites have identical  $T$  dependence. [13] [14]. This will provide justification for using a one band only model. (See Fig. 1.8). It should also be noted that the data is similar in all cuprates such as in the BSCCO family. [15]

A similar suppression at high temperatures was seen in the magnetic susceptibility measurements of Johnston et al. [16] Rather than spin singlet formation Johnston interpreted this as following the same behavior of 2D Heisenberg antiferromagnet. The model predicts that the static magnetic

susceptibility will decrease, which is what is seen.

### 1.4.3 Pseudogap Experimental Evidence: ARPES

Angle-resolved photoemission spectroscopy (ARPES) measures the density of single electron excitations below the Fermi energy and has been very important in the study of cuprates. ARPES is a powerful tool for many reasons but probably its most notable asset is in its ability to take angle resolved measurements and thus be able to map the Fermi surface and the constant energy contours. In ARPES, the sample being studied contains electrons that are held inside of the material by the work function  $\phi$ . An incoming photon can be absorbed by the material and can free the electron, if it has enough energy to break the vacuum barrier. This electron will travel toward the detector in a manner which can be modeled as a plane wave. The direction of the electron is recorded as well as the kinetic energy, yielding the full electron momentum. The relevant information though is not the measurement of the electron, the interest is in relating this to the material which has been excited. This is usually analyzed in terms of the three step model: Step 1 is the optical excitation of the electron as it is living inside the solid. Step 2 is the transport of this photoelectron to the surface of the material. Step 3 is the escape of the photoelectron into the vacuum space. This is a simplification and breakdown of the actual process where all three steps in essence happen simultaneously. In this model, though, they are well separated and independent and all treated classically except for step 1.

By using Fermi's golden rule the photocurrent is expressed as

$$\omega_{if} = \frac{2\pi}{\hbar} |\langle \Psi_f^N | H_{rad} | \Psi_i^N \rangle|^2 \delta(E_f^N - E_i^N - h\nu) \quad (1.1)$$

and with the electron interacting with the radiation field given by the Hamil-

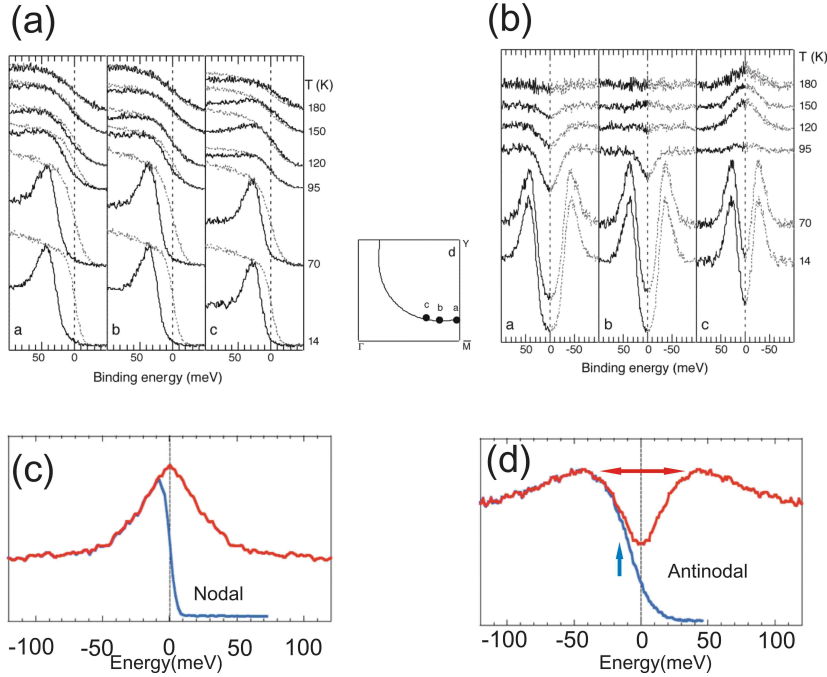


Figure 1.9: (a) Spectra showing various pseudogap closing temperatures for various positions around the M point. (b) Symmetrized spectra showing various pseudogap closing temperatures for various positions around the M point. (c) Extracted spectrum from (a)(b) on the point near the nodal region. (d) Extracted spectrum from (a)(b) on the point near the antinodal region. The vertical arrow shows one way to determine gap size: the leading edge gap. The horizontal arrow shows the other way to determine gap size: the symmetrized gap.

tonian where the dipole approximation is used

$$H_{rad} = -\frac{e}{2mc}(A \cdot p + p \cdot A) \approx -\frac{e}{mc}A \cdot p \quad (1.2)$$

From this the single particle spectral function can be related to the measured photocurrent. It is not necessary to go through the full mathematical rigor of this derivation at this time.

As the high  $T_c$  cuprate was engineered and sample quality improved the quality of ARPES techniques and equipment were constantly improving as well, leading the way for better experiments with higher quality data. This

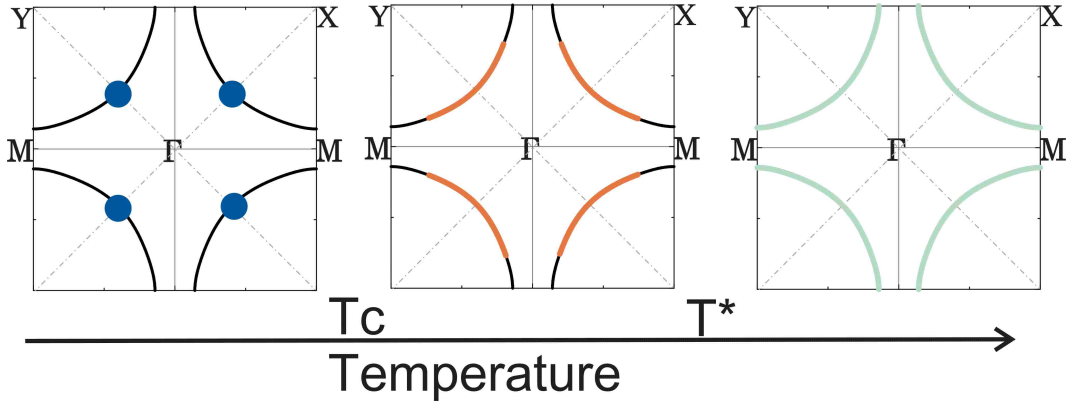


Figure 1.10: A schematic diagram of the so-called Fermi arc created by the momentum dependent closings. The d-wave node below  $T_c$  (left panel) becomes a gapless arc above  $T_c$  (middle panel) which expands with increasing  $T$  to form the full Fermi surface at  $T^*$  (right panel).<sup>[20]</sup>

made it possible to take higher resolution data both in angle and in energy on high temperature superconductors. An early pioneer in the ARPES of BSCCO 2212 cuprates was Ding et al. [17]. They directly measured the momentum resolved electron excitation spectrum in the copper-oxygen planes on a variety of dopings of BSCCO from overdoped to heavily underdoped. A suppression of spectral weight was found to be present above  $T_c$ . In the sample with  $T_c = 83$  K this suppression was found to exist all the way to 170 K. They labeled this temperature as  $T^*$ . For a more underdoped sample, where the  $T_c$  was reduced to as low as 10 K, the suppression lasted all the way to temperature of 300 K. This was seen at the M point or the  $(\pi,0)$  point in the Brillouin zone. At the  $(0,0)$  to  $(\pi,\pi)$  direction no gap is ever seen. At these high temperatures, it was observed that the linewidths are so broad that the spectral weight at the Fermi energy is non-zero, so it is not the hard gap but rather a pseudogap. This pseudogap was found to have d-wave symmetry and appeared to transition into the superconducting gap as the temperature was lowered below  $T_c$ . Similar results were seen from other ARPES studies [18][19].

Above  $T_c$ , in the normal state, the optimally doped high temperature superconductor should appear metallic (in that it has a Fermi surface of gapless electronic excitations). The ARPES measurements confirmed this. Norman et al. though set out to determine this Fermi surface for the underdoped samples [20]. They had studied this problem at three points in momentum space. When the sample is cooled the initial temperature at which the pseudogap opens is found to be strongly momentum dependent (See Fig. 1.9 a. and b.). Since ARPES measures  $I(k, \omega) \propto A(k, \omega)f(\omega)$ , there are two ways to read the gap size from the Energy Distribution Curve (EDC): one is the leading edge gap; The other is the gap after symmetrization (see Fig. 1.9 d.). The purpose of symmetrization is to remove the effect of the Fermi function:

$$\begin{aligned}
 A(k_f, \omega) &= A(k_f, -\omega) \\
 I_{sym}(k_f, \omega) &= I(k_f, \omega) + I(k_f, -\omega) = I_0 A_{sym}(k_f, \omega)
 \end{aligned}
 \tag{1.3}$$

Comparing the symmetrized spectrum at the nodal and antinodal region, as extracted in Fig. 1.9(c)(d) from (a)(b), the gap shape is highly anisotropic in k-space. When the temperature is between  $T^*$  and  $T_c$ , the spectrum is gapless around the nodal region while it has substantial sized gaps around the antinodal region. This “nodal-antinodal dichotomy” is more clearly expressed in the mapping of the Fermi surface in this temperature region (see Fig. 1.10(b)). The different momentum dependence of the gap leaves the Fermi surface to have a discontinuous contour, the so called Fermi arc. Some regions of the Fermi surface become gapped while other parts remain gapless. As a result of this unusual anisotropy in momentum space, the concept of the “*hot*” electron and “*cold*” electron came out. The “*hot*” electrons are near the antinodal region and “*cold*” electrons are near the nodal regions. The “*hot*” electrons are considered to be more prone to the pseudogap phenomena.

Though the gap is transitioning at different points in momentum space

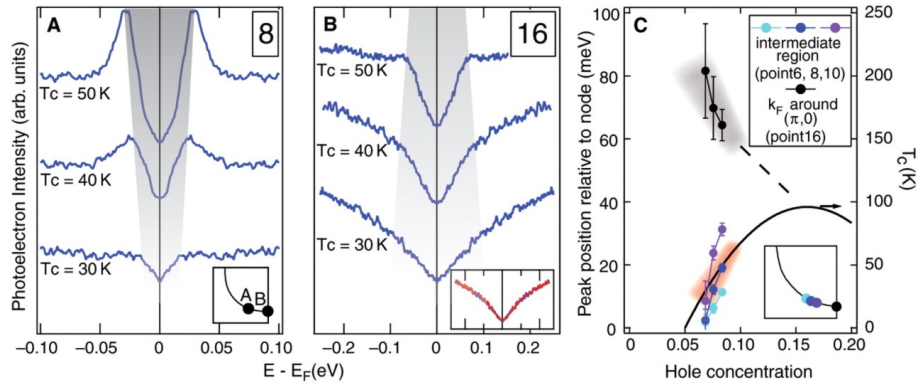


Figure 1.11: The graph on the left shows the doping evolution closer to the node and the graph in the center shows the doping evolution at the antinode. The shading denotes the determination of gap size and the opposite trend in doping is seen in the two graphs. This data is plotted to the right on a phase diagram. Figure from [21]

it was originally assumed that this was the same gap. This might not be the case though. Tanaka et al. have a different proposal. They used ARPES on deeply underdoped  $Bi_2Sr_2Ca_{1-x}Y_xCu_2O_8$  (Bi2212). They found a gap where no coherence peak was observed. This was found in the antinodal regime and increased in size with underdoping. This was consistent with all previous results. Another gap was found though in the area near the nodal regime. This gap has a coherence peak and the gap reduced with underdoping. This was a surprise and not previously observed. This leads Tanaka et al. to conclude that two distinct energy gaps are inherent in this material [21]. (See Fig. 1.11). Ma et al. found a similar result through dividing the low temperature spectrum from the high temperature spectrum. They indeed find two distinct gaps. They propose that the gap that is near nodal is potentially the gap associated with superconductivity and that it doesn't stop at the antinodal region but actually extends into it. [22]

The pseudogap phenomena ARPES observed can be summarized here: When  $T > T^*$ , the Fermi surface is a large continuous contour and the system is a normal metal. Right below the characteristic temperature  $T^*$ , a

Fermi surface mapping shows discontinuous arcs formed from the points that have no pseudogap along the arcs contrasted with the points that still have pseudogaps near the antinodes. As the temperature is further decreased these Fermi arcs shrink. Below  $T_c$ , the material is a full d-wave superconductor so the Fermi surface is fully gapped except at the nodes which are protected by the d-wave symmetry of the superconducting gap. This break up of the Fermi surface occurs without long range order, which is a very surprising result. The temperature dependence of the Fermi surface is shown schematically in Fig. 1.10. The gap near the nodal region and the gap near the antinodal region behave distinctively in terms of their momentum, temperature and doping dependence. This is supportive of the two-gap scenario.

### 1.4.4 Pseudogap Experimental Evidence: STM

One of the easiest ways to visualize the pseudogap is by looking at scanning tunneling microscope (STM) spectra on BSCCO 2212. The STM is able to measure the single particle density of states with extreme spatial resolution. The operating principle of the STM is based on quantum tunneling. When a sharp tip is brought in range of a surface, classical mechanics forbids an electron from jumping from the tip to the surface unless the energy of the electron exceeds the energy of the work function describing the system. Quantum mechanics, however, permits an electron with energy lower than the barrier to travel from the sample to the tip (or visa versa). Since in the quantum world an electron is not a point particle but rather a wave like spatial entity it is possible that there is some overlap between the wavefunction of the tip and the sample. An overlap in the wavefunction means that an electron of arbitrary small energy can end up on either side of the barrier separating these wave functions with some probability proportional to the size of the overlap. Even at atomically close distances this overlap will be extremely small which means these events are very unlikely. However unlikely, they do happen and can be counted by an electrometer which is part of the STM circuit. This counting of tunneling electrons is how the STM takes data. The physical framework of how this works is given for a given geometry based on Bardeen's tunneling theory [23].

$$I_{tip \rightarrow sample} = 2 \times \frac{2\pi e}{\hbar} \int_{-\infty}^{\infty} |M_{ts}|^2 \underbrace{\rho_t(\epsilon + eV) \cdot f(\epsilon + eV)}_{\# \text{ of filled tip states}} \underbrace{\rho_s(\epsilon) \cdot [1 - f(\epsilon)]}_{\# \text{ of empty sample states}} d\epsilon \quad (1.4)$$

The current flowing from the tip to the sample is based on the applied bias voltage  $V$  where  $M$  is some tunneling matrix based on the sample-tip characteristics,  $f(E)$  is the Fermi-Dirac distribution and  $\rho_{t(s)}$  is the density of states of the tip or sample. After subtracting the corresponding contri-

bution from sample to tip and making low temperature approximations and approximations based on the tunneling matrix it can be shown for certain metallic tips (with flat density of states profiles) the current across the tunneling junction is:

$$I(\mathbf{r}) \propto e^{-2\xi z} \int_0^{eV} \rho_s(\mathbf{r}, \epsilon) d\epsilon \quad (1.5)$$

A simple numerical derivative with respect to voltage then gives that  $dI/dV$  is proportional to the density of states of the sample. (In practice the derivative is performed by a machine called a lock-in amplifier to keep signal noise low). So what can the STM and its density of states measurements say about superconductivity and the pseudogap? It is known from measurements on BCS superconductors that the STM will show the superconducting gap at temperatures below  $T_c$  with no states residing at the Fermi energy and a metallic state with many states at the Fermi energy above  $T_c$ . The superconducting gap had also been seen at temperatures below  $T_c$  on high temperature cuprates like BSCCO 2212. In 1998 Renner et al. decided to use STM to study the superconducting gap in BSCCO as a function of temperature.

Renner et al [24] are among the first who reported the direct observation of pseudogap above the superconducting transition temperature in *Bi2212*, as shown in Fig. 1.12. When  $T < T_c$ , there is a d-wave superconducting gap around zero bias with sharp coherence peaks. When  $T_c < T < T^*$ , there is still a depression of conductance in the low energy regime, and this depression persists all the way to room temperature with a smooth evolution.

STM's most useful feature is in its spatial resolution and its ability to look for patterns. In the pseudogap phase, at temperatures around 100K, Vershinin et al. began to search for any spatial pattern associated with the pseudogap in BSCCO 2212 with zinc substitutions. These modulations were seen to be energy independent, following the orientation of the copper-oxygen

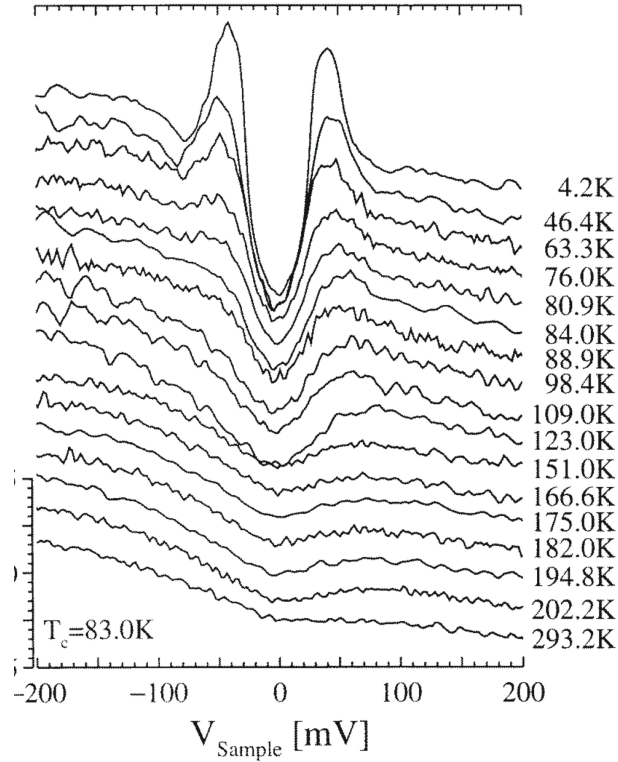


Figure 1.12: *Tunneling conductance of underdoped Bi2212, a gap like feature at zero bias is seen to persist in the normal state which is direct evidence of a pseudogap in the tunneling conductance . In the superconducting state a peak develops at  $\pm 45$  meV followed by a dip and a broad maximum, the gap size does not seem to have temperature dependence.[24]*

bonds, and have periodicity which is incommensurate with the lattice. They suggest that this has to do with some form of spin or charge ordering, which is only seen in this region above  $T_c$  and below  $T^*$ . [25]

Boyer et al. used temperature-dependent scanning tunneling spectroscopy to study the single layer cuprate  $(Bi_{1-y}Pb_y)_2Sr_2CuO_{6+x}$ . They found a narrow gap that vanishes near  $T_c$ . In addition to this, they found the typically observed inhomogeneous and broader gap, which is only weakly temperature dependent. They interpret these results that the smaller gap may be associated with superconductivity as it is associated with  $T_c$  and the larger gap

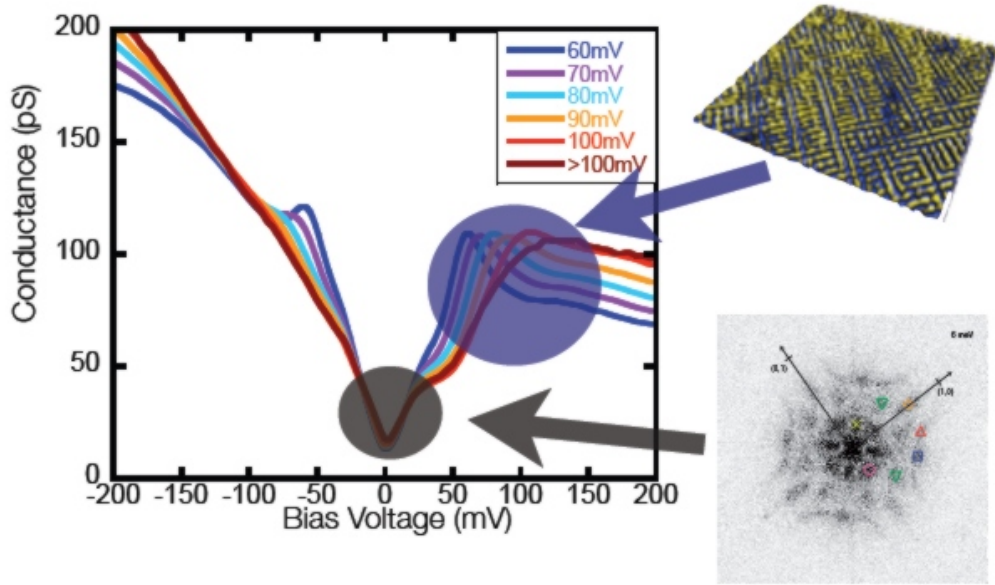


Figure 1.13: Spectra taken in underdoped BSCCO 2212 showing two distinct energy level features. The small feature shows quasiparticle scattering while the larger gap has some static charge ordering. Figure is based on data from Gomes et al. [27] and Kohsaka et al. [28] [29]

may be related to the pseudogap state.[26] This would be in contrast to the Kugler report though it is worth noting that these two gaps come from a division of high temperature by low temperature data and aren't necessarily observable in the low temperature data alone. These multiple energy features are visible though in the heavily underdoped BSCCO 2212 in the study by Gomes et al. [27](See Fig. 1.13)

#### 1.4.5 Pseudogap Experimental Evidence: Specific Heat

Loram et al [30][31] use a sensitive differential technique to measure the electronic specific heat in *YBCO*. They also find a pseudogap in the underdoped regime. The technique uses a reference sample with well known specific heat to compare with the exact same number of moles of the cuprate. When ex-

act same amount of heat is used to heat up both samples the difference of the temperature rise between these two samples are measured to calculate the specific heat of the cuprate sample. In the overdoped material a gap, signalled by a depression in the specific heat coefficient  $\gamma$ , opens up below  $T_c$ . In the underdoped sample a gap starts to form in the normal state below 140K way above  $T_c$ . This is the signature of the pseudogap.

### 1.4.6 Pseudogap Experimental Evidence: Raman Scattering

Raman scattering is one of the most common excitation spectroscopies for looking at phonons as well as other modes. The way that Raman scattering works is based on the inelastic scattering of a monochromatic source (usually in the range of 200-4000  $cm^{-1}$ ) although most of the source is scattered elastically. The part that is inelastic has a shifted frequency based on the excitation it was scattered from. This frequency shift can be based on either the absorption or emission of a photon in the scattering process which is referred to as the Stokes and anti-Stokes scattering processes respectively. A series of selection rules are used to determine which vibrations are being looked at. This makes Raman Scattering a powerful tool to look at quasiparticles in the superconducting state at specific momentums, specifically the nodal and anti nodal regions.

Slakey et al. used Raman scattering to complete one of the first studies on a high  $T_c$  cuprate YBCO. Previous studies had found BCS like behavior with a redistributed gap around 350 and 500  $cm^{-1}$  when probing the  $A_{1g}$  and  $B_{1g}$  symmetries. In the underdoped YBCO they studied though, they did not see that. They saw a peak that was insensitive to doping and persisted into the normal state past  $T_c$ . The peak got broadened but does not show softening. They claim that if the 500  $cm^{-1}$  peak is interpreted as a pairing energy then their results are consistent with pairing above 100K with no significant temperature dependence below this. [32].

Le Tacon et al. use electron Raman scattering (ERS) on as grown  $HgBa_2CuO_{4+\delta}$  ( $Hg + 1201$ ) with doping from underdoped to overdoped. This sample has specific properties that avoid nodal and antinodal mixing which sometimes occurs in other samples like YBCO. They characterize the superconducting state by examining the slope and position of the gap at the nodes and the maximum amplitude and position of the gap at the antinodes. Both of these parameters have different doping dependence which is not ex-

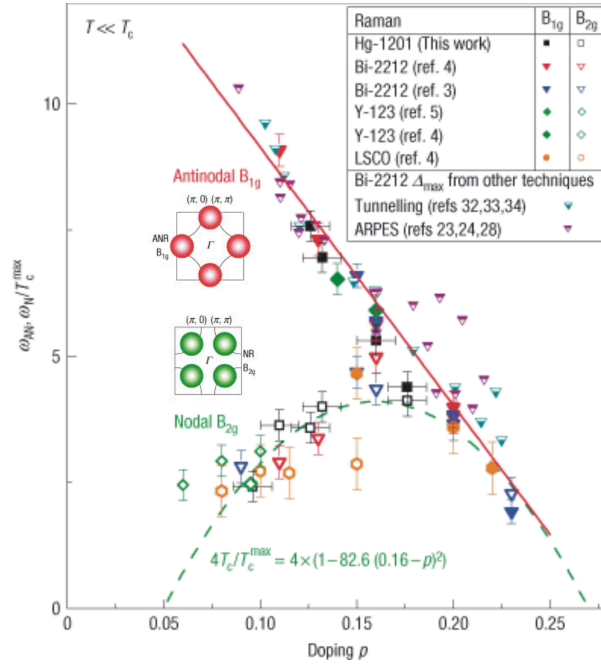


Figure 1.14: *Tacon et al.* use two new parameters on the Raman data to reclassify theirs and old data to show a new nodal/antinodal dichotomy for various cuprates. Figure from *Tacon et al.* [33]

pected for a standard d-wave gap. The nodal slope of the gap decreases as the doping decreases and the maximum of the gap increases as the doping decreases. The energy of the antinodal peak increases while the intensity of this peak rapidly decreases as the doping decreases. Together these facts point to the coherence of nodal quasiparticles and the incoherence of the antinodal ones. There are two distinct energy scales in the superconducting state which have different doping dependence in the underdoped regime. This has already been established in the normal state and now is seen in the superconducting state and coined the “nodal-antinodal dichotomy” . [33] (See figure 1.14)

## 1.5 The Origin of the Pseudogap State

The pseudogap has an intimate relationship with both superconductivity and antiferromagnetism at half filling. Understanding the role of the pseudogap is no easy task. To start with, I look at how superconductivity arises when the system is doped away from half filling. In the undoped compounds, at half filling, spin- $\frac{1}{2}$  moments on Cu order antiferromagnetically as an insulator. As holes are introduced into the insulator by doping, the hole on the copper site and the doped hole on the nearby oxygen site form a two-hole singlet state. This singlet moves coherently in the background of the copper spins [34] when there are enough doped holes to sustain the mobility. The hybridization of copper and oxygen holes lower the system's energy through the singlets' coherent motion. At different doping levels, there are different amounts of holes in the system. It is natural to relate the stability of the Zhang-Rice singlets' coherent motion to doping level. When the doping is approximately at half filling, the coherent motion is highly suppressed due to the lack of holes; the AF correlation between copper spins are particularly strong at very low doping. In an naïve picture, one would expect that the more holes doped, the more stable the coherence would be and that a large Fermi surface would exist whose area follows the Luttinger theorem. In this picture, in the normal state, I would have a large Fermi surface with a volume containing  $1 - x$  electrons and it would follow the signatures of conventional Fermi liquid. One specific example of this is in the cuprate material  $Tl_2Ba_2CuO_{6+\delta}$  ( $Tl - 2201$ ). It is extensively studied since it has a simple single  $CuO_2$  layer without other complications. In the overdoped regime, ARPES [35] and quantum oscillation experiments [36] have reached a consensus that indeed there is a large Fermi surface and the material acts as a regular Fermi liquid. But, as I will show you, in general, it is not always this simple.

Things are more complex when it comes to the underdoped regime. The situation is quite unconventional and the picture I spoke of earlier no longer holds. The experiments previously discussed [37] [38] show the signature of

a pseudogap in the normal state above the superconductor transition temperature  $T_c$ . Not until the temperature is increased all the way above  $T^*$  does it return to the conventional Fermi liquid state like what is seen in the overdoped case.

The origin of this pseudogap is one of the most intensely studied subjects in high temperature superconductivity [39]. After 30 years of debate, there is still no consensus as to what the pseudogap is; the basic dilemma is the ungapped portion of the Fermi surface. It should consist of continuous contours since the Fermi surface is the trajectories of the poles in the one-particle Green's function. One would expect that as temperature is decreased from below  $T^*$  to low temperatures (in the normal state when superconductivity is suppressed) the Fermi arc will evolve into either a Fermi point (Nodal liquid) or a Fermi surface pocket around the node. In reality however, despite numerous improvements in experimental methods and accuracy, there is no sign of pockets but instead a Fermi arc. The appearance of this Fermi arc is a haunting problem in high  $T_c$  field. There are many theories which can be mainly classified into two groups: proposals based on a one-gap scenario and proposals based on a two-gap scenario.

### 1.5.1 One-Gap Scenario

The one-gap scenario is a preformed pair scenario which considers the pseudogap to be an incoherent pairing gap above  $T_c$ . When temperature decreases from above  $T^*$  to below  $T^*$ , the d-wave pairs start to form but have not yet gained their long-range phase coherence yet. Upon further decrease of temperature toward  $T_c$ , the Fermi arc length shrinks toward the nodal point. The pseudogap evolves continuously to the d-wave superconductive gap, which resembles the coherent movement of the cooper pairs below  $T_c$  accompanied by the collapse of the arc to a node. The main point of the one-gap scenario is that there is only one gap existing below  $T_c$  and that d-wave pairing is the only driving force to gap the entire Fermi surface.

Models describing phase disordering include two different pictures. The first picture is thermal phase fluctuation [40][41][42][43]. The second picture is inelastic scattering and life-time effects [44]. The observed Nernst effect [45][46][47][48] provides evidence of large fluctuating superconductivity above the transition temperature. It is worth noting that there are two different kinds of pseudogaps. One has the same energy scale of the superconducting gap and extends above  $T_c$  to  $T_{MF}$ , which is the Nernst region. In this type of pseudogap the doping dependence of  $T_{MF}$  and  $T_c$  follow the same trend. The second kind of pseudogap is the more conventional pseudogap is shown in the phase diagram Fig. 1.5. This pseudogap has a clear characteristic temperature  $T^*$  which has the opposite doping dependence in the underdoped region with superconductivity.

Taking into account the experimental fact that the characteristic temperature  $T^*$  for pseudogap is increasing with respect to the doping decrease in the very underdoped regime, it is necessary to invoke an energetically competitive state with d-wave gap symmetry. [49]. Several quantum and thermal phase disordering in the fluctuating states are proposed, and they all involve a competing state with the superconductivity, such as the AF state [50], staggered flux phase [51], and stripes phase [52]. Among all these proposals there is only one gap - the d-wave pairing gap is responsible for the entire Fermi surface gapping.

Kanigel et al. reported that arc length depends only on the ratio  $T/T^*$ . The arcs collapse linearly with  $T/T^*$  ratio and extrapolate to zero [53][54]. They support the proposal that the  $T = 0$  pseudogap state is a nodal liquid – a strange metallic state whose gapless excitations exist only at points in k-space, just as in a d-wave superconducting state. However the experiments are performed on the optimal to lightly underdoped *BSCCO* samples, so there is a need for more information in the very underdoped regime to shed light on the pseudogap debate.

## 1.5.2 Two-Gap Scenario

In the two-gap scenario, the pseudogap is a completely different state from the superconducting state. It is an independent order of an energetically competitive state with a characteristic temperature  $T^*$  which is not related to electron pairing. The following proposals all follow this two-gap school of thought, including (1) static orbital current order.[55] [56] [57] [58] [59].(2) charge density wave order [60] [61] [62] [63].(3) valence-bond density density wave order[64].(4) other general density wave [65] [52].

Most of the theories involve breaking the translation symmetry, resulting in superstructures characterized by a finite crystal momentum  $q$ . A finite  $q$  vector gaps out the antinodal region of the Fermi surface and the folding of the bands by  $q$  gives Fermi pockets around the node. Because of the coherence factors which mix the quasiparticle states connected by vector  $q$ , one side of the pockets is weaker than the other side. This can give what appears as a 'Fermi arc'. There are also phenomenological theories which propose that the crossing of the Fermi surface and Luttinger surface leads to the truncation of the Fermi surface [66] [67] [68] [69].

After many years of research on this pseudogap issue, with much improved measurement resolution, Fermi pockets and folded bands have not been seen by ARPES. However, recent quantum oscillation measurement have suggested that there might be Fermi pockets in the presence of high magnetic field in underdoped *ortho-II*  $YBa_2Cu_3O_{6.5}$ . Since, though, the experiments were done in a very high magnetic field with suppressed  $T_c$ , the small Fermi pockets may be caused by a field induced density wave [70] [71].

## 1.5.3 My Concentration

The most important prediction of the two-gap scenario is that there are two gaps coexisting below  $T_c$ : a superconducting gap around the nodal region and a different gap around antinodal region [72]. The most recent ARPES

experiments[21] [73] [74] and Raman scattering experiments[75] support this two gap picture in the very underdoped regime. In *Bi2212* the superconducting gap is large and hard to be separated from the pseudogap. It is very hard to reach a very underdoped regime with a high sample quality. In order to overcome this difficulty, the above ARPES experiments have been performed on *Y* doped *Bi2212* or *Ln* doped *Bi2201*. They find that the spectral gap in the superconducting state contains two distinctly different pieces in terms of their momentum, temperature and doping dependence. One piece is a superconducting gap near the nodal region accompanied by a coherence peak that tracks  $T_c$ . The other piece is a large pseudogap near the antinodal region that is associated with a broad spectrum without a coherent peak that tracks  $T^*$ . This evidence strongly support the idea that pseudogap emerges from the generic two-gap scenario. In this thesis, I will start with a non-superconducting normal state and describe the origin of the Fermi arc in the clean case. Then I will study the pinning of such pseudogap state by the disordered ionic potential and the interplay of the two gaps. Several perspectives will be presented to be compared with the experiments.

# Chapter 2

## Renormalized Mean Field Theory for High $T_c$ Cuprates

In a strongly correlated system the inter particle interactions are very important. They dominate over the single particle dynamics. High temperature superconductors fall into the category of strongly correlated systems and the dominating interactions manifest different novel states. The t-J model is commonly considered to be the bare minimum model for high temperature cuprates. It is simple yet sophisticated and complicated enough to capture the salient characteristics of the complex materials. The t-J model can not be solved exactly. Approximations are needed to make theoretical progress. Starting from the basic interactions in cuprates, I will derive the renormalized t-J model which will be integral to the rest of this thesis.

### 2.1 Emergence of the t-J Model

All the members of the cuprate families share similar quasi 2D structures which contain layers of  $CuO_2$  planes. These planes are known to be the "battle fields" of the electrons and focal planes of the physics. Despite the vast difference in both number of layers of  $CuO_2$  planes and chemical com-

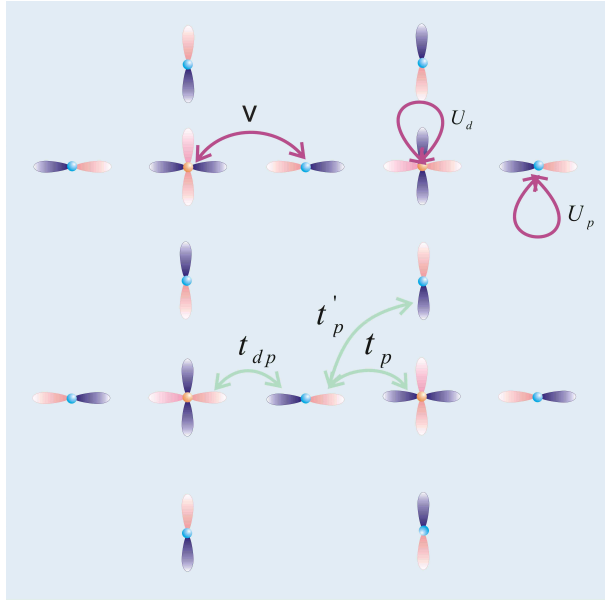


Figure 2.1: *Hopping integral, onsite potential and intersite potential with the quasi 2D  $\text{CuO}_2$  layer, revised from [79]*

position of the insulating layers, different families of cuprates all share the similar basic properties of high temperature superconductors. Therefore, such a system, can be simplified into one 2D plane with a square lattice of Copper atoms with an Oxygen atom sitting between each Cu-Cu bond.

### 2.1.1 Three-Band p-d Model

From the electronic structure of the  $\text{CuO}_2$  plane it is known that the most straight forward model is to directly deal with the Cu  $3d_{x^2-y^2}$  orbital and the O  $2p$  orbital. Several physicists have developed this three-band model [76] [77] [78] which takes into account the interactions between the nearest neighbor  $\text{Cu} - \text{O}$  bonds, the nearest neighbor  $\text{O} - \text{O}$  bonds and the next nearest neighbor  $\text{O} - \text{O}$  bonds (see Fig. 2.1). The Hamiltonian can be written, in the context of a "hole language" as Eq. 2.1 [79].

$$\begin{aligned}
H_{dp} = & - t_{dp} \sum_{\langle i,j \rangle \sigma} (d_{i\sigma}^\dagger p_{j\sigma} + h.c.) \\
& - t_p \sum_{\langle j,j' \rangle \sigma} (p_{j\sigma}^\dagger p_{j'\sigma} + h.c.) \\
& + t'_p \sum_{\langle j,j'' \rangle \sigma} (p_{j\sigma}^\dagger p_{j''\sigma} + h.c.) \\
& + \epsilon_d \sum_{i,\sigma} n_{d,i\sigma} + \epsilon_p \sum_{j\sigma} n_{p,j\sigma} + U_d \sum_i n_{d,i\uparrow} n_{d,i\downarrow} \\
& + U_p \sum_j n_{p,j\uparrow} n_{p,j\downarrow} + V \sum_{\langle i,j \rangle} n_{d,i} n_{p,j}
\end{aligned} \tag{2.1}$$

Where  $d_{i\sigma}^\dagger$  ( $d_{i\sigma}$ ) is a creation(annihilation) operator of a hole with spin  $\sigma$  on the  $Cu_{3d_{x^2-y^2}}$ -orbital at site  $i$ , and where  $p_{i\sigma}^\dagger$  ( $p_{i\sigma}$ ) is a creation(annihilation) operator of a hole with spin  $\sigma$  on the  $O_{2p}$ -orbital at site  $j$ .  $\langle i, j \rangle$  means  $i$  and  $j$  are the nearest neighbors. The number operators are defined as  $n_d = \sum_{\sigma} d_{i\sigma}^\dagger d_{i\sigma}$  and  $n_p = \sum_{\sigma} p_{i\sigma}^\dagger p_{i\sigma}$ . The vacuum is defined as  $Cu 3d^{10}$  and  $O 2p^6$ . Due to the  $Cu d^9$  electron structure the outer most orbital is the  $Cu 3d_{x^2-y^2}$  orbital and it lays head to head with the oxygen  $2p$  orbital (see Fig. 2.2). The hopping integrals  $t_{dp}, t_p, t'_p$  correspond to the hybridizations of the atoms whose bonds are connected together. They are proportional to the overlap of the wave functions of the corresponding holes. They give the energy gain by destroying one hole from one site and simultaneously creating another hole on the neighboring site. The most significant hopping integral is the d to p orbital hopping  $t_{pd} \sim 1.3eV$ . It is about twice the magnitude of the nearest p to p orbital hopping  $t_p \sim 0.65eV$ . The energy level of the single occupied copper d orbital is  $\epsilon_d$  and the energy level of the oxygen p orbital is  $\epsilon_p$ , (here I set  $\epsilon_d = 0$ ). The difference in these two orbitals is defined as  $\Delta_p = \epsilon_p - \epsilon_d$  at half filling. In the charge transfer insulator picture, because  $\Delta_p > 0$ , it is energetically favorable for one hole to sit on the copper

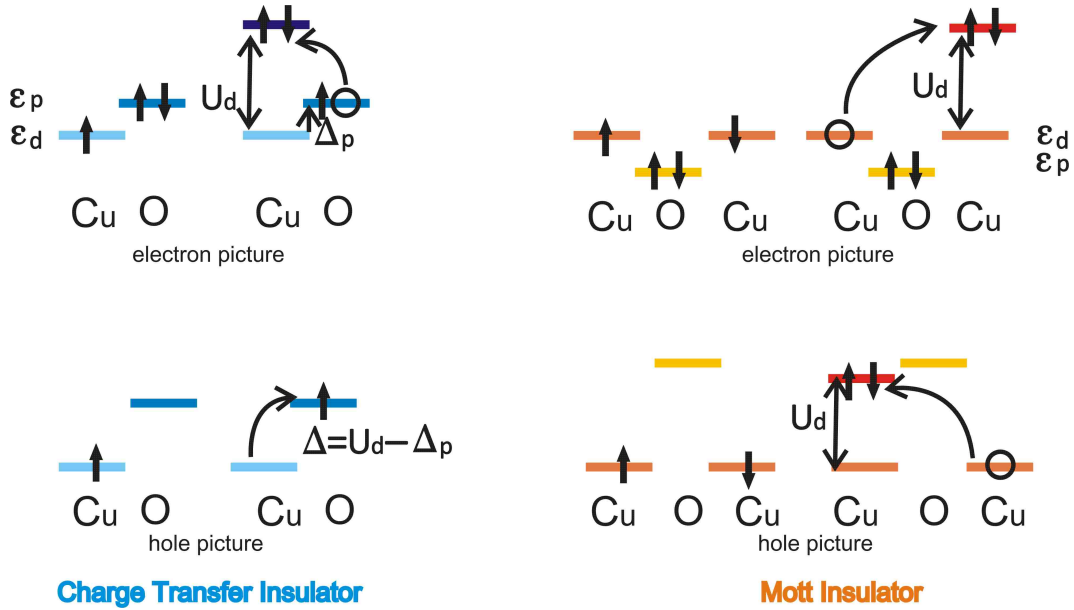


Figure 2.2: *Charge transfer insulator and Mott Insulator, revised from [79]*

d orbital. The definition of  $\Delta = U_d - \Delta_p$  is given by Fig. 2.2, which is the energy difference between the copper d orbital and the oxygen p orbital. The onsite potential of copper  $U_d = 10.5eV$  is huge. This means that the lowest energy excitation would be one hole with spin  $\frac{1}{2}$  coming from the copper site and going to the oxygen site. This makes the undoped parent compound a charge transfer insulator. Other repulsions in the system are the oxygen onsite repulsion  $U_P \sim 4eV$  and the nearest neighbor repulsion in between the copper and oxygen  $V = 1.5eV$ . They are both significantly smaller than  $U_d$ .

It is worth mentioning the difference between a charge transfer insulator and a Mott insulator. At half filling, in the electron picture, the lowest energy excitation is exciting an electron from the fully occupied O 2p to the Cu 3d orbital to form a fully occupied Cu 3d orbital. The energy cost is  $\Delta = U_d - \Delta_p$ , where  $U_d$  is the onsite coulomb repulsion of the d orbital

double occupancy and  $\Delta_p$  is the energy difference of Cu 3d and O 2p. If  $\Delta_p$  is sufficiently large as compared to  $t_{pd}$ , one hole will form a local moment on Cu. That is referred to as a charge transfer insulator [80]. It is more convenient to think in the hole picture, where the Cu 3d orbital is singly occupied by a hole with spin  $\frac{1}{2}$ . Upon exciting this hole to the empty O 2p orbital, the energy cost is  $\Delta \sim 3.6eV$ . On the other hand, the Mott insulator follows a different story, here, at half filling. In the electron picture, a fully occupied O 2p has lower energy than the singly occupied copper. The lowest energy excitation will excite one electron from one copper orbital to the other, forming a doubly occupied copper orbital with a huge energy loss of  $U_d$ . This is why the electrons are confined to their own copper sites to form local moments, referred to as the Mott insulator [10]. In this scenario, O 2p is always fully occupied by electrons, or say, fully empty without any holes. So O 2p is left out of the excitation in the Mott insulator picture. In the context of the high temperature superconductor, it is more suitable to adopt the first convention and I shall derive the t-J model from this picture in the following section. There is a different approach to reach the same final result in deriving the t-J model in the second case, which will be the second order perturbation from the Hubbard model. This will be summarized in Appendix A for the sake of completeness on this issue.

### 2.1.2 From the Two-Band Model to Effective One-Band t-J Model

The three-band model contains many interactions and it is rather involved to solve. So further reduction of the degrees of the freedom in the model was considered. There are only two types of orbitals left, the copper d orbital and the oxygen p orbital. The ultimate question is whether those two are equally important or if one of them can be reduced. F.C. Zhang and T.M Rice [34] developed a method to recover the effective single band model which was first proposed by Anderson[81]. Their starting point is a two-band model which

only considers the hybridization of nearest neighbor Cu 3d and O 2p sites, the on-site Coulomb repulsions at Cu sites, and the single occupied energy level of Cu and O sites. Different from the three-band model, the initial two-band model in Eq. 2.2 omits the effect of higher energy states on the low energy excitations. This approximation is debated, but according to experimental result in Fig. 1.8, the reduction to the effective one-band model is supported (as discussed in the first chapter).

$$\begin{aligned}
H_{2b} &= H_t + H_p \\
H_t &= \sum_{i,j} (-1)^{M_{i,j}} t_{pd} (d_{i\sigma}^\dagger p_{j\sigma} + h.c.) \\
H_p &= \epsilon_d \sum_{i,\sigma} n_{d,i\sigma} + \epsilon_p \sum_{j\sigma} n_{p,j\sigma} + U_d \sum_i n_{d,i\uparrow} n_{d,i\downarrow}
\end{aligned} \tag{2.2}$$

where

$$\begin{aligned}
M_{i,j} &= 1, (j = i + \frac{1}{2}\hat{x}, \hat{y}) \\
M_{i,j} &= 2, (j = i - \frac{1}{2}\hat{x}, \hat{y})
\end{aligned} \tag{2.3}$$

$$\begin{aligned}
H_p &= J \sum_{\langle ij \rangle} \mathbf{S}_i \cdot \mathbf{S}_j \\
J &= \frac{4t_{dp}^4}{\epsilon_p^2 U_d} + \frac{4t_{dp}^4}{2\epsilon_p^3}
\end{aligned} \tag{2.4}$$

In Equation. 2.2, the hybridization part  $H_t$  describes the hopping process between a Cu hole and a O hole. From the definition of the symmetry in Fig. 2.3(a), the up bond and the right bond have negative  $t_{pd}$  while the left bond and the down bond have a positive one. An O hole can be either

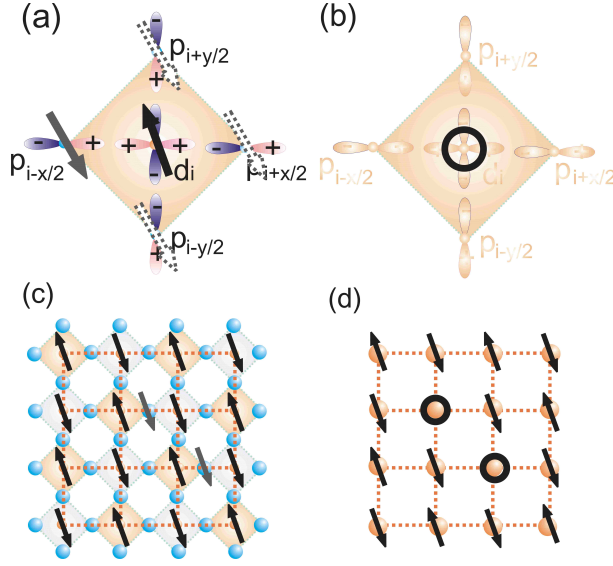


Figure 2.3: (a) Schematic diagram of the hybridization of the O hole ( $2p^5$ ) and Cu hole ( $3d^9$ ), the signs + and - represent the phase of the wave function [34]. Upon doping one hole into the O site, this doped hole can resonate on the four O sites around a Cu, the dashed arrow refers to the motion of the resonance. (b) The resonating spin combined with the spin of a hole residing on Cu forms a spin singlet on the copper site, it is equivalent to taking out the copper d hole with spin and leaving a spinless hole. (c) Doping oxygen p holes into a half filled system results in doping holes onto the copper site (d). In the final result (d) the system is simplified into a two dimensional square lattice with only copper site involved.

in a symmetric(-) or an antisymmetric(+) state with respect to a Cu hole, and either of them can combine a Cu hole to form a spin singlet (S) or a spin triplet (T) state. After choosing an orthogonal and complete function  $\phi_{i\sigma}$  to represent symmetric O hole space, the symmetric singlet state can be written as Equation. 2.7. The hopping motion of a singlet with its neighbors can be expressed as Equation. 2.5, where  $t_{ij}$  are hopping integrals which can be determined within second order perturbation theory. Creation of a Cu d hole on site i means annihilation of a singlet state. In other words,  $\Psi_i^-$  is equivalent of an empty site without any Cu d hole. So Equation. 2.5 can be reduced to Equation 2.6. The operator  $(1 - n_{i,\bar{\sigma}})$  explicitly excludes double

occupation on site  $i$ .

$$H_t = \sum_{i \neq j, \sigma} t_{ij} ((\Psi_j^- d_{i\sigma}^\dagger)^+ (\Psi_i^- p_{j\sigma})) \quad (2.5)$$

$$= \sum_{i \neq j, \sigma} t_{ij} (1 - n_{i, \bar{\sigma}}) d_{i\sigma}^\dagger d_{j\sigma} (1 - n_{j, \bar{\sigma}}) \quad (2.6)$$

$$\Psi_i^- = (1/\sqrt{2})(\Phi_{i\uparrow} d_{i\downarrow} - \Phi_{i\downarrow} d_{i\uparrow}) \quad (2.7)$$

In Equation. 2.2, the potential part  $H_p$  describes the on-site potential for the Cu hole and the O hole, also the inter-site repulsion between them. It is well known that at half filling it can be reduced to  $S = \frac{1}{2}$  Heisenberg model on the square lattice [82], see Equation. 2.4.

The basic idea of Zhang and Rice is that when doping one hole into the O site from half filling (one hole per Cu site, empty in O site), that doped hole can resonate on the four O sites around a Cu site (see Fig. 2.3(a)). In order to form a stable state, the resonating spin combined with the spin of the hole residing on Cu forms a spin singlet. So instead of a hole located originally on the oxygen site, there is a spin singlet state centered on the Cu site. It is equivalent to subtracting one spin  $-\frac{1}{2}$  from the Cu site to have an empty spin site. This is the so called hole in the Heisenberg spin system (see Fig. 2.3(b)). The 2D  $CuO_2$  plane is reduced to a system which consists of antiferromagnetic spins on the copper sites at half filling and doped holes on top of that when the system goes away from half filling to the p-doped side (see Fig. 2.3(c)(d)). The oxygen hole is totally out of the picture. In this sense, the two-band model has been reduced to an effective one-band model: the t-J model.

$$H_{tJ} = \sum_{i \neq j, \sigma} t_{ij} (1 - n_{i, \bar{\sigma}}) d_{i\sigma}^\dagger d_{j\sigma} (1 - n_{j, \bar{\sigma}}) + \sum_{\langle ij \rangle} J \mathbf{S}_i \cdot \mathbf{S}_j \quad (2.8)$$

## 2.2 The Renormalized Mean Field Method with Gutzwiller Approximation

The t-J model is considered to be the simplest model available to treat cuprates. Although quite simple in its expression, the exact treatment of it is only limited to very special cases. There are two difficulties: The first difficulty is the question of how to project out the double occupancy on the same site in order to work in a reduced Hilbert space. The second difficulty is the question of how to treat the four-fermion interaction term  $\mathbf{S}_i \cdot \mathbf{S}_j$ . The renormalized mean-field theory (RMFT) is a powerful tool to resolve these difficulties with some sensible approximations. The key issue here is the correct evaluation of the expectation values of operators with respect to the trial wave function  $|\Psi\rangle$ . With our constraint of reduced Hilbert space, a projection  $\hat{P}$  needs to act on the non-interacting wave function, resulting in  $|\Psi\rangle = \hat{P}|\Psi_0\rangle$ .  $|\Psi_0\rangle$  is an uncorrelated state, for example a Slater determinate of single particle states. The expression of the object operator's ( $\hat{\mathcal{O}}$ ) expectation value follows the following term:

$$\langle \hat{\mathcal{O}} \rangle_R \equiv \frac{\langle \Psi | \hat{\mathcal{O}} | \Psi \rangle}{\langle \Psi | \Psi \rangle} = \frac{\langle \Psi_0 | \hat{P} \hat{\mathcal{O}} \hat{P} | \Psi_0 \rangle}{\langle \Psi_0 | \hat{P}^2 | \Psi_0 \rangle} \approx g^{\mathcal{O}}(\mathbf{M}) \frac{\langle \Psi_0 | \hat{\mathcal{O}} | \Psi_0 \rangle}{\langle \Psi_0 | \Psi_0 \rangle} = g^{\mathcal{O}}(\mathbf{M}) \langle \hat{\mathcal{O}} \rangle \quad (2.9)$$

Here the expectation value, which is supposed to be evaluated on the projected space  $\langle \hat{\mathcal{O}} \rangle_R$ , is successfully reduced to the expectation value evaluated on the unprojected space  $\langle \hat{\mathcal{O}} \rangle$  with a renormalization factor  $g^{\mathcal{O}}(\mathbf{M})$  in front.  $\mathbf{M} = (M_1, M_2, M_3, \dots)$  are the relevant mean fields. Here I follow one of the renormalization schemes, the so called the Gutzwiller approximation to implement the blueprint which was laid out in Equation. 2.9.

### 2.2.1 Uniform Gutzwiller Approximation

In the last section, I derived an effective Hamiltonian for cuprates. The t-J model is applied on a reduced Hilbert space, excluding double occupation. Although having a reduced Hilbert space is easy to conceptualize, it is not trivial to treat analytically. The Gutzwiller approximation is a very powerful tool to project out double occupation. Gutzwiller [83][84] and Ogata [85] have derived the renormalization factor using a classical weight counting method. Vollhardt [86] has given a clear physical explanation of this issue. They reach a consistent result in the uniform case.

The Gutzwiller factor acts like a classical weighting factor which ensures the expectation value of the kinetic energy term and superexchange term are correctly estimated. [87] The projection is defined as  $|\Psi\rangle = P_G|\Psi_0\rangle$ . The renormalization of these two major terms in the t-J model is as follows:

$$\langle\Psi_0|P_G C_{i\sigma}^\dagger C_{j\sigma} P_G|\Psi_0\rangle = g_t \langle\Psi_0|C_{i\sigma}^\dagger C_{j\sigma}|\Psi_0\rangle_0 \quad (2.10)$$

$$\langle\Psi_0|P_G \mathbf{S}_i \cdot \mathbf{S}_j P_G|\Psi_0\rangle = g_J \langle\Psi_0|\mathbf{S}_i \cdot \mathbf{S}_j|\Psi_0\rangle_0 \quad (2.11)$$

The first term is the hopping process. Starting with site i empty and site j singly occupied with a spin up electron, the spin up electron hops from j site to i site. If there is no exclusion of double occupation, the Pauli principle prohibits the process to occur when i site is occupied by a spin up electron. If the probability of site i occupied by a spin up electron is  $n_{i\uparrow}$ , then the probability of site i being not occupied by a spin up electron is  $1 - n_{i\uparrow} = (1 + x)/2$  when spin up and spin down are degenerate. Here x is the doping of holes. After the projection, the double occupation is excluded. The hopping only happens when site i is occupied by a hole. That probability is x indeed. To give the right expectation value of the hopping term using the projected wave

function, there should be a factor of  $\frac{x}{(1+x)^{1/2}}$  in front of the expectation value of the hopping term using the bare wave function. This gives us  $g_t = \frac{2x}{1+x}$ .

The second process is the superexchange process. Initially I start with site i occupied by a spin up electron and site j occupied by a spin down electron. After a superexchange, site i is occupied by a spin down electron and site j is occupied by a spin up electron. The net effect is the orientation of the spin flipped during the process. Without excluding the double occupation, the process can be broken down into two steps. Step one: the spin up electron on site i hops into site j with a probability  $n_{i\uparrow}(1 - n_{j\uparrow})$ . Step two: the spin down electron on site j hops into site i with a probability  $n_{j\downarrow}(1 - n_{i\downarrow})$ . So the total probability of the process to happen is  $n_{i\uparrow}(1 - n_{j\uparrow})n_{j\downarrow}(1 - n_{i\downarrow})$ . If double occupation is prohibited, the probability for this process to happen is instead  $n_{i\uparrow}n_{j\downarrow}$ . To give the right expectation value of the superexchange term, using the projected wave function, there should be a factor of  $\frac{n_{i\uparrow}n_{j\downarrow}}{n_{i\uparrow}(1-n_{j\uparrow})n_{j\downarrow}(1-n_{i\downarrow})}$  in front of the expectation value of the superexchange term using the bare wave function. That gives us  $g_J = \frac{4}{(1+x)^2}$ .

This uniform Gutzwiller factor can be achieved by setting the hole density to be the same value at every lattice site in the spatially unrestricted Gutzwiller factor. This will be further explained in the next section.

### 2.2.2 Spatially Unrestricted Gutzwiller Approximation

Strongly correlated electrons in cuprates have novel response to inhomogeneity, the resulting physics cannot be overlooked. The uniform Gutzwiller approximation, which gives exactly the same projection on every lattice site, is not justified in the presence of inhomogeneity. The concept of statistical counting in the classical regime depends on the correlation strength. The correlation strength is dependant on the spatial density of each individual lattice site. This needs to be taken into account beginning with the construc-

tion of the trial wave function. Due to the spatially inhomogeneous nature of cuprates, the spatially unrestricted Gutzwiller approximation (SUGA) is needed. Following the method of F.C Zhang et al [88], I will derive the renormalization factors for t-J model in the spatially unrestricted case.

In t-J model, I separate the Hamiltonian into two different parts: the kinetic energy part  $H_t$  and the exchange part  $H_J$ .

$$\begin{aligned}
H &= H_t + H_J \\
H_t &= -t \sum_{\langle ij \rangle \sigma} (c_{i\sigma}^\dagger c_{j\sigma} + h.c.) \\
H_J &= J \sum_{\langle i,j \rangle \sigma} (\mathbf{S}_i \cdot \mathbf{S}_j - \frac{1}{4} n_i n_j)
\end{aligned} \tag{2.12}$$

When constructing a trial wave function describing correlated states  $|\Psi\rangle$  from uncorrelated states  $|\Psi_0\rangle$ , the projection operator is site dependent, defined by

$$|\Psi\rangle = \prod_i \hat{P}_i |\Psi_0\rangle \tag{2.13}$$

The definition of  $\hat{P}_i$  is given by

$$\hat{P}_i = y_{i\uparrow}^{\hat{n}_{i\uparrow}} \cdot y_{i\downarrow}^{\hat{n}_{i\downarrow}} \cdot (1 - \hat{n}_{i\uparrow} \hat{n}_{i\downarrow}) \tag{2.14}$$

$y_{i\sigma}$  is the site and spin dependent fugacity. The purpose of introducing it is to keep the electron density before and after the projection identical,  $\langle \hat{n}_{i\sigma} \rangle = \langle \hat{n}_{i\sigma} \rangle_0$ .  $\hat{n}_{i\sigma}$  is the density operator which counts the number of the spin  $\sigma$  electrons on site  $i$ . Since the density operator can only result in an empty 0 or occupied 1 state, I can simplify the exponential function as follows:

$$y_{i\sigma}^{\hat{n}_{i\sigma}} = 1 - (1 - y_{i\sigma})\hat{n}_{i\sigma} \quad (2.15)$$

Using the commutation relation of fermions, I can transform the projection operator  $\hat{P}_i$  in Equation. 2.14 into the form composed of empty operator  $\hat{E}_i$  and single occupation operator  $\hat{Q}_{i\sigma}$ ,

$$\begin{aligned} \hat{P}_i &= \hat{E}_i + y_{i\uparrow}\hat{Q}_{i\uparrow} + y_{i\downarrow}\hat{Q}_{i\downarrow} \\ \hat{E}_i &= (1 - n_{i\uparrow})(1 - n_{i\downarrow}) \\ \hat{Q}_{i\uparrow} &= \hat{n}_{i\uparrow}(1 - \hat{n}_{i\downarrow}) \\ \hat{Q}_{i\downarrow} &= \hat{n}_{i\downarrow}(1 - \hat{n}_{i\uparrow}) \end{aligned} \quad (2.16)$$

Note that if I set the fugacity of the up spin and down spin to be equal to each other ( $y_{i\uparrow} = y_{i\downarrow} = y_i$ ), the spin dependent fugacity can be reduced to the spin independent one, which is the case for the paramagnetic state where the up and down spins are degenerate. Now I calculate the expectation values of the occupation operators in the unprojected space:

$$\begin{aligned} e_{i0} &= \langle \Psi_0 | \hat{E}_i | \Psi_0 \rangle = (1 - n_{i\sigma 0})(1 - n_{i\bar{\sigma} 0}) \\ q_{i\sigma 0} &= \langle \Psi_0 | \hat{Q}_{i\sigma} | \Psi_0 \rangle = n_{i\sigma 0}(1 - n_{i\bar{\sigma} 0}) \end{aligned} \quad (2.17)$$

Similarly, I can calculate the expectation values of the occupation oper-

ators in the projected space:

$$\begin{aligned}
e_i &= z_i^{-1} \langle \Psi_0 | \hat{P}_i \hat{E}_i \hat{P}_i | \Psi_0 \rangle = z_i^{-1} \langle \Psi_0 | \hat{E}_i | \Psi_0 \rangle = \frac{e_{i0}}{z_i} \\
q_{i\sigma} &= z_i^{-1} \langle \Psi_0 | \hat{P}_i \hat{Q}_{i\sigma} \hat{P}_i | \Psi_0 \rangle = z_i^{-1} \langle \Psi_0 | y_{i\sigma}^2 \hat{Q}_{i\sigma} | \Psi_0 \rangle = \frac{y_{i\sigma}^2 q_{i\sigma 0}}{z_i}
\end{aligned} \tag{2.18}$$

Note in Equation. 2.18, the renormalization factor  $Z = \prod_i z_i$ , where

$$z_i = \langle \Psi_0 | \hat{P}_i \cdot \hat{P}_i | \Psi_0 \rangle = e_{i0} + y_{i\uparrow}^2 q_{i\uparrow 0} + y_{i\downarrow}^2 q_{i\downarrow 0} \tag{2.19}$$

Using the basic fermion commutation relation  $\{C_i^\dagger, C_i\} = 1$  and Pauli principle the following building blocks are derived. They are helpful tools in later calculations.

$$\hat{P}_i C_{i\sigma}^\dagger \hat{P}_i = [y_{i\sigma}(1 - n_{i\bar{\sigma}})] C_{i\sigma}^\dagger \tag{2.20}$$

$$\hat{P}_i C_{i\sigma} \hat{P}_i = [y_{i\sigma}(1 - n_{i\bar{\sigma}})] C_{i\sigma} \tag{2.21}$$

$$\hat{P}_i n_i \hat{P}_i = \sum_{\sigma} y_{i\sigma}^2 Q_{i\sigma} \tag{2.22}$$

$$\hat{P}_i S_i^+ \hat{P}_i = y_{i\sigma} y_{i\bar{\sigma}} S_i^+ \tag{2.23}$$

$$\hat{P}_i S_i^- \hat{P}_i = y_{i\sigma} y_{i\bar{\sigma}} S_i^- \tag{2.24}$$

Equipped with these equations, next I am going to derive the projection factor for  $H_t$  and  $H_J$ .

$$\begin{aligned}
& \langle \Psi | C_{i\sigma}^\dagger C_{j\sigma} | \Psi \rangle \\
&= \langle \Psi_0 | \hat{P}_i C_{i\sigma}^\dagger \hat{P}_i \hat{P}_j C_{j\sigma} \hat{P}_j | \Psi_0 \rangle / z_i z_j \\
&= g_{t\sigma}(i) g_{t\sigma}(j) \langle \Psi_0 | C_{i\sigma}^\dagger C_{j\sigma} | \Psi_0 \rangle \tag{2.25} \\
g_t(i) &= \frac{y_{i\sigma}(1 - n_{i\bar{\sigma}})}{z_i} = \sqrt{\frac{e_i q_{i\sigma}}{e_{i0} q_{i\sigma 0}}} (1 - n_{i\bar{\sigma}}) \\
&= \sqrt{\frac{n_{i\sigma}(1 - n_i)}{n_{i\sigma}(1 - n_{i\sigma})}} = \sqrt{\frac{2x_i}{1 + x_i}} \\
g_t(j) &= \frac{y_{j\sigma}(1 - n_{j\bar{\sigma}})}{z_j} = \sqrt{\frac{e_j q_{j\sigma}}{e_{j0} q_{j\sigma 0}}} (1 - n_{j\bar{\sigma}}) \\
&= \sqrt{\frac{n_{j\sigma}(1 - n_j)}{n_{j\sigma}(1 - n_{j\sigma})}} = \sqrt{\frac{2x_j}{1 + x_j}} \tag{2.26}
\end{aligned}$$

In order to get the renormalization factor in front the superexchange term, I break the exchange term into two parts, the  $S^{+-}$  part and the  $S^{zz}$  part (  $\mathbf{S}_i \mathbf{S}_j = \mathbf{S}_i^+ \mathbf{S}_j^- + \mathbf{S}_i^z \mathbf{S}_j^z$  ). Although there are different ways to interpret the renormalization factor for the  $S^{zz}$  part, there is indeed consensus on the renormalization factor for the first  $S^{+-}$  part:

$$\begin{aligned}
& \langle \Psi | S_i^+ \cdot S_j^- | \Psi \rangle \\
&= \langle \Psi_0 | \hat{P}_i S_i^+ \hat{P}_i \hat{P}_j S_j^- \hat{P}_j | \Psi_0 \rangle / z_i z_j \\
&= g_J^{+-}(i) g_J^{+-}(j) \langle \Psi_0 | S_i^+ \cdot S_j^- | \Psi_0 \rangle \\
g_J^{+-}(i) &= \frac{y_{i\uparrow} y_{i\downarrow}}{z_i} = \sqrt{\frac{q_{i\uparrow} q_{i\downarrow}}{q_{i\uparrow 0} q_{i\downarrow 0}}} \\
&= \sqrt{\frac{n_{i\uparrow}}{n_{i\uparrow}(1-n_{i\downarrow})} \frac{n_{i\downarrow}}{n_{i\downarrow}(1-n_{i\uparrow})}} \\
&= \sqrt{\frac{1}{(1-n_{i\uparrow})(1-n_{i\downarrow})}} = \frac{1}{1-\frac{n_i}{2}} = \frac{2}{1+x_i} \\
g_J^{+-}(j) &= \frac{y_{j\uparrow} y_{j\downarrow}}{z_j} = \sqrt{\frac{q_{j\uparrow} q_{j\downarrow}}{q_{j\uparrow 0} q_{j\downarrow 0}}} \\
&= \sqrt{\frac{n_{j\uparrow}}{n_{j\uparrow}(1-n_{j\downarrow})} \frac{n_{j\downarrow}}{n_{j\downarrow}(1-n_{j\uparrow})}} \\
&= \sqrt{\frac{1}{(1-n_{j\uparrow})(1-n_{j\downarrow})}} = \frac{1}{1-\frac{n_j}{2}} = \frac{2}{1+x_j} \tag{2.27}
\end{aligned}$$

The renormalization factor for the  $S^{zz}$  part has several interpretations and the derivation is rather involved [89]. In the paramagnetic state there is spin-rotation symmetry. The renormalization factor in front of  $S_i^z S_j^z$  should be the same as the one in front of  $S_i^+ S_j^-$ . In summary, the spatially unrestricted Gutzwiller factors can be written as:

$$\begin{aligned}
g_{ij}^t &= \frac{\langle \Psi | C_{i\sigma}^\dagger C_{j\sigma} | \Psi \rangle}{\langle \Psi_0 | C_{i\sigma}^\dagger C_{j\sigma} | \Psi_0 \rangle} = \sqrt{\frac{4x_i x_j}{(1+x_i)(1+x_j)}} \\
g_{ij}^J &= \frac{\langle \Psi | \mathbf{S}_i \cdot \mathbf{S}_j | \Psi \rangle}{\langle \Psi_0 | \mathbf{S}_i \cdot \mathbf{S}_j | \Psi_0 \rangle} = \frac{4}{(1+x_i)(1+x_j)} \tag{2.28}
\end{aligned}$$

Again, if this is a uniform state ( $x_i = x_j = x$ ), the uniform Gutzwiller factor can be recovered:

$$\begin{aligned}g_t &= 2x/(1+x) \\g_J &= 4/(1+x)^2\end{aligned}\tag{2.29}$$

### 2.2.3 The Mean Field Decoupling of S · S Superexchange Term in the t-J Model

The Gutzwiller approximation has taken care of the strongest correlation in the system. Now I can move onto how to treat the four-fermion term in the t-J model. The superexchange term in the t-J model is:

$$J \sum_{\langle i,j \rangle \sigma} (\mathbf{S}_i \cdot \mathbf{S}_j - \frac{1}{4} n_i n_j) = \frac{1}{2} (C_{i\sigma}^\dagger C_{i\bar{\sigma}} C_{j\bar{\sigma}}^\dagger C_{j\sigma} - n_{i\sigma} n_{j\bar{\sigma}}) \quad (2.30)$$

$\mathbf{S}_i$  is defined as  $\mathbf{S}_i = \frac{1}{2} C_{i\alpha}^\dagger \sigma_{\alpha\beta} C_{i\beta}$ , where  $\sigma$  are the Pauli matrices. There is an extra  $-\frac{1}{4} n_i n_j$  term in addition to the exchange term in Equation. 2.8. Since  $\mathbf{S}_i \cdot \mathbf{S}_j = \frac{1}{2} C_{i\sigma}^\dagger C_{i\bar{\sigma}} C_{j\bar{\sigma}}^\dagger C_{j\sigma} + \frac{1}{4} n_{i\sigma} n_{j\sigma} - \frac{1}{4} n_{i\sigma} n_{j\bar{\sigma}}$ , and  $\frac{1}{4} n_i n_j = \frac{1}{4} n_{i\sigma} n_{j\sigma} + \frac{1}{4} n_{i\sigma} n_{j\bar{\sigma}}$ , with an extra  $-\frac{1}{4} n_i n_j$  term, the indices in front of  $C_{i\sigma}^\dagger C_{i\bar{\sigma}} C_{j\bar{\sigma}}^\dagger C_{j\sigma}$  and  $-n_{i\sigma} n_{j\bar{\sigma}}$  are tuned to be the same. Also, it is consistent with the t-J model derived from the Hubbard model using second perturbation theory.

These two four-fermion terms can be written into the mean field format. Using  $AB+CD = \frac{1}{2}(A+C)(B+D) + \frac{1}{2}(A-C)(B-D)$ , the first four-fermion term can be written as the following:

$$\begin{aligned} & \frac{1}{2} C_{i\sigma}^\dagger C_{i\bar{\sigma}} C_{j\bar{\sigma}}^\dagger C_{j\sigma} \\ = & -\frac{1}{2} (C_{i\uparrow}^\dagger C_{j\uparrow} C_{j\downarrow}^\dagger C_{i\downarrow} + C_{i\downarrow}^\dagger C_{j\downarrow} C_{j\uparrow}^\dagger C_{i\uparrow}) \\ = & -\frac{1}{4} (C_{i\uparrow}^\dagger C_{j\uparrow} + C_{i\downarrow}^\dagger C_{j\downarrow}) (C_{j\downarrow}^\dagger C_{i\downarrow} + C_{j\uparrow}^\dagger C_{i\uparrow}) \\ & -\frac{1}{4} (C_{i\uparrow}^\dagger C_{j\uparrow} - C_{i\downarrow}^\dagger C_{j\downarrow}) (C_{j\downarrow}^\dagger C_{i\downarrow} - C_{j\uparrow}^\dagger C_{i\uparrow}) \end{aligned} \quad (2.31)$$

If I define the mean field order parameter representing the bond order as the

following :

$$\begin{aligned}
\chi_{ij}^+ &\equiv \langle C_{i\uparrow}^\dagger C_{j\uparrow} + C_{i\downarrow}^\dagger C_{j\downarrow} \rangle \\
(\chi_{ij}^+)^* &\equiv \langle C_{j\downarrow}^\dagger C_{i\downarrow} + C_{j\uparrow}^\dagger C_{i\uparrow} \rangle \\
\chi_{ij}^- &\equiv \langle C_{i\uparrow}^\dagger C_{j\uparrow} - C_{i\downarrow}^\dagger C_{j\downarrow} \rangle \\
(\chi_{ij}^-)^* &\equiv -\langle C_{j\downarrow}^\dagger C_{i\downarrow} - C_{j\uparrow}^\dagger C_{i\uparrow} \rangle
\end{aligned} \tag{2.32}$$

The first four-fermion term becomes:

$$\begin{aligned}
&\frac{1}{2} C_{i\sigma}^\dagger C_{i\bar{\sigma}} C_{j\bar{\sigma}}^\dagger C_{j\sigma} \\
&= -\frac{1}{4} [(\chi_{ij}^+)^* (C_{i\uparrow}^\dagger C_{j\uparrow} + C_{i\downarrow}^\dagger C_{j\downarrow}) + h.c. - |\chi_{ij}^+|^2] \\
&\quad + \frac{1}{4} [(\chi_{ij}^-)^* (C_{i\uparrow}^\dagger C_{j\uparrow} - C_{i\downarrow}^\dagger C_{j\downarrow}) + h.c. - |\chi_{ij}^-|^2]
\end{aligned} \tag{2.33}$$

In the same way, the second four-fermion term can be written:

$$\begin{aligned}
&-\frac{1}{2} \sum_{\sigma} n_{i\sigma} n_{j\bar{\sigma}} \\
&= -\frac{1}{2} (C_{i\uparrow}^\dagger C_{j\downarrow}^\dagger C_{j\downarrow} C_{i\uparrow} + C_{i\downarrow}^\dagger C_{j\uparrow}^\dagger C_{j\uparrow} C_{i\downarrow}) \\
&= -\frac{1}{4} (C_{i\uparrow}^\dagger C_{j\downarrow}^\dagger + C_{i\downarrow}^\dagger C_{j\uparrow}^\dagger) (C_{j\downarrow} C_{i\uparrow} + C_{j\uparrow} C_{i\downarrow}) \\
&\quad -\frac{1}{4} (C_{i\uparrow}^\dagger C_{j\downarrow}^\dagger - C_{i\downarrow}^\dagger C_{j\uparrow}^\dagger) (C_{j\downarrow} C_{i\uparrow} - C_{j\uparrow} C_{i\downarrow})
\end{aligned} \tag{2.34}$$

If I define the mean field order parameter representing the pairing order as the following:

$$\begin{aligned}
\Delta_{ij}^+ &\equiv \langle C_{i\uparrow}^\dagger C_{j\downarrow}^\dagger + C_{i\downarrow}^\dagger C_{j\uparrow}^\dagger \rangle \\
(\Delta_{ij}^+)^* &\equiv C_{j\downarrow} C_{i\uparrow} + C_{j\uparrow} C_{i\downarrow} \\
\Delta_{ij}^- &\equiv \langle C_{i\uparrow}^\dagger C_{j\downarrow}^\dagger - C_{i\downarrow}^\dagger C_{j\uparrow}^\dagger \rangle \\
(\Delta_{ij}^-)^* &\equiv \langle C_{j\downarrow} C_{i\uparrow} - C_{j\uparrow} C_{i\downarrow} \rangle
\end{aligned} \tag{2.35}$$

The second four-fermion term becomes:

$$\begin{aligned}
&-\frac{1}{2} \sum_{\sigma} n_{i\sigma} n_{j\bar{\sigma}} \\
&= -\frac{1}{4} (\Delta_{ij}^+)^* (C_{i\uparrow}^\dagger C_{j\downarrow}^\dagger + C_{i\downarrow}^\dagger C_{j\uparrow}^\dagger) + h.c. - |\Delta_{ij}^+|^2 \\
&\quad -\frac{1}{4} (\Delta_{ij}^-)^* (C_{i\uparrow}^\dagger C_{j\downarrow}^\dagger - C_{i\downarrow}^\dagger C_{j\uparrow}^\dagger) + h.c. - |\Delta_{ij}^-|^2
\end{aligned} \tag{2.36}$$

I sum over these two terms to get the mean field decoupled  $\mathbf{S} \cdot \mathbf{S}$  term:

$$\begin{aligned}
&J \sum_{\langle i,j \rangle_{\sigma}} (\mathbf{S}_i \cdot \mathbf{S}_j - \frac{1}{4} n_i n_j) \\
&= -\frac{1}{4} J [(\chi_{ij}^+)^* (C_{i\uparrow}^\dagger C_{j\uparrow}^\dagger + C_{i\downarrow}^\dagger C_{j\downarrow}^\dagger) + h.c. - |\chi_{ij}^+|^2] \\
&\quad + \frac{1}{4} J [(\chi_{ij}^-)^* (C_{i\uparrow}^\dagger C_{j\uparrow}^\dagger - C_{i\downarrow}^\dagger C_{j\downarrow}^\dagger) + h.c. - |\chi_{ij}^-|^2] \\
&\quad - \frac{1}{4} J [(\Delta_{ij}^+)^* (C_{i\uparrow}^\dagger C_{j\downarrow}^\dagger + C_{i\downarrow}^\dagger C_{j\uparrow}^\dagger) + h.c. - |\Delta_{ij}^+|^2] \\
&\quad - \frac{1}{4} J [(\Delta_{ij}^-)^* (C_{i\uparrow}^\dagger C_{j\downarrow}^\dagger - C_{i\downarrow}^\dagger C_{j\uparrow}^\dagger) + h.c. - |\Delta_{ij}^-|^2]
\end{aligned} \tag{2.37}$$

Here I use spin dependant notation to write the order parameter:

$$\begin{aligned}
\chi_{ij\sigma} &= \langle C_{i\sigma}^\dagger C_{j\sigma} \rangle \\
\Delta_{ij\sigma} &= \langle C_{i\sigma} C_{j\bar{\sigma}} \rangle
\end{aligned}
\tag{2.38}$$

Then the order parameters in Equation. 2.42 can be written as:

$$\begin{aligned}
\chi_{ij}^+ &= \chi_{ij\uparrow} + \chi_{ij\downarrow} \\
\chi_{ij}^- &= \chi_{ij\uparrow} - \chi_{ij\downarrow} \\
\Delta_{ij}^+ &= \Delta_{ij\uparrow} + \Delta_{ij\downarrow} \\
\Delta_{ij}^- &= \Delta_{ij\uparrow} - \Delta_{ij\downarrow}
\end{aligned}
\tag{2.39}$$

In the paramagnetic state, the  $SU(2)$  symmetry requires setting up the order parameters in the following way:

$$\begin{aligned}
\chi_{ij\uparrow} &= \chi_{ij\downarrow} \\
\Delta_{ij\uparrow} &= -\Delta_{ij\downarrow}
\end{aligned}
\tag{2.40}$$

I can drop the  $+-$  sign in my definition of order parameters in Equation. 2.42 to get the more conventional notation:

$$\begin{aligned}
\chi_{ij} &= \langle C_{i\uparrow}^\dagger C_{j\uparrow} + C_{i\downarrow}^\dagger C_{j\downarrow} \rangle \\
\Delta_{ij} &= \langle C_{i\uparrow}^\dagger C_{j\downarrow}^\dagger - C_{i\downarrow}^\dagger C_{j\uparrow}^\dagger \rangle
\end{aligned}
\tag{2.41}$$

As a result, the  $\mathbf{S} \cdot \mathbf{S}$  term becomes multiple two-fermion terms coupled with the mean fields. At this point I have tackled the last difficulty in solving the t-J model.

$$\begin{aligned}
& J \sum_{\langle i,j \rangle \sigma} (\mathbf{S}_i \cdot \mathbf{S}_j - \frac{1}{4} n_i n_j) \\
= & -\frac{1}{4} J [\chi_{ij}^* (C_{i\uparrow}^\dagger C_{j\uparrow} + C_{i\downarrow}^\dagger C_{j\downarrow}) + h.c. - |\chi_{ij}|^2] \\
& -\frac{1}{4} J [\Delta_{ij}^* (C_{i\uparrow}^\dagger C_{j\downarrow} - C_{i\downarrow}^\dagger C_{j\uparrow}) + h.c. - |\Delta_{ij}|^2]
\end{aligned} \tag{2.42}$$

## 2.2.4 The Renormalized Mean Field Hamiltonian with SUGA

From the most standard format of t-J model:

$$H = \hat{P} \left\{ - \sum_{i \neq j} t_{ij} C_{i\sigma}^\dagger C_{j\sigma} + J \sum_{\langle i,j \rangle} (\mathbf{S}_i \cdot \mathbf{S}_j - \frac{1}{4} \hat{n}_i \hat{n}_j) \right\} \hat{P} \tag{2.43}$$

Incorporating the two parts of the approximation: the SUGA part and the mean field decoupling part. I get the renormalized mean field t-J model I am going to use throughout the following chapters:

$$\begin{aligned}
H_{GA} = & - \sum_{i \neq j} g_{ij}^t t_{ij} C_{i\sigma}^\dagger C_{j\sigma} - \sum_i \mu_f C_{i\sigma}^\dagger C_{i\sigma} + \sum_i \lambda_i C_{i\sigma}^\dagger C_{i\sigma} \\
& - \frac{1}{4} J \sum_{\langle i,j \rangle} g_{ij}^\chi (\chi_{ij}^* C_{i\sigma}^\dagger C_{j\sigma} + h.c. - |\chi_{ij}|^2) \\
& - \frac{1}{4} J \sum_{\langle i,j \rangle} g_{ij}^\Delta (\Delta_{ij}^* \epsilon_{\sigma\sigma'} C_{i\sigma}^\dagger C_{j\sigma'} + h.c. - |\Delta_{ij}|^2)
\end{aligned} \tag{2.44}$$

$C_{i\sigma}^\dagger$  creates an electron that hops between near neighbors via  $t_{ij}$  with repeated spin indices summed. The density operator and the electron density at site  $i$  is  $\hat{n}_i = C_{i\sigma}^\dagger C_{i\sigma}$ . The local doping concentration is given by  $x_i = 1 - n_i$ . The average doping is  $x = (1/N_s) \sum_i x_i$  on a square lattice of  $N_s$  sites.  $g_{ij}^X = g_{ij}^\Delta = g_{ij}^J$  in the Gutzwiller approximation reflects the SU(2) symmetry at half filling.  $\mu_f$  is the chemical potential which keeps the doping to be the desired one.  $\lambda_i$  is the local fugacity which is necessary when there is inhomogeneity.

There are three mean fields  $\{\Delta_{ij}, \chi_{ij}, x_i\}$ , they can be solved self-consistently by minimizing the energy. There are no spatial restrictions on any of these mean fields unless I am particularly interested in the uniform case. The strong correlation is built in the renormalization factor  $g_{ij}^X$  and  $g_{ij}^\Delta$ . Since they depend on one of the mean fields, the local density, they are optimized simultaneously when the global energy minimum is reached upon solving the mean field order parameters self-consistently.

### 2.2.5 Two Valence Bond Channels with the Same Origin Become Different Away from Half Filling

In the undoped case at half filling, the kinetic energy is completely quenched, leading to a Mott insulator. The superexchange interaction causes the spins to order antiferromagnetically in the ground state (see Fig. 2.4(a)), this can be described by the Heisenberg model.

For more than two decades, theories have been guided by the idea that the strong quantum fluctuations of the spin-1/2 moments make the spin-singlet valence bond state close in energy to the antiferromagnetic state. Following the mean field decomposition in Equation. 2.45, the valence bond can form via either spin singlet pairing  $\Delta_{ij}$  or the orbital hybridization  $\chi_{ij}$ . This has been envisioned by Pauling in the context of chemical bonding in molecules

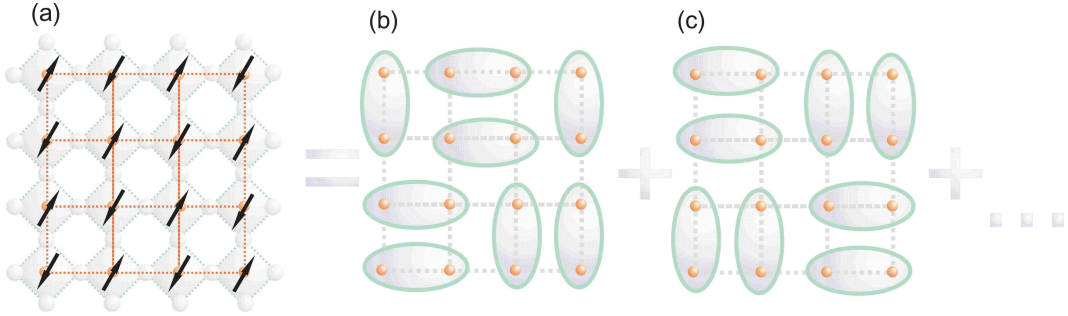


Figure 2.4: *Cuprates at half filling.* (a) *The ground state is an AF state with spins aligned in the opposite position with all their nearest neighbors to avoid costing extra superexchange energy.* (b)(c) *Two examples of valence bond arrangement at half filling. The RVB ground state is the superposition of all the possible arrangements.*

and revived by Anderson in the resonance valence bond (RVB) theory for cuprates [81]:

$$\begin{aligned}
 \Delta_{ij} &= \langle C_{i\uparrow}C_{j\downarrow} - C_{i\downarrow}C_{j\uparrow} \rangle = \frac{1}{\sqrt{2}}(|\uparrow\downarrow\rangle - |\downarrow\uparrow\rangle) \\
 \chi_{ij} &= \langle C_{i\uparrow}^\dagger C_{j\uparrow} + C_{i\downarrow}^\dagger C_{i\downarrow} \rangle = \frac{1}{\sqrt{2}}(|\uparrow\uparrow\rangle + |\downarrow\downarrow\rangle)
 \end{aligned}
 \tag{2.45}$$

Since charge fluctuations are completely suppressed, these two descriptions (the spin singlet pair and the orbital hybridization) in Equation. 2.45 are equivalent at half filling due to the  $SU(2)$  symmetry [90][55]. The  $SU(2)$  transformation is:

$$\begin{pmatrix} C_{i\uparrow} \\ C_{i\downarrow} \end{pmatrix} = \begin{pmatrix} a & b \\ -b^* & a^* \end{pmatrix} \begin{pmatrix} \tilde{C}_{i\uparrow} \\ \tilde{C}_{i\downarrow} \end{pmatrix}
 \tag{2.46}$$

$$\tag{2.47}$$

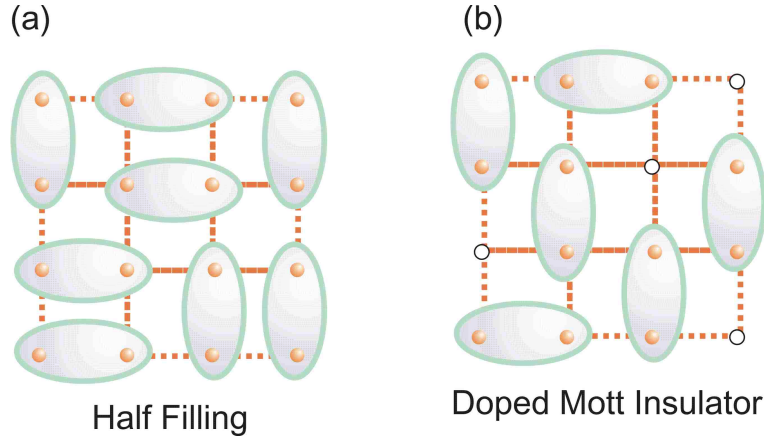


Figure 2.5: *Doping a Mott insulator. (a) One valence bond arrangement at half filling. (b) Doped Mott insulator*

Here the matrix is unitary with  $|a|^2 + |b|^2 = 1$ . If I use  $a = 0, b = 1$ , this will immediately give us the transformation I need to prove the equivalence of the spin singlet pair and the orbital hybridization at half filling in Equation. 2.45:

$$\begin{aligned}
 C_{\uparrow} &\rightarrow C_{\downarrow}^{\dagger} \\
 C_{\downarrow} &\rightarrow -C_{\uparrow}^{\dagger}
 \end{aligned}
 \tag{2.48}$$

If the order parameters are real, the  $s$  state in  $\Delta_{ij}$  is equivalent with the uniform state with real  $\chi_{ij}$ . If the order parameters are complex, the  $s + id$  state in  $\Delta_{ij}$  is equivalent with the flux phase with complex  $\chi_{ij}$ . In Anderson's RVB theory, two nearest neighbor spins form a valence bond to lower the energy. The ground state is a linear superposition of valence bond arrangements (see Figure 2.4). This is considered to be a valence bond liquid state with short range order. Besides valence bond liquid states, there are also symmetry breaking valence bond crystal states that are gapped but competitive in energy [59] [52].

When doping away from half filling, extra carriers break the  $SU(2)$  symmetry. One of the consequences is that the valence bond in the particle-particle representation and particle-hole representation become different from each other. The doping process can be represented in the cartoon Fig. 2.5. This can be viewed as follows: the introduced extra holes hop on the background of the resonating valence bond liquid. As it goes away from half filling, the basic question one can ask is which fluctuation valence bond states is selected when a sufficient amount of doping destroys the AF long-rang order. In the short-range RVB theory, the spin-singlet valence bond pairs are mobilized by the doped holes and tend to condense into a d-wave SC state below  $T_c$  [91]. There is a natural competing order driven by the same spin exchange interaction  $J$ , but associated with the valence bond  $\chi_{ij}$  in particle-hole channel that favors a quantum paramagnetic state. The competition between these two might result in the rich physics of the underdoped cuprates.

### **2.3 The Bridge Between the Theory and Experiment – Using Retarded Green’s Function to Describe One Particle Properties as Seen in Experiments**

Once I have my model, the next step is to determine what "measurables" can be calculated and compared with the experiments. Of particular interest is experimental evidence from ARPES and STM. Together, they described the one-particle properties of cuprates both in the momentum and the real space. One of the important quantities of concern is the retarded Green’s function, since the one particle spectral function and the density of states are both related to it. Following Mahan’s [92] notation, the definition of the

retarded Green's function for an electron in state  $\mathbf{k}$  is:

$$\begin{aligned}
G_{ret}(\mathbf{k}, t - t') &= -i\Theta(t - t')\langle [C_{\mathbf{k}\sigma}(t)C_{\mathbf{k}\sigma}^\dagger(t') + C_{\mathbf{k}\sigma}^\dagger(t')C_{\mathbf{k}\sigma}(t)] \rangle \\
&= -i\Theta(t - t')\langle \{C_{\mathbf{k}\sigma}(t), C_{\mathbf{k}\sigma}^\dagger(t')\} \rangle
\end{aligned}
\tag{2.49}$$

In Equation. 2.49, the expectation value of the quantity in the bracket means taking the thermal average. In other words, it means tracing over a complete set of states. Here I set  $t' = 0$ . It means that one starts a signal at  $t' = 0$  and measures it at a later time  $t$ . The real measurement at time  $t$  is always the result of the signal at starting point  $t' = 0$ . The definition of the retarded Green's function can be simplified into the following form (see Equation. 2.50). This formula is written at a non-zero temperature, but the zero temperature formula can be deduced by setting the temperature to be zero,  $T = 0$ :

$$\begin{aligned}
G_{ret}(\mathbf{k}, t) &= -i\Theta(t)\langle [C_{\mathbf{k}\sigma}(t)C_{\mathbf{k}\sigma}^\dagger(0) + C_{\mathbf{k}\sigma}^\dagger(0)C_{\mathbf{k}\sigma}(t)] \rangle \\
&= -i\Theta(t)\langle \{C_{\mathbf{k}\sigma}(t), C_{\mathbf{k}\sigma}^\dagger(0)\} \rangle \\
&= -i\Theta(t)Tr\{e^{-\beta(K-\Omega)}[\{C_{\mathbf{k}\sigma}(t), C_{\mathbf{k}\sigma}^\dagger(0)\}]\} \\
K &\equiv H - \mu N
\end{aligned}
\tag{2.50}$$

In Equation. 2.50,  $\mu$  is the chemical potential, and  $N$  is the particle number. The thermodynamic potential  $\Omega$  is a scalar function of  $\beta$  and  $\mu$ .  $e^{-\beta\Omega}$  is the usual normalization factor for the thermal average, which can be denoted as  $Z^{-1}$ . The grand Canonical ensemble is used since the particle number of the many body system can vary during the observation. If I write the retarded Green's function out explicitly on a set of states  $|n\rangle$ , and the eigenvalues of

$K$  is  $E_n$ , Equation. 2.50 gives us the following:

$$\begin{aligned}
G_{ret}(\mathbf{k}, t) &= -i\Theta(t)\langle [C_{\mathbf{k}\sigma}(t)C_{\mathbf{k}\sigma}^\dagger(0) + C_{\mathbf{k}\sigma}^\dagger(0)C_{\mathbf{k}\sigma}(t)] \rangle \\
&= -i\Theta(t)e^{\beta\Omega} \sum_n \langle n|C_{\mathbf{k}\sigma}(t)C_{\mathbf{k}\sigma}^\dagger(0) + C_{\mathbf{k}\sigma}^\dagger(0)C_{\mathbf{k}\sigma}(t)|n \rangle \\
&= -i\Theta(t)e^{\beta\Omega} \sum_{m,n} \langle n|C_{\mathbf{k}\sigma}(t)|m \rangle \langle m|C_{\mathbf{k}\sigma}^\dagger(0)|n \rangle + \langle n|C_{\mathbf{k}\sigma}^\dagger(0)|m \rangle \langle m|C_{\mathbf{k}\sigma}(t)|n \rangle \\
&= -i\Theta(t)e^{\beta\Omega} \sum_{m,n} |\langle n|C_{\mathbf{k}\sigma}|m \rangle|^2 e^{it(E_n - E_m)} [e^{-\beta E_n} + e^{-\beta E_m}]
\end{aligned} \tag{2.51}$$

The retarded Green's function has the standard Fourier transform:

$$\begin{aligned}
G_{ret}(\mathbf{k}, \omega) &= \int G_{ret}(\mathbf{k}, t) \exp(i\omega t) \\
G_{ret}(\mathbf{k}, t) &= \frac{1}{2\pi} \int G_{ret}(\mathbf{k}, \omega) \exp(-i\omega t)
\end{aligned} \tag{2.52}$$

Utilizing the Fourier transform in Equation. 2.52 to transform the retarded Green's function from the time  $t$  space to energy  $\omega$  space, I get the frequency dependent retarded Green's function:

$$\begin{aligned}
G_{ret}(\mathbf{k}, \omega) &= -i \int_0^\infty e^{it(\omega+i\delta)} dt e^{\beta\Omega} \sum_{m,n} |\langle n|C_{\mathbf{k}\sigma}|m \rangle|^2 e^{it(E_n - E_m)} [e^{-\beta E_n} + e^{-\beta E_m}] \\
&= e^{\beta\Omega} \sum_{m,n} |\langle n|C_{\mathbf{k}\sigma}|m \rangle|^2 \frac{e^{-\beta E_n} + e^{-\beta E_m}}{\omega + E_n - E_m + i\delta}
\end{aligned} \tag{2.53}$$

In the experiment,  $\omega$  is the energy relevant to the Fermi level. Since the reference metal and the superconductor are in the thermal equilibrium, they have the same Fermi Level. In equation. 2.53,  $\delta \rightarrow 0^+$ . Sokhotsky's formula comes in handy when taking the limit. The Sokhotsky's formula states that:

$$\lim_{\epsilon \rightarrow 0^+} \frac{1}{x \pm i\epsilon} = P\left(\frac{1}{x}\right) \mp i\pi\delta(x) \quad (2.54)$$

After taking the limit, the retarded Green's function becomes:

$$\begin{aligned} G_{ret}(\mathbf{k}, \omega) &= e^{\beta\Omega} \sum_{m,n} |\langle n|C_{\mathbf{k}\sigma}|m\rangle|^2 \frac{e^{-\beta E_n} + e^{-\beta E_m}}{\omega + E_n - E_m + i\delta} \\ &= e^{\beta\Omega} \sum_{m,n} |\langle n|C_{\mathbf{k}\sigma}|m\rangle|^2 [e^{-\beta E_n} + e^{-\beta E_m}] \\ &\quad [P(\omega + E_n - E_m) - i\pi\delta(\omega + E_n - E_m)] \end{aligned} \quad (2.55)$$

The definition of the one particle spectral function is :

$$A(\mathbf{k}, \omega) = -2Im[G_{ret}(\mathbf{k}, \omega)] \quad (2.56)$$

Then I get the spectral function for the electron:

$$A(\mathbf{k}, \omega) = 2\pi e^{\beta\Omega} \sum_{m,n} |\langle n|C_{\mathbf{k}\sigma}|m\rangle|^2 [e^{-\beta E_n} + e^{-\beta E_m}] \delta(\omega + E_n - E_m) \quad (2.57)$$

A standard manipulation of the temperature factors can be utilized:

$$[e^{-\beta E_n} + e^{-\beta E_m}] = e^{-\beta E_m} [1 + e^{-\beta(E_n - E_m)}] \quad (2.58)$$

$f(\omega)$  is the Fermi function:

$$f(\omega) = \frac{1}{e^{-\frac{\omega}{k_B T}} + 1} \quad (2.59)$$

The spectral function can be written as:

$$A(\mathbf{k}, \omega) = 2\pi e^{\beta\Omega} \sum_{m,n} |[e^{-\beta E_m}/f(\omega)]\langle n|C_p|m\rangle|^2 \delta(\omega + E_n - E_m) \quad (2.60)$$

ARPES is measuring the photoemission process which extracts one electron from the system. The spectral function  $A(\mathbf{k}, \omega)$  contains two parts: the photoemission term and the inverse photoemission term.  $A^-(\mathbf{k}, \omega)$  is the one electron removal spectra, which can be extracted from the ARPES measurement.  $A^+(\mathbf{k}, \omega)$  is the one electron addition spectra which can be extracted from inverse photoemission. High quality data is currently lacking though from inverse photoemission experiments. The relation in between these spectral functions is:

$$A(\mathbf{k}, \omega) = A^-(\mathbf{k}, \omega) + A^+(\mathbf{k}, \omega) \quad (2.61)$$

The one electron removal spectral function can be written as:

$$A^-(\mathbf{k}, \omega) = 2\pi e^{\beta\Omega} \sum_{m,n} |[e^{-\beta E_m}]\langle n|C_p|m\rangle|^2 \delta(\omega + E_n - E_m) \quad (2.62)$$

As a result:

$$A^-(\mathbf{k}, \omega) = f(\omega)A(\mathbf{k}, \omega) \quad (2.63)$$

In order to write the intensity measured by an ARPES experiment explicitly, several approximations need to be made. One of them is the sudden approximation. Assume the energy of the photo-electron is high, the outgoing photo-electron is so fast that I can ignore its interaction with other photo-holes and the medium. The process of the photoemission can be treated

simply by considering that this photo-electron is removed from the system instantaneously, the rest of the system changes its status into a new state of matter instantaneously. Once the process happens, both the photo-electron and the remaining system do not suffer any continuous change due to collisions. Although this does not apply to photo-electrons which have low energy, at least providing the context wherein, this is a valid approximation [93]. Another approximation is that I need to neglect any extrinsic background to simplify the real situation into a simple formula. The energy distribution curve(EDC) is given by [94][95]:

$$I(\mathbf{k}, \omega) = I_0(\mathbf{k})f(\omega)A(\mathbf{k}, \omega) \quad (2.64)$$

$\mathbf{k}$  is the momentum on the  $2D$  plane of the sample.  $I_0(\mathbf{k})$  is related to the square of the one electron dipole matrix element and all the kinematical factors. Symmetrization of the spectrum is the usual technique for ARPES in order to take out the effect of Fermi function at finite temperature. In this way the true gap can be measured.

The integrated density of states can be calculated by summing over all the  $\mathbf{k}$  space points.

$$\sum_{\mathbf{k}} A(\mathbf{k}, \omega) = N(\omega) \quad (2.65)$$

Following the same routine, I can calculate the local tunneling density of states to compare with STM data [96]. For example at  $T = 0$  K, I can define the retarded Green's function of an electron in real space:

$$G_{ret}(i, t) = -\theta(t)\langle\{C_{i\sigma}(0)^\dagger, C_{i\sigma}(t)\}\rangle \quad (2.66)$$

The local density of states can be calculated with the definition of the spectral function and the sum rule:

$$N_i(\omega) = Im \int dt e^{i\omega t} G_{ret}(i, t) \quad (2.67)$$

Equipped with these tools, not only I can study the two valence bond channels arising from the superexchange interactions on the level of mean field order parameters, but also I can compare the consequences of the interplay between these two by looking at the one particle properties. Thus, I can thoroughly investigate the matter of pseudogap in cuprates.

# Chapter 3

## The Incommensurate Bond Density Wave State of Cuprates

### 3.1 The Visualization of Bond Density Waves in Cuprates

On the  $CuO_2$  plane there are two hypothetical ways for the density wave to form: the  $O - Cu - O$  site centered density wave and the  $Cu - O - Cu$  bond centered density wave. With increasing spatial resolution of STM measurements, Davis et al. [29] have successfully resolved the difference between these two. They have studied two lightly hole-doped cuprates:  $Ca_{1.88}Na_{0.12}CuO_2Cl_2$  and  $Bi_2Sr_2Dy_{0.2}Ca_{0.8}Cu_2O_{8+d}$  with the atomic-resolution tunneling-asymmetry imaging method. Despite the difference of the two, the universality in terms of spatial variations at the planar oxygen sites is obvious in both materials. Their spatial arrangement forms a  $Cu - O - Cu$  bond-centered electronic pattern without long-range order. The natural bond centered quantity in mean field  $t - J$  model is the paramagnetic valence bond  $\chi_{ij}$ . This observation is motivation to study the bond channel in detail.

One important observation in Fig. 3.1(c) is that the major spatial vari-

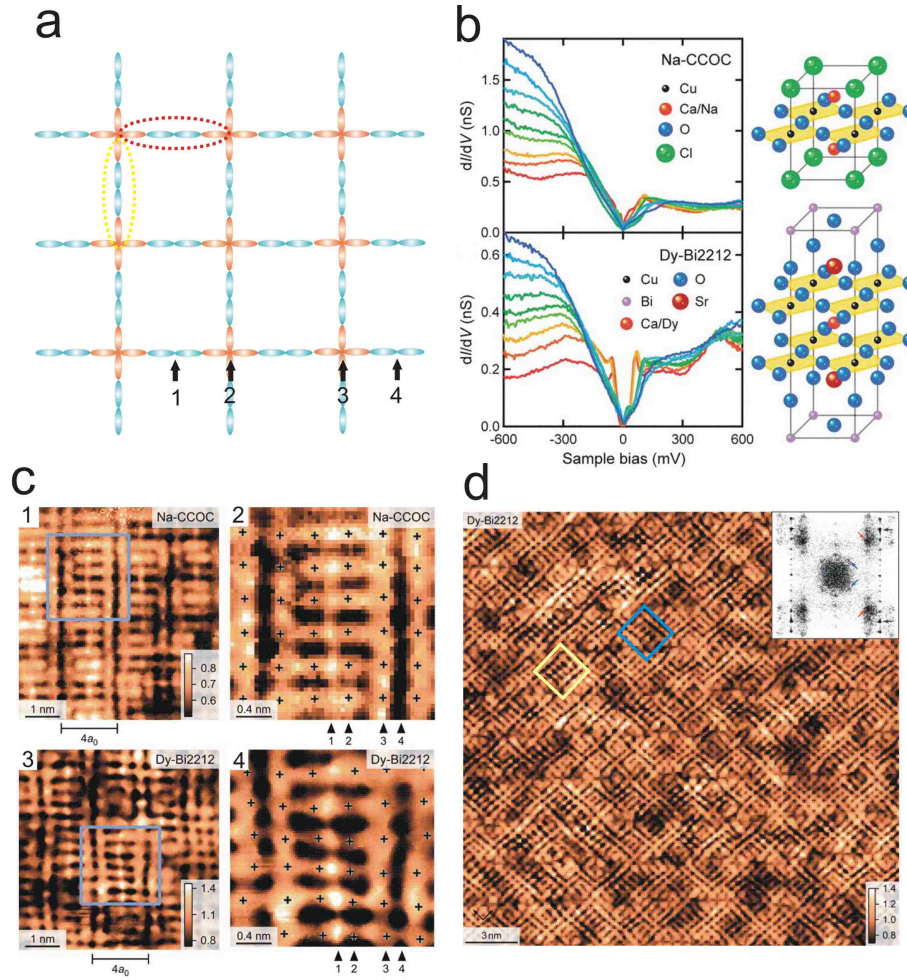


Figure 3.1: (a) electronic orbitals of the  $\text{CuO}_2$  plane. Cu 3d orbitals are shown in orange and O 2p orbitals are shown in blue. Two structural equivalent Cu – O – Cu bonds are shown in the dashed ovals, along the x-direction is shown in red, along the y-direction is shown in yellow. (b) Typical  $dI/dV$  curves at 4.2K of Na – CCOC ( $T_c \sim 21\text{K}$ ) and Dy – Bi2212 ( $T_c \sim 45\text{K}$ ) are shown on the left. The spectra is normalized on the positive side. The structure of Na – CCOC and Dy – Bi2212 are shown on the right. (c) R map of Na – CCOC (c1) and Dy – Bi2212 (c3), where  $R(\mathbf{r}, V) = \frac{I(\mathbf{r}, z, +V)}{I(\mathbf{r}, z, -V)}$ . The corresponding high resolution R map within equivalent domains in the blue boxes are shown in (c2) and (c4) respectively. The location of the Cu atoms are shown as black crosses. (d) A field of view R map of Dy – Bi2212, the blue box and yellow box show two typical domains of Cu – O – Cu bond states with different bond orientations. They are randomly distributed with equal probability. Graphs are modified from [29]

ation is concentrated on the O site rather than Cu site, which is in strong support of bond centered behavior. The intensity is very different between the oxygen site along the vertical line labeled '1' and the oxygen site along the vertical line labeled '4'. Also, although sharing the same corner  $Cu$ , the intensity on the x-direction oxygen site and the intensity on the y-direction oxygen site are very different. Both the rotational  $C4$  symmetry and translational symmetry are broken from a perfect square lattice. With the help of a field of view map in Fig. 3.1 (d), I can identify two kinds of domains with perpendicular electronic variations of the  $Cu - O - Cu$  bond states. They are randomly distributed in the entire sample with equal probability. These observations are highly suggestive that there are two energetically degenerate states which have different bond orientations and serve as a major inspiration of bond centered treatment of normal state Hamiltonian.

## 3.2 Incommensurate Multiple Scattering in Underdoped Cuprates

Away from half filling, when there is enough doping, the paramagnetic bond channel and the pairing channel become different. In this chapter, I focus on the normal state by turning off the pairing channel completely. Also, I focus on the state without breaking the time reversal symmetry so the order parameter in the bond channel is real. My starting point is choosing a unreconstructed Fermi surface in the Fermi liquid state described by:

$$\hat{H}_0 = \sum_{\mathbf{k}, \sigma} (\varepsilon(\mathbf{k}) - \mu_f) (C_{\mathbf{k}\sigma}^\dagger C_{\mathbf{k}\sigma}) \quad (3.1)$$

Where  $C_k^\dagger (C_k)$  is the creation (annihilation) operator for an electron with momentum  $\mathbf{k}$ ,  $\hat{H}_0$  is a renormalized tight binding model and  $\varepsilon(\mathbf{k})$  is the renormalized band dispersion with the Gutzwiller factor.  $\mu_f$  is introduced to keep track of the doping. This will give a large Fermi surface in the uniform case. It is a continuous contour in momentum space centered at  $(\pi, \pi)$ . The volume of this hole like contour is proportional to the hole density following Luttinger's theorem [97]. This is confirmed by ARPES in the optimal to overdoped regime. I use  $J = 120meV$  and up to the fifth nearest neighbor hoppings  $t = (360; -120; 29; 24; -24)meV$  relevant for the band structure [98] to calculate the shape of the Fermi surface at different dopings. The result is shown in Fig. 3.2. With the increase of doping, the volume of Fermi surface increases.

STM reported the intrinsic bond centered short ranged order with a wavevector  $q$  [29]. And also the truncation of the the sections of the large Fermi surface around  $(\pi, 0)$  and  $(0, \pi)$  are generally believed to be tied to the scattering around the antinodal region by certain wave vector  $q$ , as observed in the ARPES measurements. As a result, in addition to the Hamiltonian Eq. 3.1, I need to add a term which includes the multiple scattering process.

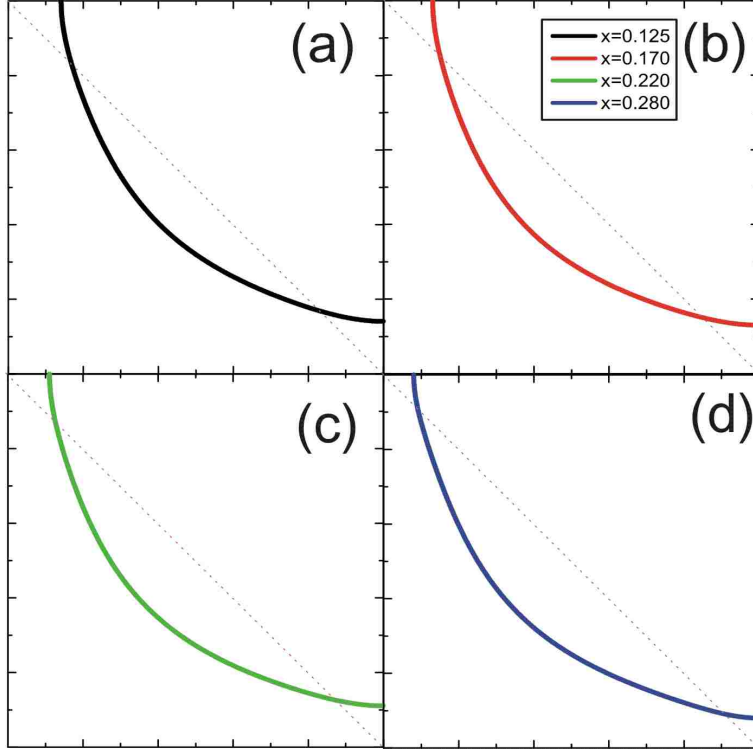


Figure 3.2: *Continuous Fermi surface line shape in the normal Fermi liquid state, at the doping level (a) $x=0.125$ , (b) $x=0.17$ , (c) $x=0.22$ , (d) $x=0.28$*

I call this term  $\hat{H}_s$ , standing for the scattering part of the Hamiltonian.

$$\hat{H}_s = \sum_{kq} V_q (C_{k+q}^\dagger C_k + h.c.) \quad (3.2)$$

So the total Hamiltonian can be written as :

$$\hat{H} = \hat{H}_0 + \hat{H}_s \quad (3.3)$$

The specific form of  $\hat{H}$  in the context of the t-J model will be discussed in detail in section 3.3. I illustrate here the basic ideas. In Equation. 3.3,  $H_0$  is the diagonal part in  $k$ , and  $H_s$  is the off diagonal part which connects different  $k$ 's by  $q$ .  $H_s$  is part of the Hamiltonian which cannot be considered small.

In other words, without considering the entangled part  $H_s$ , the system has a well defined set of eigenstates with eigenvalues  $E_k$  with a large normal state Fermi surface. But with multiple scattering, the situation becomes more complicated. I allow all possible  $q$ 's connecting all  $k$ 's to lower the total energy of the system. In this way, I take into account every scattering which can happen in the system. To understand how to treat the  $H_s$  term, I need to explain the effect of multiple scattering with incommensurate wavevector  $q$ .

First I need to define what I mean by "incommensuration". Consider the simplest 1D example: when  $q$  is commensurate where  $q = q_{AF} = \pi$ , as shown in Fig. 3.3(a). The top panel shows that  $k$  and  $k + q$  are connected by  $q$ . Due to the periodicity in momentum space,  $k$  and  $k + 2q$  are equivalent. In order to show this equivalence, the bottom panel connects  $k$  and  $k + 2q$  as one point to make a full circle. This problem can be solved by diagonalizing the matrix.

$$\mathbb{A}_{AF} = \begin{pmatrix} \varepsilon_k & V_q \\ V_q & \varepsilon_{k+q} \end{pmatrix} \quad (3.4)$$

When  $q$  is incommensurate,  $q$  is not a rational number. The multiple scattering connected by incommensurate wavevectors never closes a full loop, as shown in Fig. 3.3(b). Each scattering is unique in  $k$  space and will never repeat. This means that no periodicity can be found. If I start with a point  $k$  in momentum space, there are an infinite number of other  $k'$  points connected by a series of scatterings related to the incommensurate vector  $q$ . Because of this, writing down the matrix or diagonalizing it is impossible.

Due to this infinite point problem I have no choice but to reduce the dimension of  $k$ . To compromise I write the incommensurate wavevector into an almost incommensurate case. Eq. 3.5 shows an almost incommensurate

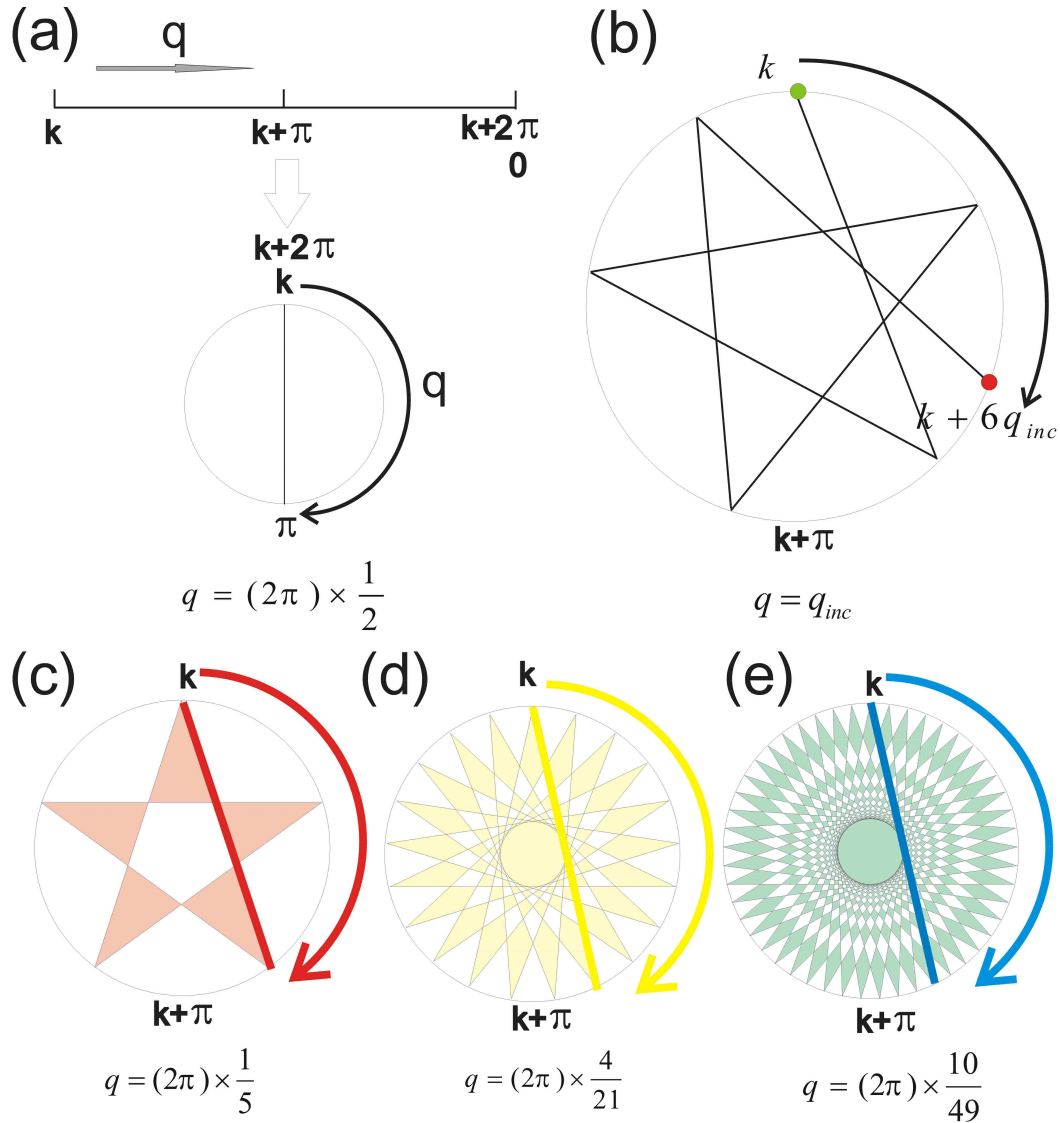


Figure 3.3: *Cartoon illustration of commensuration, incommensuration and practical "almost" incommensuration in 1D (a)  $q_{AF} = \pi$ , the simplest commensurate case. The bottom panel is the rolled up top panel due to the periodicity in momentum space. (b)  $q = q_{inc}$  incommensuration case, starting point  $k$  and end point  $k' = k + nq_{inc}$  where  $n$  is a positive integer (in the graph,  $n=6$ ), are both distinctive points in momentum space, it can never form a closed loop since  $q_{inc}$  is not a rational number. (c)(d)(e) demonstration of mimicking the incommensuration by increasing the denominator  $M$  in  $q = N/M(2\pi)$ , note that  $N/M = 1/5 \approx 4/21 \approx 10/49$*

case (when  $M$  is a large enough number). I approximate incommensuration by a large commensurate ratio.

$$Q = n \times q, n = (0, 1, 2, \dots, M - 1) \quad (3.5)$$

$$q = \frac{N}{M} \times (2\pi) \quad (3.6)$$

$$(3.7)$$

where  $N$  and  $M$  are positive integers. Fig. 3.3 (c)(d)(e) show the transition from the commensurate scattering to the incommensurate scattering by increasing the denominator  $M$  in Eq. 3.5. In Fig. 3.3(c)  $q = (N/M)2\pi = (1/5)2\pi$  is the base scattering vector, this is a commensurate case since the denominator  $M$  is very small. It forms a closed loop by  $5q$ . This problem can be solved by diagonalizing the matrix in Eq. 3.8:

$$\mathbb{A} = \begin{pmatrix} \varepsilon_k - \mu & f(V_q, V_{4q}) & f(V_{2q}, V_{3q}) & f(V_{2q}, V_{3q}) & f(V_q, V_{4q}) \\ f(V_q, V_{4q}) & \varepsilon_{k+q} - \mu & f(V_q, V_{4q},) & f(V_{2q}, V_{3q},) & f(V_{2q}, V_{3q}) \\ f(V_{2q}, V_{3q}) & f(V_q, V_{4q}) & \varepsilon_{k+2q} - \mu & f(V_{4q}, V_q) & f(V_{2q}, V_{3q}) \\ f(V_{2q}, V_{3q}) & f(V_{2q}, V_{3q}) & f(V_q, V_{4q}) & \varepsilon_{k+3q} - \mu & f(V_q, V_{4q}) \\ f(V_q, V_{4q}) & f(V_{2q}, V_{3q}) & f(V_{2q}, V_{3q}) & f(V_q, V_{4q}) & \varepsilon_{k+4q} - \mu \end{pmatrix} \quad (3.8)$$

It is worth noting that here in Eq. 3.8, all of the  $V_{nq}$  are order parameters. They all serve an equally important role at the beginning of the iterations. They become different in strength after being solved self consistently. For the incommensurate case, the system undergoes a multiple scattering process with continuous scattering wave vectors. The incommensurate limit is when  $k$  space and  $q$  space are both continuous. As a result, through multiple scattering, all the preferred scattering according to the topology of the Fermi surface can be picked up. Equivalently, all the scattering process with different wave vectors will be chosen by the system itself, and an ensemble of the prominent scattering will be dominating in the ground state. It is natural to

reach the conclusion that all the possible scattering processes involving different wave vectors need to be considered as independent order parameters and that the total energy should be minimized with respect to everyone of them.

Looking back to the realization of almost incommensuration, in Fig. 3.3(c)(d)(e) the denominator  $M$  increases from (c) to (e). There are more and more  $k$  points connected as  $M$  increases the denominator. It is useful for me to choose a large enough  $M$  without paying the expensive computing time to study the almost incommensurate case as an approximation to the incommensurate limit. Here I am going to drop the terminology "almost", and call a wavevector "incommensurate" when the denominator  $M$  is large enough. This carries out through the rest of this chapter.

### 3.3 Renormalized Mean Field Hamiltonian in Momentum Space

After outlining how to treat the incommensurate wave vector, the problem now boils down to how to treat the bond centered hopping term. My starting point is the normal state renormalized mean field Hamiltonian in real space as described in Eq. 2.44. Setting pairing to be zero it reads:

$$\begin{aligned}
H_{\text{GA}} = & - \sum_{i \neq j} g_{ij}^t t_{ij} c_{i\sigma}^\dagger c_{j\sigma} \\
& - \frac{1}{4} J \sum_{\langle i,j \rangle} g_{ij}^\chi \left( \chi_{ij}^* c_{i\sigma}^\dagger c_{j\sigma} + \text{h.c.} - |\chi_{ij}|^2 \right) \\
& - \mu_f \sum c_{i\sigma}^\dagger c_{i\sigma}
\end{aligned} \tag{3.9}$$

Where  $\chi_{ij} = \sum_{\sigma} C_{i\sigma}^\dagger C_{j\sigma}$  is the bond order parameter of concern. The density at every site is  $n_i = 1 - x_i$ . Since I am going to study the system in  $k$  space, I use the uniform Gutzwiller approximation in Eq. 2.29, where  $g_{ij}^t = g^t = \frac{2x}{1+x}$  and  $g_{ij}^\chi = \frac{4}{(1+x)^2}$ . The hopping term contains up to fifth nearest neighbor hopping. The Fourier transform is given by:

$$\begin{aligned}
- \sum_{n=1} \sum_{ij\sigma} t_n \cdot g^t C_{i\sigma}^\dagger C_{j\sigma} &= - \sum_{n=1} \sum_k g^t \cdot t_n \beta_n \left( C_{k\uparrow}^\dagger C_{k\uparrow} + C_{k\downarrow}^\dagger C_{k\downarrow} \right) \tag{3.10} \\
\beta_1 &= 2 * (\cos k_x + \cos k_y) \\
\beta_2 &= 4 * (\cos k_x \cdot \cos k_y) \\
\beta_3 &= 2 * (\cos 2k_x + \cos 2k_y) \\
\beta_4 &= 4 * (\cos 2k_x \cdot \cos k_y + \cos k_x \cdot \cos 2k_y) \\
\beta_5 &= 4 * (\cos 2k_x \cdot \cos 2k_y)
\end{aligned} \tag{3.11}$$

Now I need to choose the coordinates to Fourier transform the term involving  $\chi_{ij} = \sum_{\sigma} C_{i\sigma}^\dagger C_{j\sigma}$ . Examining the  $\text{CuO}_2$  plane closely it can be seen that for each copper site there are two bonds that share the same copper

without double counting. As a result, there are two equivalent sets of bonds, the x direction bond and y direction bond, as shown in Fig. 3.4. The choice of bond center is quite non-trivial. Here, I adopt the idea of bond centered short ranged order. I choose the location of the x direction bond and the y direction bond as in Fig. 3.4, labeled by  $\mathbf{R}_x(i)$  and  $\mathbf{R}_y(i)$  respectively. They are half a lattice constant offset from the copper atom site labeled by  $\mathbf{r}(i)$ . The relationship is in shown in Fig. 3.12:

$$\begin{aligned}\mathbf{R}_x(i) &= \mathbf{r}(i) + \hat{\mathbf{x}}/2 \\ \mathbf{R}_y(i) &= \mathbf{r}(i) + \hat{\mathbf{y}}/2\end{aligned}\tag{3.12}$$

A Fourier transform of the  $\chi$  term can be written in terms of the x bond and y bond:

$$\begin{aligned}\chi_x(i) &= \sum_q \chi_x(q) \cos(\mathbf{q} \cdot \mathbf{R}_x(i)) \\ &= \sum_q \chi_x(q) \cos(\mathbf{q} \cdot \mathbf{r}_i + \frac{1}{2}\mathbf{q} \cdot \hat{\mathbf{x}}) \\ \chi_y(i) &= \sum_q \chi_y(q) \cos(\mathbf{q} \cdot \mathbf{R}_y(i)) \\ &= \sum_q \chi_y(q) \cos(\mathbf{q} \cdot \mathbf{r}_i + \frac{1}{2}\mathbf{q} \cdot \hat{\mathbf{y}})\end{aligned}\tag{3.13}$$

With this definition of bond centered two sublattice sites for  $\chi_{ij}$ , I perform the Fourier transform in the bond channel of the Hamiltonian. Note that the fermions follow the site centered definition. If I only consider the real part of the bond, it reads,

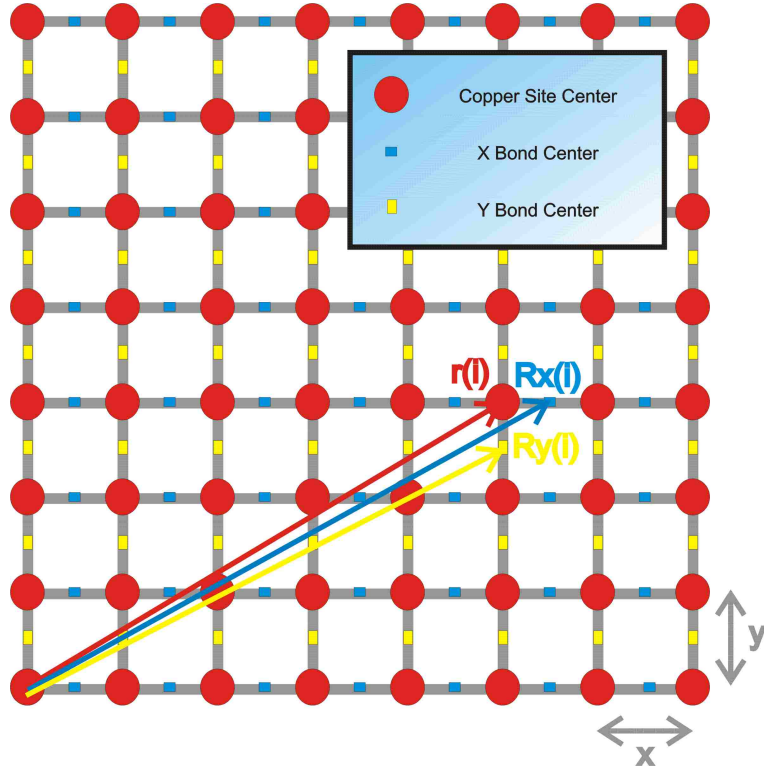


Figure 3.4: The illustration of  $\text{CuO}_2$  Plane. The red circle is the copper site, labeled by  $\mathbf{r}(i)$  at site  $i$ . The blue and yellow rectangular are bond centered oxygen sites, labeled by  $\mathbf{r}_x(i)$  and  $\mathbf{r}_y(i)$  respectively. Different colors denote the different orientations of the bonds.

$$\begin{aligned}
& \sum_{\langle i,j \rangle \sigma} \chi_{i,j}^* C_{i\sigma}^\dagger C_{j\sigma} \\
&= \sum_{i\eta} \sum_{kk'q} \chi_\eta(q) \frac{1}{2} [e^{i(\mathbf{q}\cdot\mathbf{r}_i + \frac{1}{2}\mathbf{q}\cdot\hat{\eta})} + e^{-i(\mathbf{q}\cdot\mathbf{r}_i + \frac{1}{2}\mathbf{q}\cdot\hat{\eta})}] e^{i\mathbf{k}\cdot\mathbf{r}_i} e^{-ik'\cdot(\mathbf{r}_i + \hat{\eta})} C_k^\dagger C_{k'} \\
&= \frac{1}{2} \sum_{\eta kq} e^{-i(\mathbf{k} + \frac{1}{2}\mathbf{q})\cdot\hat{\eta}} \chi_\eta(q) (C_k^\dagger C_{k+q} + C_{k+q}^\dagger C_k) \tag{3.14}
\end{aligned}$$

In the same way I can do the Fourier transform on the *h.c.* term of the

bond channel.

$$\begin{aligned}
& \sum_{\langle i,j \rangle \sigma} \chi_{i,j} C_{j\sigma}^\dagger C_{i\sigma} \\
&= \sum_{i\eta} \sum_{kk'q} \chi_\eta(q) \frac{1}{2} [e^{i(\mathbf{q}\cdot\mathbf{r}_i + \frac{1}{2}\mathbf{q}\cdot\hat{\eta})} + e^{-i(\mathbf{q}\cdot\mathbf{r}_i + \frac{1}{2}\mathbf{q}\cdot\hat{\eta})}] e^{i\mathbf{k}\cdot(\mathbf{r}_i + \hat{\eta})} e^{-ik'\cdot\mathbf{r}_i} C_k^\dagger C_{k'} \\
&= \frac{1}{2} \sum_{\eta kq} e^{i(\mathbf{k} + \frac{1}{2}\mathbf{q})\cdot\hat{\eta}} \chi_\eta(q) (C_k^\dagger C_{k+q} + C_{k+q}^\dagger C_k) \tag{3.15}
\end{aligned}$$

Summing them up, I get the Fourier transform of the second part of the Hamiltonian:

$$\begin{aligned}
& \sum_{\langle i,j \rangle \sigma} \chi_{i,j}^* C_{i\sigma}^\dagger C_{j\sigma} + h.c. \\
&= \sum_{\eta} \sum_{kq} \cos((\mathbf{k} + \frac{1}{2}\mathbf{q}) \cdot \hat{\eta}) \chi_\eta(q) (C_k^\dagger C_{k+q} + C_{k+q}^\dagger C_k) \tag{3.16}
\end{aligned}$$

And the mean field constant term reads:

$$\begin{aligned}
\sum_{ij} |\chi_{ij}|^2 &= \sum_{i\eta} \chi_{i\eta}^* \chi_{i\eta} \\
&= \sum_{iqq'\eta} \chi_\eta(q) \chi_\eta(q') \cos(\mathbf{q} \cdot \mathbf{r}_i + \frac{1}{2} \mathbf{q} \cdot \hat{\eta}) \cos(\mathbf{q}' \cdot \mathbf{r}_i + \frac{1}{2} \mathbf{q}' \cdot \hat{\eta}) \\
&= \frac{1}{4} N \sum_{qq'\eta} \chi_\eta(q) \chi_\eta(q') [\delta(\mathbf{q} + \mathbf{q}' + \mathbf{G}) e^{i\frac{\mathbf{q} + \mathbf{q}'}{2}}] \\
&\quad + \frac{1}{4} N \sum_{qq'\eta} \chi_\eta(q) \chi_\eta(q') [\delta(\mathbf{q} - \mathbf{q}' + \mathbf{G}) e^{i\frac{\mathbf{q} - \mathbf{q}'}{2}}] \\
&\quad + \frac{1}{4} N \sum_{qq'\eta} \chi_\eta(q) \chi_\eta(q') [\delta(-\mathbf{q} + \mathbf{q}' + \mathbf{G}) e^{i\frac{-\mathbf{q} + \mathbf{q}'}{2}}] \\
&\quad + \frac{1}{4} N \sum_{qq'\eta} \chi_\eta(q) \chi_\eta(q') [\delta(-\mathbf{q} - \mathbf{q}' + \mathbf{G}) e^{i\frac{-\mathbf{q} - \mathbf{q}'}{2}}] \\
&= N \sum_q (|\chi_x(q)|^2 + |\chi_y(q)|^2) \tag{3.17}
\end{aligned}$$

The t-J model in k space with bond centered  $\chi_{ij}$  reads:

$$\begin{aligned}
\mathbf{H} &= - \sum_{k,\sigma} \left[ \sum_{n=1}^5 g^n \beta_n t_n - \mu_f \right] C_{k,\sigma}^\dagger C_{k,\sigma} \\
&\quad - \sum_{kq\sigma} \frac{1}{4} J g^J \left( \cos(k_x + \frac{1}{2} q_x) \chi_x(\mathbf{q}) + \cos(k_y + \frac{1}{2} q_y) \chi_y(\mathbf{q}) \right) (C_k^\dagger C_{k+q} + h.c.) \\
&\quad + N \sum_q \frac{1}{4} J g^J (|\chi_x(\mathbf{q})|^2 + |\chi_y(\mathbf{q})|^2) \tag{3.18}
\end{aligned}$$

Separating into two parts, the diagonal part and the off diagonal parts

(as before), I get:

$$\begin{aligned}
\hat{H} &= \hat{H}_0 + \hat{H}_s \\
\hat{H}_0 &= - \sum_{k,\sigma} \left[ \sum_{n=1}^5 g^t t_n \beta_n + \frac{1}{2} J g^J (\cos(k_x) + \cos(k_y)) \chi_0 - \mu_f \right] C_{k,\sigma}^\dagger C_{k,\sigma} \\
&= \sum_{\mathbf{k},\sigma} (\varepsilon(\mathbf{k}) - \mu_f) (C_{\mathbf{k}\sigma}^\dagger C_{\mathbf{k}\sigma}) \\
H_s &= - \sum_{kq\sigma} \frac{1}{4} J g^J \left( \cos(k_x + \frac{1}{2}q_x) \chi_x(\mathbf{q}) + \cos(k_y + \frac{1}{2}q_y) \chi_y(\mathbf{q}) \right) (C_k^\dagger C_{k+q} + h.c.) \\
&+ N \sum_q \frac{1}{4} J g^J (|\chi_x(\mathbf{q})|^2 + |\chi_y(\mathbf{q})|^2)
\end{aligned} \tag{3.19}$$

Since I am modeling a 2D plane I need to extend my treatment of the incommensurate  $\mathbf{q}$  in the last section into two dimensions. I am considering all the possible  $\mathbf{q}$  in a 2D momentum space, and they contribute equally to the Hamiltonian  $H_s$ . The spontaneous breaking of the lattice symmetry by  $\mathbf{q}$  will be determined self-consistently. If  $\mathbf{q}$  is the connecting vector, state  $\mathbf{k}$  is connected with  $\mathbf{k} + \mathbf{q}$  through vector  $\mathbf{q}$ , where

$$\begin{aligned}
\mathbf{q} &\equiv (q_x, q_y) = (n_x q, n_y q) \\
n_{x,y} &= 0, 1, \dots, M - 1 \\
q &= 2\pi \left( \frac{N}{M} \right) \\
M &> N > 0
\end{aligned} \tag{3.20}$$

I minimize the ground state energy of Eq. 3.18 through self-consistently determined  $\chi_x(\mathbf{q}), \chi_y(\mathbf{q})$  for every  $\mathbf{q}$  in the 2D plane of dimension  $M^2 \times M^2$  lattice sites for different choice of M.

The stationary states are determined by

$$\begin{aligned}
\left\langle \frac{\partial H_k}{\partial \chi_x(\mathbf{q})} \right\rangle &= 0 \\
\left\langle \frac{\partial H_k}{\partial \chi_y(\mathbf{q})} \right\rangle &= 0
\end{aligned}
\tag{3.21}$$

As a result, I get the self-consistency equations for  $\chi_x(\mathbf{q}), \chi_y(\mathbf{q})$

$$\begin{aligned}
\chi_x(\mathbf{q}) &= \frac{1}{2N} \sum_{k\sigma} \cos(k_x + \frac{1}{2}q_x) \langle C_{k,\sigma}^\dagger C_{k+q,\sigma} + h.c. \rangle \\
\chi_y(\mathbf{q}) &= \frac{1}{2N} \sum_{k\sigma} \cos(k_y + \frac{1}{2}q_y) \langle C_{k,\sigma}^\dagger C_{k+q,\sigma} + h.c. \rangle
\end{aligned}
\tag{3.22}$$

I choose a 2D momentum space  $\mathbf{k} = (k_x, k_y)$ .

$$\mathbf{C}_{\mathbf{k}}^\dagger = (C_{\mathbf{k}}^\dagger, C_{\mathbf{k}+(0,q)}^\dagger, \dots, C_{\mathbf{k}+(M-1)q, (M-1)q}^\dagger)
\tag{3.23}$$

At this point I can write my Hamiltonian into the matrix form, It reads:

$$\begin{aligned}
H &= H_0 + H_s \\
&= \sum_{\mathbf{k}\sigma} \mathbf{C}_{\mathbf{k}\sigma}^\dagger \mathbb{A}_0 \mathbf{C}_{\mathbf{k}\sigma} \\
&\quad + \sum_{\mathbf{k}\mathbf{q}\sigma} \mathbf{C}_{\mathbf{k}\sigma}^\dagger \mathbb{A}_{\mathbf{k}\mathbf{q}} \mathbf{C}_{\mathbf{k}+\mathbf{q},\sigma}
\end{aligned}
\tag{3.24}$$

where

$$\mathbb{A}_0 = \begin{pmatrix} A_{\mathbf{k},\mathbf{k}} & 0 & \cdots & 0 \\ 0 & A_{\mathbf{k}+(0,q),\mathbf{k}+(0,q)} & \cdots & 0 \\ \cdots & \cdots & \cdots & \\ 0 & 0 & \cdots & A_{\mathbf{k}+((M-1)q,(M-1)q),\mathbf{k}+((M-1)q,(M-1)q)} \end{pmatrix} \quad (3.25)$$

$$\mathbb{A}_{\mathbf{k}\mathbf{q}} = \begin{pmatrix} 0 & A_{\mathbf{k},\mathbf{k}+(0,q)} & \cdots & A_{\mathbf{k},\mathbf{k}+((M-1)q,(M-1)q)} \\ A_{\mathbf{k},\mathbf{k}+(0,q)} & 0 & \cdots & A_{\mathbf{k}+(0,q),\mathbf{k}+((M-1)q,(M-1)q)} \\ \cdots & \cdots & \cdots & \\ A_{\mathbf{k},\mathbf{k}+((M-1)q,(M-1)q)} & A_{\mathbf{k}+(0,q),\mathbf{k}+((M-1)q,(M-1)q)} & \cdots & 0 \end{pmatrix} \quad (3.26)$$

in which, the element  $A_{\mathbf{k},\mathbf{k}+\mathbf{q}}$  and  $A_{\mathbf{k},\mathbf{k}}$  read:

$$\begin{aligned} A_{\mathbf{k},\mathbf{k}} &= -\sum_{n=1}^5 g^t t_n \beta_n - \mu_f - \sum_{\sigma} \frac{1}{4} J g^J (\cos(k_x) \chi_x(\mathbf{q} = (0,0)) + \cos(k_y) \chi_y(\mathbf{q} = (0,0))) \\ &= \varepsilon(\mathbf{k}) - \mu_f \\ A_{\mathbf{k},\mathbf{k}+\mathbf{q}} &= -\frac{1}{4} J g^J \left( \cos(k_x + \frac{1}{2} q_x) \chi_x(\mathbf{q}) + \cos(k_y + \frac{1}{2} q_y) \chi_y(\mathbf{q}) \right) (\mathbf{q} \neq (0,0)) \end{aligned} \quad (3.27)$$

In order to reduce computation time I invoke a procedure called the superlattice method in momentum space. I separate all the  $\mathbf{k}$  points in the momentum space into different groups. Within each group I diagonalize a smaller matrix (rather than a matrix containing all the  $\mathbf{k}$  points in my truncated momentum space). This method is summarized as follows: (also in Fig. 3.5)

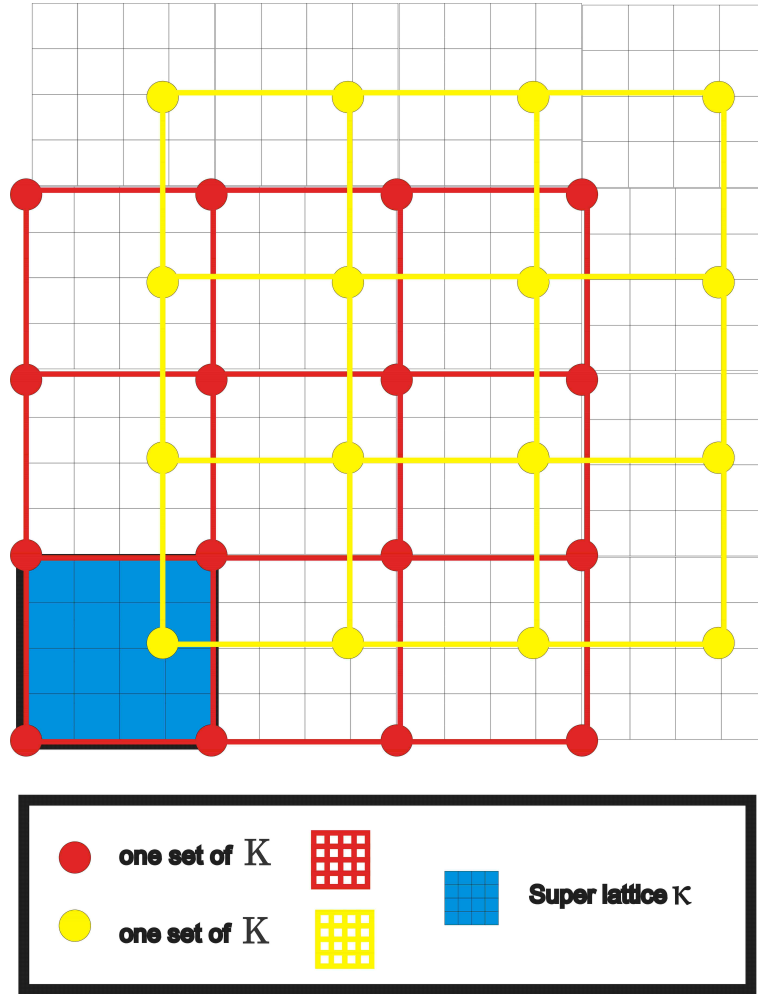


Figure 3.5: *Cartoon drawing of supercell and superlattice in  $\mathbf{k}$  space*

A specific  $\mathbf{k}$  point in momentum space can be connected by all  $\mathbf{q}$  vectors with a set of  $\mathbf{k}'$ . All of the bond terms connecting  $\mathbf{k}$  and  $\mathbf{k}'$  enter the matrix. I call all these  $\mathbf{k}$  points which belong to a set  $\mathbb{K}$ . The matrix dimension of all connecting  $\mathbf{k}$  points is the dimension of the set  $\mathbb{K}$ . The dimension of the set  $\mathbb{K}$  is  $D * D$ , ( $D = M * M$ ) accordingly. In the same way, every single  $\mathbf{k}$  point in momentum space I choose belong to a corresponding set  $\mathbb{K}$ . This allows us to maintain the matrix dimension to be  $D * D$ . In order to sum over all

the  $\mathbf{k}$  point, I treat the whole system as a summation of all the existing set  $\mathbb{K}$ . In other words, all the of set  $\mathbb{K}$  form another super lattice which I call the supper lattice  $\kappa$ . Increasing the dimension of the supper lattice  $\kappa$  will increase the computing time linearly. On the other hand, by increasing the dimension of  $\mathbb{K}$ , the computing time will increase by the power law. Thus this is an economic way deal with larger system sizes.

### 3.4 Uniform Normal State without Symmetry Breaking

The simplest case is the normal state in the Fermi liquid regime. In this case, there is only  $\chi_\eta(\mathbf{q} = (0, 0))$  left in the Hamiltonian, all the other  $\chi_\eta(\mathbf{q} \neq (0, 0)) = 0$ . The Fermi surface is a continuous contour in momentum space. This is my starting point, the non-interacting band structure before multiple scattering is taken into consideration. It is necessary to study this simplest case because there is an underlying instability due to the topology of the Fermi surface. In order to show the generality of the situations in underdoped cuprates, I consider two slightly different band parameters [99] [98] at doping  $x = 0.125$ . They share similar characters. Fig. 3.6 (a)(b) show the continuous contour of the trajectory of the poles. These are generic cases since the tips of the Fermi surface at the antinodal region are not particularly tuned to be parallel to each other, which is closer to the real materials measured by experimentalists.

When the electron Fermi surface “nests” with a specific band structure, the Fermi surface has the tendency towards instability. In order to lower the energy, the systems tends to open up gaps to form density wave orders. This is so called Fermi surface nesting [100] [101]. To gain more insight into the situation, I need to take a look at an important quantity: the wave-vector-dependent susceptibility  $\Gamma(\mathbf{q})$ . The definition of  $\Gamma(\mathbf{q})$  is the following

$$\Gamma(\mathbf{q}) = \sum_{\mathbf{k}, \sigma} \frac{f(\varepsilon_{\mathbf{k}}) - f(\varepsilon_{\mathbf{k}+\mathbf{q}})}{\varepsilon_{\mathbf{k}+\mathbf{q}} - \varepsilon_{\mathbf{k}}} \quad (3.28)$$

where  $f(\varepsilon)$  is the Fermi function.  $\mathbf{q}$  is the vector connecting two states at  $\mathbf{k}$  and  $\mathbf{k} + \mathbf{q}$ . The expression for  $\Gamma(\mathbf{q})$  contains  $\frac{1}{\varepsilon_{\mathbf{k}+\mathbf{q}} - \varepsilon_{\mathbf{k}}} = \frac{1}{\Delta\varepsilon}$ , where  $\Delta\varepsilon$  is the energy difference between occupied and unoccupied states. Therefore, the maximum contribution will come from states when  $\mathbf{q}$  are connecting the occupied and unoccupied states near an equal energy contour, which is the

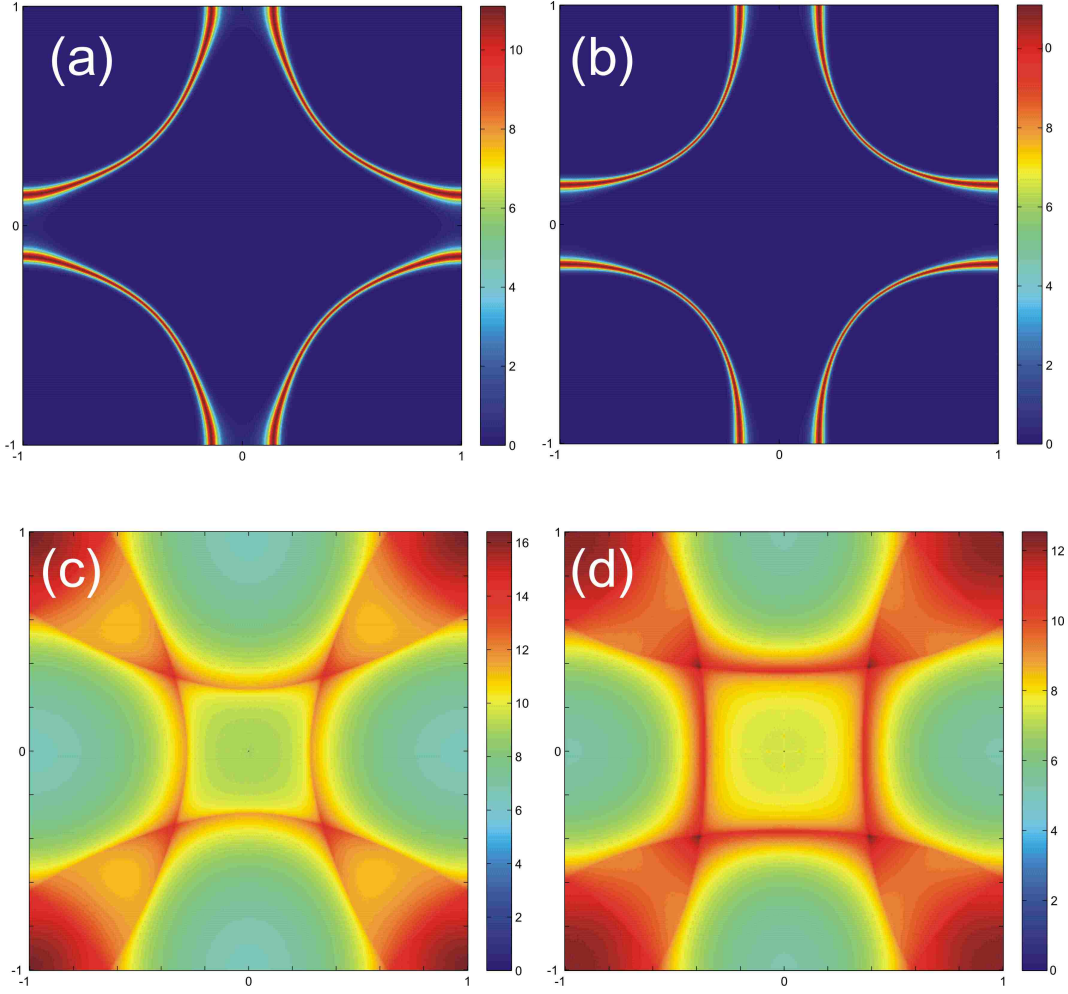


Figure 3.6: (a) ~ (b) Continuous Fermi surface plot for underdoped cuprates, at doping  $x = 0.125$ . (a)  $J=0.12$  eV,  $t = (0.36, -0.12, 0.028, 0.024, -0.024)$  eV. (b)  $J=0.12$  eV,  $t = (0.48, -0.16, 0.05, 0.05, -0.05)$  eV (c) ~ (d) Wave vector dependent susceptibility  $\Gamma(\mathbf{q})$  (Joint density of states) plot for underdoped cuprates, at doping  $x = 0.125$ . (c)  $J=0.12$  eV,  $t = (0.36, -0.12, 0.028, 0.024 - 0.024)$  eV. (d)  $J=0.12$  eV,  $t = (0.48, -0.16, 0.05, 0.05, -0.05)$  eV

Fermi surface. I calculate the wave-vector-dependent susceptibility of the two cases respectively. The maps as a function of  $\mathbf{q}$  is shown in Fig. 3.6 (c) (d).

Along the  $(0, 0) - (\pi, 0)$  direction: In the first case the dominant susceptibility is around the wave vector  $q_1 = (\frac{2\pi}{6}, 0)$ , and in the second case the dominant susceptibility is around the wave vector  $q_1 = (\frac{2\pi}{5}, 0)$ . In general, there is one promising peak along  $(\pi, 0)$  direction:  $q_1 = (\frac{2\pi}{n}, 0)$ .

Along the  $(0, 0) - (\pi, \pi)$  direction: In the first case the dominant susceptibility is around the wave vector  $q_d = (\frac{2\pi}{6}, \frac{2\pi}{6})$  and  $q_\pi = (\pi, \pi)$ , and in the second case the dominant susceptibility is around the wave vector  $q_d = (\frac{2\pi}{5}, \frac{2\pi}{5})$  and  $q_\pi = (\pi, \pi)$ . In general, there are two promising peaks along  $(\pi, \pi)$  direction:  $q_d = (\frac{2\pi}{n}, \frac{2\pi}{n})$  and  $q_\pi = (\pi, \pi)$

Nevertheless, the peaks are not only limited along the x,y axis or along the diagonal of the Brillouin zone, they actually form a "hot square" around zero. That is precisely the reason why I want to treat every possible wave vector as an independent order parameter in  $\chi$ , although I am focusing on the most dominating ones as described above.

Using the periodicity in k-space, I can get the relationship between these wave vectors,

$$\begin{aligned} q_d &= q_\pi + q_7 \\ |q_d| &\simeq \sqrt{2}|q_1| \end{aligned} \tag{3.29}$$

When the AF zone boundary cuts through the Fermi surface, there are 8 interceptions, labeled by a pair of red dots, a pair of blue dots, a pair of yellow dots, and a pair of pink dots in one Brillouin zone as shown in Fig. 3.7 (a).  $q_1$  is the connecting vector of the two dots with the same color, as shown in Fig. 3.7 (d).  $q_7$  and  $q_d$  are the connecting vectors of the two dots with different colors, where  $q_7$  can straddle across to adjacent Brillouin zone and it

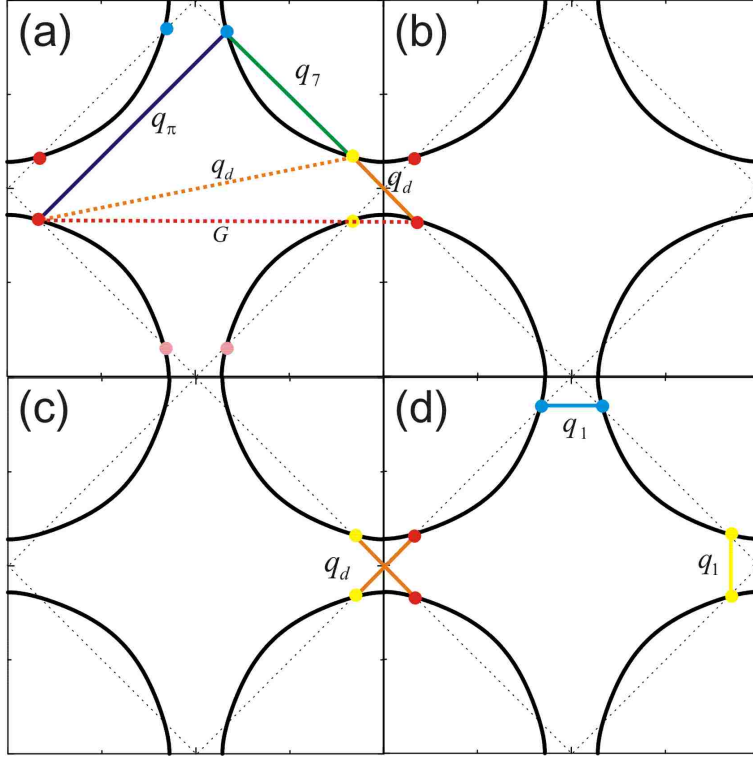


Figure 3.7: *Relationship between different characteristic wave vectors.  $q_\pi, q_d, q_7, q_1$*

has its equivalence in the same Brillouin zone due to the periodic boundary condition. This is shown in Fig. 3.7 (a)(b). This definition is close but not limited to the definition one can find in the experimental observations in the superconducting state [102] [103].

Now I turn my attention to the density wave instability around these dominating  $q$  wave vectors [104]. According to the definition of my order parameter for the bond:

$$\chi_\eta(Q) = \frac{1}{2N} \sum_{k\sigma} \cos(k_\eta + \frac{1}{2}Q_\eta) \langle C_{k,\sigma}^\dagger C_{k+Q,\sigma} + h.c. \rangle \quad (3.30)$$

$Q$  is the density wave vector. It is natural to think that the underdoped cuprates inherit the antiferromagnetism of the half filled Mott Insulator.

This is why the new added AF zone boundary in momentum space is quite special.  $q_7$ ,  $q_d$  and  $q_1$  are connecting the hot spots created by this boundary. The AF long range order  $Q = (\pi, \pi)$  is the first natural candidate for the bond ordering. But this is not the case when my discussion is limited in the case that the time reversal symmetry is conserved in the system. The reason is the following.

First I take a Hermitian conjugate of the order parameter in Equation. 3.30,

$$\chi_\eta^*(Q) = \frac{1}{2N} \sum_{k\sigma} \cos(k_\eta + \frac{1}{2}Q_\eta) \langle C_{k+Q,\sigma}^\dagger C_{k,\sigma} + h.c. \rangle \quad (3.31)$$

Also if I change  $k$  into  $k'$  in Equation. 3.30,

$$k' = k + Q, Q = (\pi, \pi) \quad (3.32)$$

And I can get the following relation:

$$\chi_\eta(Q) = \frac{1}{2N} \sum_{k\sigma} \cos(k_\eta + \frac{1}{2}Q_\eta + \pi) \langle C_{k+Q,\sigma}^\dagger C_{k+Q+Q,\sigma} + h.c. \rangle \quad (3.33)$$

Since  $2\pi$  is the periodicity of  $C_k$ , so  $C_{k+Q+Q,\sigma} = C_{k,\sigma}$ . I can rewrite Equation. 3.33 into the following term:

$$\chi_\eta(Q) = \frac{1}{2N} \sum_{k\sigma} \cos(k_\eta + \frac{1}{2}Q_\eta + \pi) \langle C_{k+Q,\sigma}^\dagger C_{k,\sigma} + h.c. \rangle \quad (3.34)$$

From equations 3.31 and 3.34, I can get:

$$\chi_\eta^*(Q) = -\chi_\eta(Q) \quad (3.35)$$

My assumption is the bond order parameter is real, this yields:

$$\chi_\eta^*(Q) = \chi_\eta(Q) \quad (3.36)$$

From Equation. 3.35 and Equation. 3.36, I get

$$\chi_\eta(\pi, \pi) = 0 \tag{3.37}$$

As a result, the system won't have a bond density wave which shows the  $(\pi, \pi)$  ordering if I insist on preserving the time reversal symmetry. But as I discussed before the inheritance from the Mott Insulator is still in the underdoped cuprates, that is why all the dominating density wave instabilities are closely related to the AF zone boundary.

### 3.5 Commensurate Bond Density Wave State

As discussed in the beginning of this chapter, the term commensurate wave vector means that the elemental density wave vector,  $q = \frac{N}{M} * (2\pi)$ , denominator is a small integer number. Take  $\frac{N}{M} = \frac{1}{5}$  for example, the allowed scattering is the combination of the multiples of the following  $\mathbf{Q}$  vectors:

$$\begin{aligned}\mathbf{Q}_{1,0} &= \left(\frac{1}{5}, 0\right) * (2\pi) \\ \mathbf{Q}_{0,1} &= \left(0, \frac{1}{5}\right) * (2\pi) \\ \mathbf{Q}_{1,1} &= \left(\frac{1}{5}, \frac{1}{5}\right) * (2\pi)\end{aligned}\tag{3.38}$$

After learning the normal state instability in the Fermi liquid regime, I can move on to the next step. First of all, I want to investigate the commensurate case to see how the system reacts to it. I calculated the spectral function  $A(k, \omega)$  to show the Fermi surface of the two cases corresponding to Fig. 3.6. The wave-vector dependent susceptibility exhibits sharp peaks at certain finite elementary  $q = \frac{N}{M} * (2\pi) = \frac{1}{6} * (2\pi)$  and  $q = \frac{N}{M} * (2\pi) = \frac{1}{5} * (2\pi)$  for the two cases respectively. The system is prone to these instabilities which lead to bond density wave ordered states with lower energy than in the uniform state. The resulting spectral intensity maps are shown in Fig. 3.8 after self-consistency calculations. In Fig. 3.8, Fermi surface sections connected by  $\mathbf{q}$  are truncated and there are clear signatures of band folding according to these  $\mathbf{q}$ 's in both cases. Here I use a log scale Fermi surface to show the fine structures of the shadow bands in the Fermi surface topology. There are several wave vectors interlacing the systems, giving the fine structure of the shadow bands. I demonstrated how to achieve these fine structures by simply folding the band according to the instability wave vectors.

It is worth mentioning that different commensurate wave vectors have been tested. They are slightly different than the ones close to the peaks.

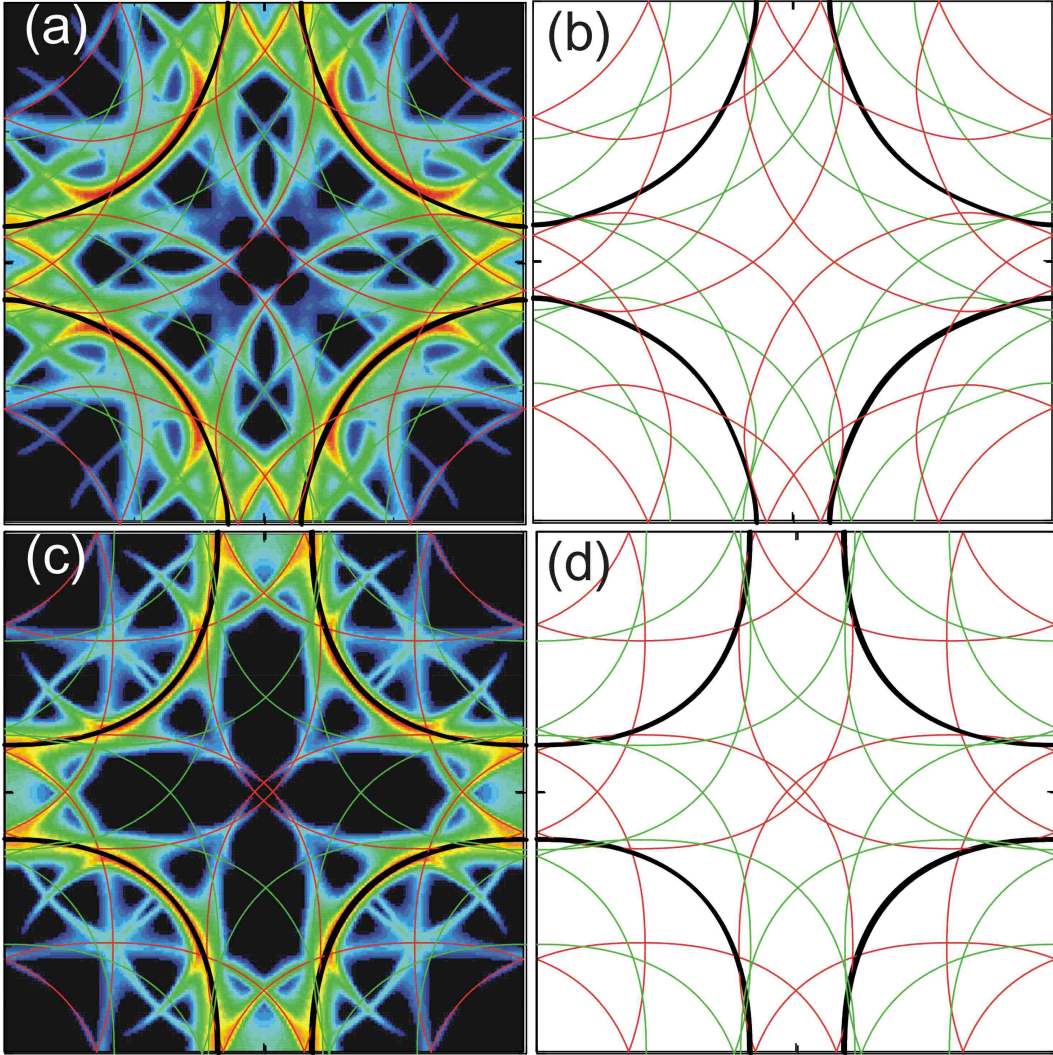


Figure 3.8: *Fermi surface of the commensurate orderings. (a) (b) the elemental vector is  $q = (2\pi)(1/5)$  (c) (d) the elemental vector is  $q = (2\pi)(1/6)$ . The black solid curves are the uniform Fermi surfaces. The red solid curves show the band foldings according to wave vectors  $\mathbf{Q}_d = (q, q), (q, -q), (-q, q), (-q, -q)$ . And the green solid curves show the band foldings according to  $\mathbf{Q}_1 = (q, 0), (-q, 0), (0, q), (0, -q)$ . (b) is overlaid on top of the log scale plot of the Fermi surface (a). And (d) is superimposed on top of the log scale plot of the Fermi surface (c).*

These commensurate wave vectors have been tested as a base vector to solve the self-consistency equations and there is no finite value around the other  $q$  values. They all recover to the uniform case after convergence, if  $q$  is not matching the wave-vector-dependent susceptibility peaks.

Similar features have been achieved on an  $80 * 80$  systems with supercell technique in the spatially unrestricted system. The ground state converged to a checkerboard state with a wave vector  $q^* = \frac{N}{M} * (2\pi) = \frac{1}{5} * (2\pi)$  with slightly different hopping integrals [64]. It also yields partially gapped segments near  $(0, \pm\pi)$  and  $(\pm\pi, 0)$  on the Fermi surface. This indicates the density wave state has lower energy than the uniform Fermi liquid state, and the (logarithmic) divergence when  $q$  approach to  $q^*$  leads to the instability around it.

### 3.6 The Emergence of the Fermi Arc: From the Commensurate Bond Density Wave State to the Incommensurate Bond Density Wave State

Now I have explored the possibility for the commensurate scattering case. Let's remind ourselves of the structure of the Hamiltonian I am investigating in Equation. 3.3. For the commensurate case, the number in a set of  $\mathbf{k}$  which are connected by  $\mathbf{Q} = n\mathbf{q}$  is limited to be small, so the role of  $\hat{H}_s$  is relatively clear. It tends to open up a gap according to the instability wave vector. When  $M$  in  $q = \frac{N}{M} * (2\pi)$  gets larger, there is more freedom in the choice of  $\mathbf{Q}$  which can connect different  $\mathbf{k}$  in order to lower the energy. In other words, there is an ensemble of  $\mathbf{Q}$  around the commensurate wave vector and every one of them can result in elimination of the state at the Fermi level due to scattering. They are not isolated either, and they are all connected and enter the Hamiltonian as a nonseparable part  $\hat{H}_s$ .

$\hat{H}_s$  is a rather complex term to interpret. Its effect is not straightforward but rather a chaotic one. To gain more insight of incommensurate multiple scattering process, I calculate the spectral function  $A(\mathbf{k}, \omega)$  and plot the Fermi surface as in Fig. 3.9(a) ~ (d). In the graph I show the comparison between commensurate multiple scattering process Fig. 3.9(a) and incommensurate multiple scattering process Fig. 3.9(b). To take a closer look of the low intensity spectrum in the antinodal region, I plot the same Fermi surface by lower the intensity by 10 times to show how the fine structures of the shadow bands change when I increase incommensurability by large commensurations, see Fig. 3.9(c) ~ (d).

As can be seen from Fig. 3.9 there are several points worth noticing. First of all, compared to the commensurate scattering case, in the incommensurate case there is further elimination of states in the antinodal  $(\pi, 0)$  and  $(0, \pi)$

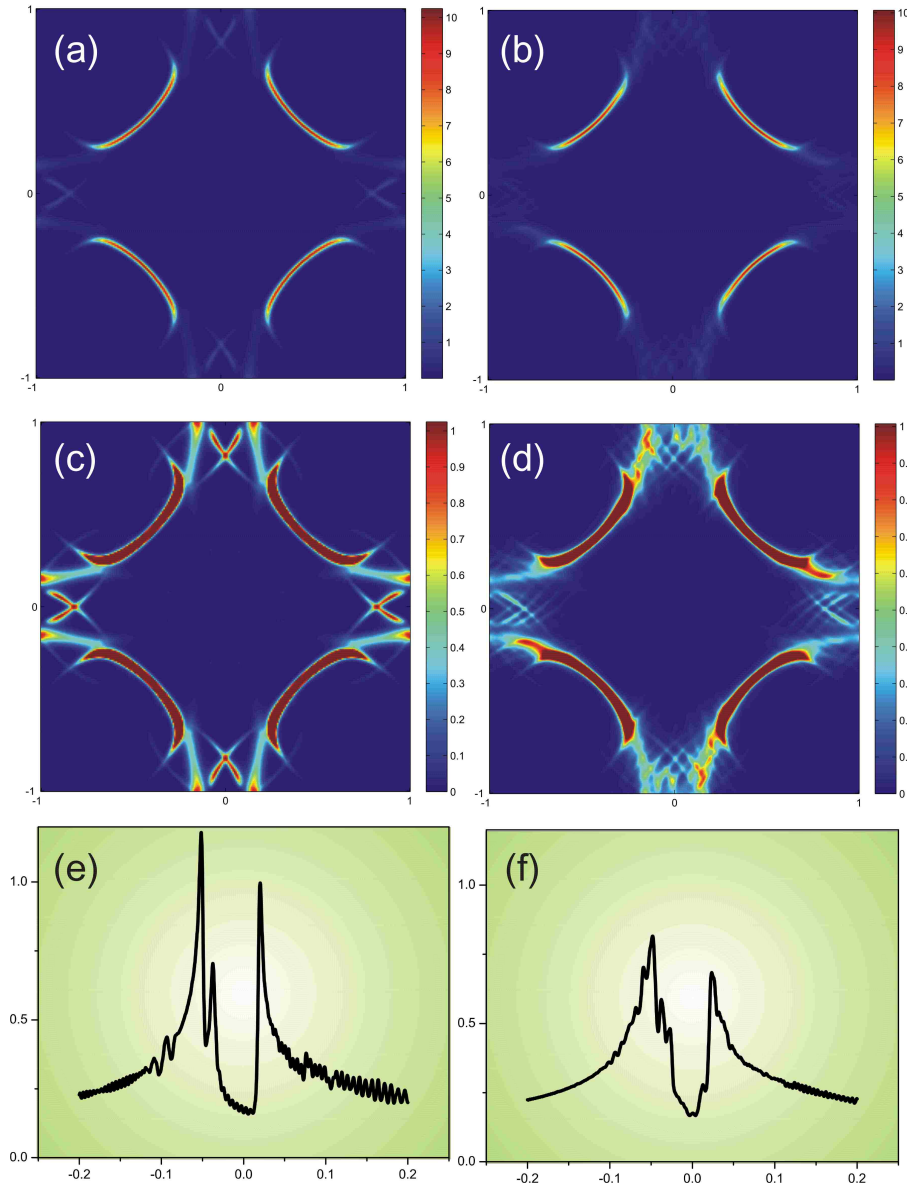


Figure 3.9: (a) Fermi surface of the commensurate ordering case with unit wave vector  $q = \frac{1}{6}(2\pi)$ . (b) Fermi surface of incommensurate ordering case with unit wave vector  $q = \frac{4}{23}(2\pi)$ . (c) Same plot as (a) by lowering the intensity 10 times. (d) Same plot as (b) by lowering the intensity 10 times. (e) Density of states of the commensurate ordering case with unit wave vector  $q = \frac{1}{6}(2\pi)$ . (f) Density of states of the incommensurate ordering case with unit wave vector  $q = \frac{4}{23}(2\pi)$ .

region. Secondly, in the commensurate case, the Fermi surface is truncated according to a single  $\mathbf{Q}$  vector. In the incommensurate case, there are effectively more than one  $\mathbf{Q}$  vectors existing in the converged result which all contribute to lowering the energy. Thirdly, although the Fermi surface in the commensurate case looks similar to the pseudogap state already, clearly band folding is seen in this state. It is less obvious than in the incommensurate case. The continuous contour of Fermi surface is strongly interrupted by the multi wave vector scattering process, resulting in a discontinuous contour more close to the Fermi arc which is observed in the ARPES experiments.

In order to gain more insight into this issue, I calculated the average density of states (DOS) by summing over all the spectrum in  $k$  space for each case. For the commensurate case, there is suppression of density of states below the Fermi energy, resulting in a particle hole asymmetric gap at low energy. While increasing incommensuration, the density of states curve becomes more and more symmetric towards a  $V$  shaped gap, as observed in STM experiments.

With limited computing power, I can not perform a large incommensuration with a larger  $M$  in the denominator, thus both the Fermi arc and the DOS are still pretty close to the commensurate case. For example, there are still multiple shadow bands seen in the antinodal region on the Fermi surface, although with lower intensity. Also, the DOS is not a perfect  $V$  shaped around zero. It is important, though, to study the trend of increasing the incommensuration. I believe that in the true incommensurate case, all these phenomena will recover to the real situation as observed in experiments. I found an alternative way to realize the true incommensuration case which will be discussed in the next chapter.

### 3.7 Doping Dependence of the Incommensurate Bond Density Wave State

With increasing doping, more holes are introduced into the system. As a result the hole like Fermi surface in the Fermi liquid regime around the  $X$  point gets larger and larger. At different doping levels, the AF zone boundary cuts through the Fermi surface at different  $k$  points, as shown in Fig. 3.2. As a result, the wave vector of the susceptibility peak is changing accordingly. In order to demonstrate this, I performed the self-consistency calculation at different dopings. The susceptibility calculations show that with the increase of doping the length of the basic scattering vector  $|q|$  decreases, i.e. the “hot zone” around zero gets smaller and smaller. Also, the absolute value of the wave vector dependent susceptibility peak gets lower and lower. The trend can be easily seen in Fig. 3.10. Detailed measurement of the peak position in Fig. 3.10 is consistent with the “hot spot” (the intersections of the Fermi surface in the uniform case and the AF zone boundary) in Fig. 3.10.

As a consequence of this trend two phenomena can be observed: (1) The corresponding Fermi arc will grow in length while increasing the doping (2) the  $V$ -shaped gap in density of states will get smaller when increasing doping. This can be seen in Fig. 3.11.

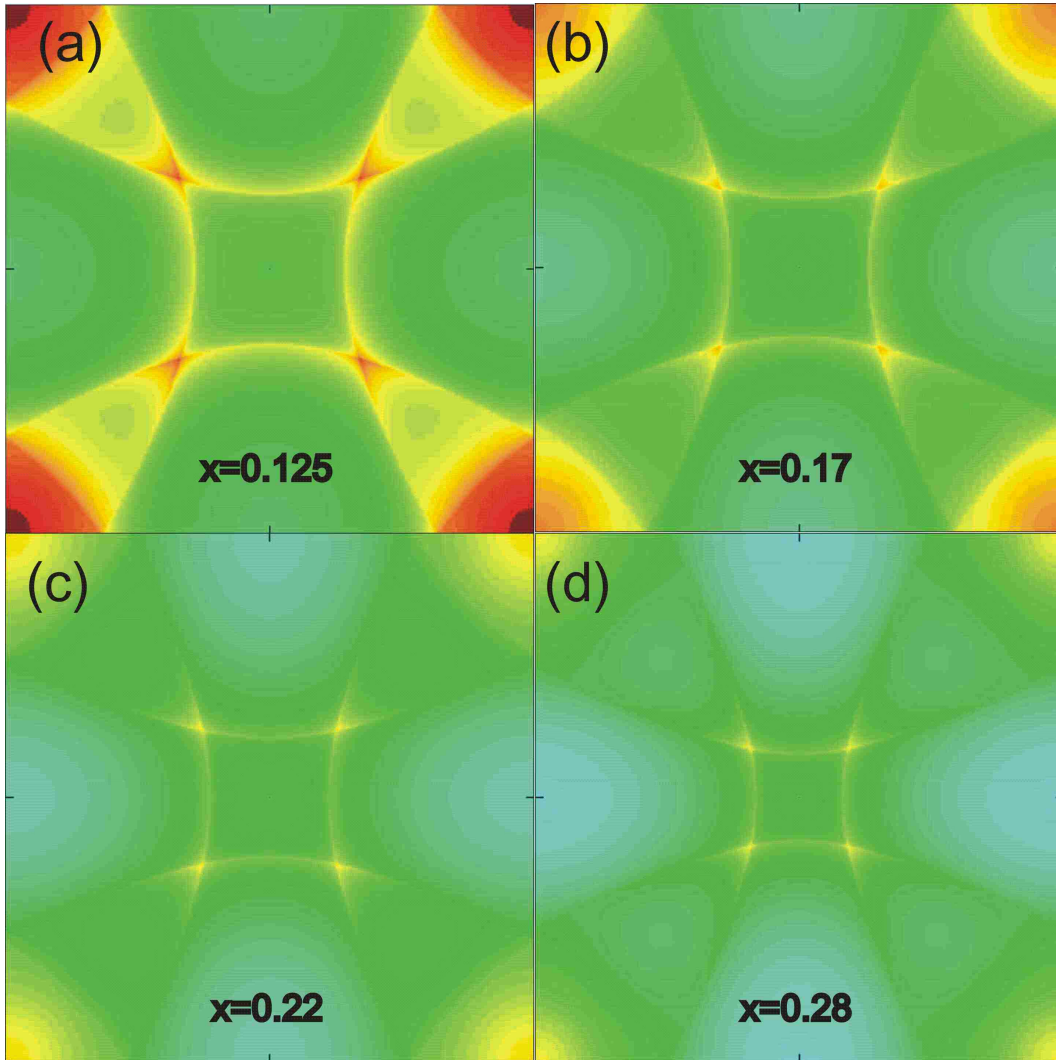


Figure 3.10: *The wave vector dependent susceptibility map at four different doping levels. (a) $x=0.125$ . (b)  $x=0.17$  (c)  $x=0.22$  (d) $x=0.28$ . All the four maps are on the same color scale to be compared on equal footing*

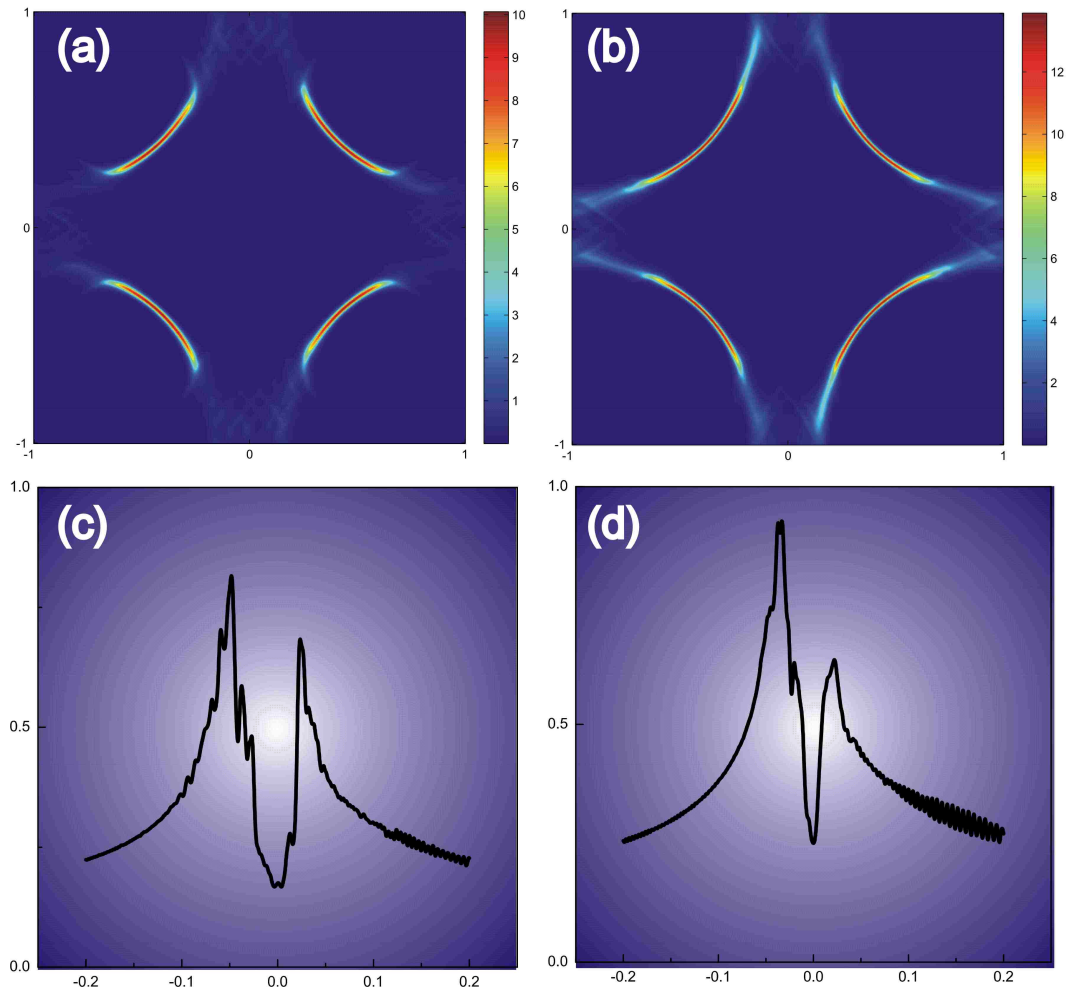


Figure 3.11: (a) Fermi surface at doping  $x=0.125$ , incommensurate wave vector is  $q = (4/23)(2\pi)$ . (b) Fermi surface at doping  $x=0.17$ , incommensurate wave vector is  $q = (4/23)(2\pi)$ . (c) Density of states at doping  $x=0.125$ . (d) Density of states at doping  $x=0.17$ .

### 3.8 Nematic Order and Symmetry Breaking

Regarding the STM observation I discussed earlier, the x-bond oxygen site and y-bond oxygen site inequality within one domain of the sample, the so called electronic nematicity of the states close to the pseudogap energy, is further studied in a recent STM report [105]. Here I examine this issue vis-a-vis incommensurate bond density wave state. The relevant questions are: Will there be a similar nematic order associated with the symmetry breaking? Where does it come from? Why would the system want to choose these states? And does this nematicity have important consequences in the pseudogap state?

First, let's take a look at the order parameter in the incommensurate bond density wave state. I plot  $\chi_x - \chi_y$  in momentum space in Fig. 3.12(a). If there is non vanishing component in this map, that means that the x-bond and y bond are not totally equivalent. As can be seen, this nematicity manifests itself into a 4-fold symmetry broken state. The non vanishing value at zero q means the average of  $\chi_x$  bond and  $\chi_y$  bond are not entirely the same in this state. This can be viewed through the x-bond oxygen site and y-bond oxygen site inequality (for instance, the x-bond has more intensity than the y-bond within one domain of the sample). Certain instances of the combination of x and y bond intensity are degenerate with other separate and different instances (perhaps where the y-bond is more intense than the x-bond) in other domains of the sample. All the other spots with finite q imply that there are fluctuations in this x-bond oxygen site and y-bond oxygen site inequality. Although bonds show the same trend (for example the x-bond has more intensity than the y-bond) within one domain, they still undergo certain fluctuations, see Fig. 3.1. I show a similar bond map in Fig. 3.12(b), the blue region and the yellow region have different bond orientations. In the blue region the x-bond value is bigger than the y bond value and in the yellow region the y-bond value is bigger than the x-bond value. Also the four fold symmetry broken pattern can be seen particularly on the x-axis and

y-axis. It can be seen from Fig. 3.12(a) that the spots on  $(q, 0)$  and  $(0, q)$  are not equivalent.

It is particularly meaningful to dig deeper to see where does this 4-fold broken symmetry state come from. Yamase and Kohno did a systematic study [106] to show that within the slave boson approximation mean field theory, the two-dimensional t-J model has an intrinsic instability toward forming a 4-fold symmetry broken Fermi surface, what they call a quasi 1D state. With the decrease of doping, the instability gets stronger and stronger. I plotted the bond value of the x direction and y direction with respect to doping in Fig. 3.12(d) . It changes from the 4-fold symmetric 2D Fermi surface to a 2-fold symmetric 1D Fermi surface. My doping level is slightly below the critical 2D to 1D transition. In other words, the incommensurate scattering allows the system to undergo a symmetry broken transition to bring out this intrinsic instability, comparing to its commensurate case, which does not break the 4-fold symmetry. In Fig. 3.12(c), I plotted the quasi-1D Fermi surface and the corresponding 4-fold symmetric 2D Fermi surface.

There are two kinds of instabilities existing in the system, the density wave instability and the quasi 1D instability. Both of these become stronger and stronger with deeper and deeper underdoping. The fascinating “strange” behaviors of the pseudogap are the manifestation of these instabilities.

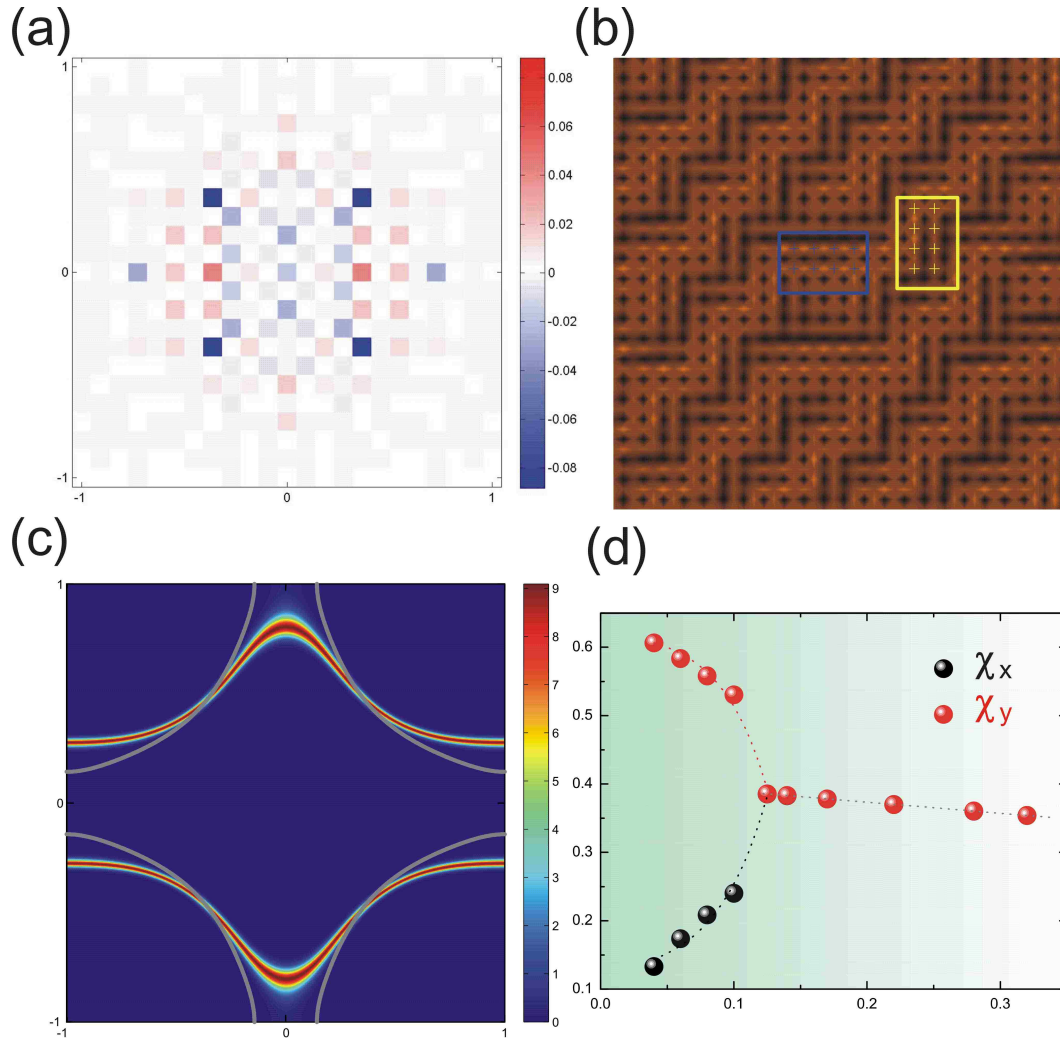


Figure 3.12: (a) The momentum dependence of the order parameter  $\chi_x - \chi_y$ , a typical arrangement in the incommensurate bond density wave state at doping  $x=0.125$ . (b) A bond map corresponding to the ordered state in (a). The blue rectangular region shows one type of domain and the yellow rectangular region shows the other. Within those two regions, the location of the copper site are marked by +. The brighter the color, the bigger the bond value is. (c) Quasi 1D Fermi surface at doping  $x=0.1$ , the grey line shows the corresponding four fold symmetric Fermi surface at the same doping. (d) Bond value of x direction and y direction at different doping levels, with increase of underdoping, such nematicity increases.

# Chapter 4

## Valence Bond Glass Theory in the Pseudogap Regime

### 4.1 Interplay of Incommensurate Valence Bond Order and Electronic Disorder

One common feature in real cuprate materials is intrinsic electronic inhomogeneity. This electronic disorder can potentially pin the low energy fluctuations, resulting in an unusual inhomogeneous state. Here I give a quick survey on electronic disorder in underdoped cuprates.

ARPES groups have studied high quality samples of the chemically substituted Bismuth family of cuprates in the optimal and underdoped regimes where the superconducting energy scale and the pseudogap energy scale are well separated. These substitutions include substituting the cation atom Ca by Y in bilayer  $Bi_2Sr_2Ca_{1-x}Y_xCu_2O_8$  (substituted Bi2212) and substituting the Sr ion in apical planes by a trivalent Lanthanide ( $Ln = La, Bi, \text{ or } Eu$ ) in single-layered  $Bi_2Sr_{2-z}Ln_zCuO_{6+\delta}$  (substituted Bi2201). The ARPES group led by Ding studied the evolution of the pseudogap with continuous underdoping [22], pushing the underdoping threshold continuously to the su-

perconducting/insulating phase boundary. By substituting the divalent Sr ions by the trivalent Bi ions in the apical plane in  $Bi_2Sr_{2-z}Bi_zCuO_{6+\delta}$ , Luo et al.[107] have achieved a continuous range of substitutional densities from  $z = 0$  to  $z = 0.5$ . The large range has provided the possibility to detect the true underdoped properties. This has been confirmed by measuring the underlying Fermi surface volume [22]. There are two effects of such doping: The first effect is that it changes the hole density because of the difference in valence electrons: there is one more electron in the outmost layer in Bi as compared to Sr. The second effect is that it increases the off-plane disorder due to the  $Sr : Bi$  ionic radii mismatch in the apical plane [108] [109]. The ARPES data of Ding et al has been compared with those obtained in heavily underdoped Bi2212  $Bi_2Sr_2Ca_{1-x}Y_xCu_2O_8$ [21] and the nonsuperconducting zero temperature pseudogap phase of  $Ca_{1.95}Na_{0.05}CuO_2Cl_2$ [110]. All these materials have shown disorder as a common character in the underdoped regime.

On the other hand, mounting STM evidence shows that electronic disorder is an inherent feature of the cuprates. Experimentalists have observed nanoscale single particle spectral gap disorder as well as short-range ordered checkerboard density of states modulations. The inhomogeneity of gaps has been reported in  $Bi_2Sr_2CaCu_2O_{8+x}$  by several groups [111] [112] [113] [114], and also on  $Ca_{2-x}Na_xCuO_2Cl_2$  [115]. When superconductivity is weakened under various conditions, the short-range ordered checkerboard and short-range ordered DOS modulations have been reported by several group [112] [115] [116] [117]. The electronic disorder is important because the periodically modulated checkerboard states have rather short correlation lengths (about 20 lattice spacings). This is further reflected in the finite width of the non dispersive peak structure in the Fourier spectrum of the tunneling conductance maps. The observed quasiparticle interference patterns signaled by the dispersive peak structures with bias energy inside the superconducting gap[118] have been attributed to off plane dopant disorder induced elastic

scattering of the quasiparticles. This picture has gained theoretical support [119][120]. It is natural to suspect that the short range ordered patterns are manifestations of certain density-wave states [65] [121] [122] [123] [124] [125] [126] pinned by electronic disorder. In fact, they are not inconsistent with the disorder induced glassy phase or the nematic liquid crystal of stripes. [52].

It is then important to determine the cause of this electronic disorder and how to treat it. The out of plane ionic dopant is the most prominent candidate. It can be interstitial as in  $Bi_2Sr_2CaCu_2O_{8-x}$ ; it can be substitutional as in  $La_{2-x}Sr_xCuO_4$  and  $Ca_{2-x}Na_xCuO_2Cl_2$ ; and it can be in combination with chemical substitutions as in  $Bi_2Ln_{2-z}Bi_zCuO_{6+x}$  (Ln-Bi2201). The classification of different family of cuprates and their disorder are shown in Fig. 4.1.

While donating carriers to the  $CuO_2$  planes, the out of plane ionic dopants are also introducing off-plane electrostatic potential centers which directly affect the low energy electronic states in the  $CuO_2$  planes at the same time. The screening of the dopant electrostatic potential is highly nonlinear in doped Mott insulators since the kinetic energy required for charge redistribution is frustrated due to strong coulomb correlation. This nonlinear screening also leads to spatially inhomogeneous electronic states. [96] [119].

To include the effects of this intrinsic electronic disorder, I include the electrostatic potential originating from the off plane ionic dopants. Previous studies of doping induced inhomogeneity treat interstitial ionic dopants as random charge centers [96] [99]. Here I utilize a hard wall condition counting in the number of dopants. As shown in Fig. 4.2, oxygen dopants are randomly distributed outside the  $CuO_2$  plane following a hard wall condition, exposing the correlated electrons in the  $CuO_2$  plane to the off-plane dopant potential through the relation:

$$H_{imp} = \sum_{kq\sigma} V(q) C_{k+q,\sigma}^\dagger C_{k,\sigma} \quad (4.1)$$

Halogen Family	Bi Family	(a)	(b)	(c)																										
Pb Family	1L TI Family																													
La Family	2L Family	(1)		(c-1)																										
YBCO Family	Hg Family	(a-1)		(c-1)																										
		<table border="1"> <thead> <tr> <th></th> <th><math>T_c</math></th> </tr> </thead> <tbody> <tr> <td><math>\text{Ca}_{2-x}\text{Na}_x\text{CuO}_2\text{Cl}_2</math></td> <td>26</td> </tr> <tr> <td><math>\text{Pb}_2\text{Sr}_{2-x}\text{La}_x\text{Cu}_2\text{O}_z</math></td> <td>33</td> </tr> <tr> <td><math>\text{La}_{2-x}\text{M}_x\text{CuO}_4</math></td> <td>39</td> </tr> <tr> <td><math>\text{Bi}_2\text{Sr}_{1-x}\text{Ln}_x\text{CuO}_{6+\delta}</math></td> <td>38</td> </tr> <tr> <td><math>\text{TlBa}_{1+x}\text{La}_{1-x}\text{CuO}_5</math></td> <td>45</td> </tr> </tbody> </table>		$T_c$	$\text{Ca}_{2-x}\text{Na}_x\text{CuO}_2\text{Cl}_2$	26	$\text{Pb}_2\text{Sr}_{2-x}\text{La}_x\text{Cu}_2\text{O}_z$	33	$\text{La}_{2-x}\text{M}_x\text{CuO}_4$	39	$\text{Bi}_2\text{Sr}_{1-x}\text{Ln}_x\text{CuO}_{6+\delta}$	38	$\text{TlBa}_{1+x}\text{La}_{1-x}\text{CuO}_5$	45		<table border="1"> <thead> <tr> <th></th> <th><math>T_c</math></th> </tr> </thead> <tbody> <tr> <td><math>\text{Sr}_2\text{CuO}_2\text{F}_{2+x}</math></td> <td>46</td> </tr> <tr> <td><math>\text{La}_2\text{CuO}_{4+\delta}</math></td> <td>45</td> </tr> <tr> <td><math>\text{Tl}_2\text{Ba}_2\text{CuO}_{6+\delta}</math></td> <td>93</td> </tr> <tr> <td><math>\text{HgBa}_2\text{CuO}_{4+\delta}</math></td> <td>98</td> </tr> </tbody> </table>		$T_c$	$\text{Sr}_2\text{CuO}_2\text{F}_{2+x}$	46	$\text{La}_2\text{CuO}_{4+\delta}$	45	$\text{Tl}_2\text{Ba}_2\text{CuO}_{6+\delta}$	93	$\text{HgBa}_2\text{CuO}_{4+\delta}$	98				
	$T_c$																													
$\text{Ca}_{2-x}\text{Na}_x\text{CuO}_2\text{Cl}_2$	26																													
$\text{Pb}_2\text{Sr}_{2-x}\text{La}_x\text{Cu}_2\text{O}_z$	33																													
$\text{La}_{2-x}\text{M}_x\text{CuO}_4$	39																													
$\text{Bi}_2\text{Sr}_{1-x}\text{Ln}_x\text{CuO}_{6+\delta}$	38																													
$\text{TlBa}_{1+x}\text{La}_{1-x}\text{CuO}_5$	45																													
	$T_c$																													
$\text{Sr}_2\text{CuO}_2\text{F}_{2+x}$	46																													
$\text{La}_2\text{CuO}_{4+\delta}$	45																													
$\text{Tl}_2\text{Ba}_2\text{CuO}_{6+\delta}$	93																													
$\text{HgBa}_2\text{CuO}_{4+\delta}$	98																													
		(2)	(b-2)	(c-2)																										
		(a-2)		(c-2)																										
		<table border="1"> <thead> <tr> <th></th> <th><math>T_c</math></th> </tr> </thead> <tbody> <tr> <td><math>\text{La}_{2-x}\text{Sr}_x\text{CaCu}_2\text{O}_6</math></td> <td>60</td> </tr> <tr> <td><math>(\text{La}_{1-x}\text{Ca}_x)(\text{Ba}_{1.75-x}\text{La}_{0.25+x})\text{Cu}_3\text{O}_y</math></td> <td>80</td> </tr> <tr> <td><math>\text{Bi}_{2+x}\text{Sr}_{2-x}\text{CaCu}_2\text{O}_{8+\delta}</math></td> <td>90</td> </tr> </tbody> </table>		$T_c$	$\text{La}_{2-x}\text{Sr}_x\text{CaCu}_2\text{O}_6$	60	$(\text{La}_{1-x}\text{Ca}_x)(\text{Ba}_{1.75-x}\text{La}_{0.25+x})\text{Cu}_3\text{O}_y$	80	$\text{Bi}_{2+x}\text{Sr}_{2-x}\text{CaCu}_2\text{O}_{8+\delta}$	90	<table border="1"> <thead> <tr> <th></th> <th><math>T_c</math></th> </tr> </thead> <tbody> <tr> <td><math>\text{Pb}_2\text{Sr}_2\text{Y}_{1-x}\text{Ca}_x\text{Cu}_3\text{O}_{8+\delta}</math></td> <td>80</td> </tr> <tr> <td><math>\text{Y}_{1-x}\text{Ca}_x\text{Ba}_2\text{Cu}_3\text{O}_{7-\delta}</math></td> <td>90</td> </tr> <tr> <td><math>\text{Bi}_2\text{Sr}_2\text{Ca}_{1-x}\text{Y}_x\text{Cu}_3\text{O}_{8+\delta}</math></td> <td>96</td> </tr> </tbody> </table>		$T_c$	$\text{Pb}_2\text{Sr}_2\text{Y}_{1-x}\text{Ca}_x\text{Cu}_3\text{O}_{8+\delta}$	80	$\text{Y}_{1-x}\text{Ca}_x\text{Ba}_2\text{Cu}_3\text{O}_{7-\delta}$	90	$\text{Bi}_2\text{Sr}_2\text{Ca}_{1-x}\text{Y}_x\text{Cu}_3\text{O}_{8+\delta}$	96	<table border="1"> <thead> <tr> <th></th> <th><math>T_c</math></th> </tr> </thead> <tbody> <tr> <td><math>\text{YBa}_2\text{Cu}_3\text{O}_{7-\delta}</math></td> <td>93</td> </tr> <tr> <td><math>\text{TlBa}_2\text{CaCu}_2\text{O}_{7+\delta}</math></td> <td>110</td> </tr> <tr> <td><math>\text{Tl}_2\text{Ba}_2\text{CaCu}_2\text{O}_{8+\delta}</math></td> <td>110</td> </tr> <tr> <td><math>\text{HgBa}_2\text{CaCu}_2\text{O}_{6+\delta}</math></td> <td>120</td> </tr> </tbody> </table>		$T_c$	$\text{YBa}_2\text{Cu}_3\text{O}_{7-\delta}$	93	$\text{TlBa}_2\text{CaCu}_2\text{O}_{7+\delta}$	110	$\text{Tl}_2\text{Ba}_2\text{CaCu}_2\text{O}_{8+\delta}$	110	$\text{HgBa}_2\text{CaCu}_2\text{O}_{6+\delta}$	120
	$T_c$																													
$\text{La}_{2-x}\text{Sr}_x\text{CaCu}_2\text{O}_6$	60																													
$(\text{La}_{1-x}\text{Ca}_x)(\text{Ba}_{1.75-x}\text{La}_{0.25+x})\text{Cu}_3\text{O}_y$	80																													
$\text{Bi}_{2+x}\text{Sr}_{2-x}\text{CaCu}_2\text{O}_{8+\delta}$	90																													
	$T_c$																													
$\text{Pb}_2\text{Sr}_2\text{Y}_{1-x}\text{Ca}_x\text{Cu}_3\text{O}_{8+\delta}$	80																													
$\text{Y}_{1-x}\text{Ca}_x\text{Ba}_2\text{Cu}_3\text{O}_{7-\delta}$	90																													
$\text{Bi}_2\text{Sr}_2\text{Ca}_{1-x}\text{Y}_x\text{Cu}_3\text{O}_{8+\delta}$	96																													
	$T_c$																													
$\text{YBa}_2\text{Cu}_3\text{O}_{7-\delta}$	93																													
$\text{TlBa}_2\text{CaCu}_2\text{O}_{7+\delta}$	110																													
$\text{Tl}_2\text{Ba}_2\text{CaCu}_2\text{O}_{8+\delta}$	110																													
$\text{HgBa}_2\text{CaCu}_2\text{O}_{6+\delta}$	120																													
		(3)	(b-3)	(c-3)																										
		(a-3)		(c-3)																										
		<table border="1"> <thead> <tr> <th></th> <th><math>T_c</math></th> </tr> </thead> <tbody> <tr> <td><math>\text{Bi}_{2+x}\text{Sr}_{2-x}\text{Ca}_2\text{Cu}_3\text{O}_{10+\delta}</math></td> <td>110</td> </tr> <tr> <td><math>\text{TlBa}_{2-x}\text{Ca}_2\text{Cu}_3\text{O}_{9+\delta}</math></td> <td>123</td> </tr> </tbody> </table>		$T_c$	$\text{Bi}_{2+x}\text{Sr}_{2-x}\text{Ca}_2\text{Cu}_3\text{O}_{10+\delta}$	110	$\text{TlBa}_{2-x}\text{Ca}_2\text{Cu}_3\text{O}_{9+\delta}$	123	<table border="1"> <thead> <tr> <th></th> <th><math>T_c</math></th> </tr> </thead> <tbody> <tr> <td><math>\text{TlBa}_2\text{Ca}_{2-\epsilon}\text{Cu}_3\text{O}_{9+\delta}</math></td> <td>131</td> </tr> </tbody> </table>		$T_c$	$\text{TlBa}_2\text{Ca}_{2-\epsilon}\text{Cu}_3\text{O}_{9+\delta}$	131	<table border="1"> <thead> <tr> <th></th> <th><math>T_c</math></th> </tr> </thead> <tbody> <tr> <td><math>\text{TlBa}_2\text{Ca}_2\text{Cu}_3\text{O}_{9+\delta}</math></td> <td>133</td> </tr> <tr> <td><math>\text{Tl}_2\text{Ba}_2\text{Ca}_2\text{Cu}_3\text{O}_{10+\delta}</math></td> <td>125</td> </tr> <tr> <td><math>\text{HgBa}_2\text{Ca}_2\text{Cu}_3\text{O}_{10+\delta}</math></td> <td>135</td> </tr> </tbody> </table>		$T_c$	$\text{TlBa}_2\text{Ca}_2\text{Cu}_3\text{O}_{9+\delta}$	133	$\text{Tl}_2\text{Ba}_2\text{Ca}_2\text{Cu}_3\text{O}_{10+\delta}$	125	$\text{HgBa}_2\text{Ca}_2\text{Cu}_3\text{O}_{10+\delta}$	135								
	$T_c$																													
$\text{Bi}_{2+x}\text{Sr}_{2-x}\text{Ca}_2\text{Cu}_3\text{O}_{10+\delta}$	110																													
$\text{TlBa}_{2-x}\text{Ca}_2\text{Cu}_3\text{O}_{9+\delta}$	123																													
	$T_c$																													
$\text{TlBa}_2\text{Ca}_{2-\epsilon}\text{Cu}_3\text{O}_{9+\delta}$	131																													
	$T_c$																													
$\text{TlBa}_2\text{Ca}_2\text{Cu}_3\text{O}_{9+\delta}$	133																													
$\text{Tl}_2\text{Ba}_2\text{Ca}_2\text{Cu}_3\text{O}_{10+\delta}$	125																													
$\text{HgBa}_2\text{Ca}_2\text{Cu}_3\text{O}_{10+\delta}$	135																													

Figure 4.1: Classification of bulk High  $T_c$  cuprates in terms of the disorder site and the number of  $\text{CuO}_2$  layers. Materials belonging to the same family are indicated by the same color. ( This Figure is taken from [108])

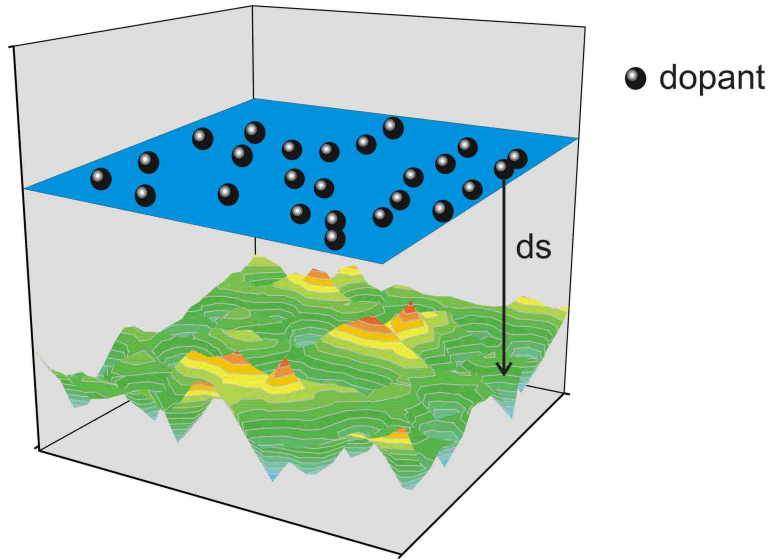


Figure 4.2: *The illustration of introducing the electronic disorder by adding out of plane random ionic dopants. The top plane(blue) is the the dopants plane, and bottom plane (multi color) is the CuO<sub>2</sub> plane. The 3D contour plot represents the hole doping distributions on the CuO<sub>2</sub> plane. In the rainbow color scale, red represents high hole density*

As a result, the doping concentration undergoes a reconstruction due to the nonlinear screening of the dopant potential. Fig. 4.3 shows the induced density inhomogeneity in the presence of out of the plane ionic dopants on a 2D map.

The density inhomogeneity is not periodic and involves a distribution of wave vectors ( $q$ ). As discussed in the previous chapter, a density wave with a unique wavevector  $q$  has several serious difficulties to reconcile with experiments. In the ARPES experiment, there is not even the slightest feature for the emergence of Fermi surface pockets folded along the  $(\pi, \pi)$  boundary. Also, there is no sign of band folding by the commensurate wave vector  $q$ . The pseudogap produced by the commensurate density wave order is quite generically particle-hole asymmetric in the density of states [64] which is inconsistent with experiments that find V-shaped gapping of the low-energy

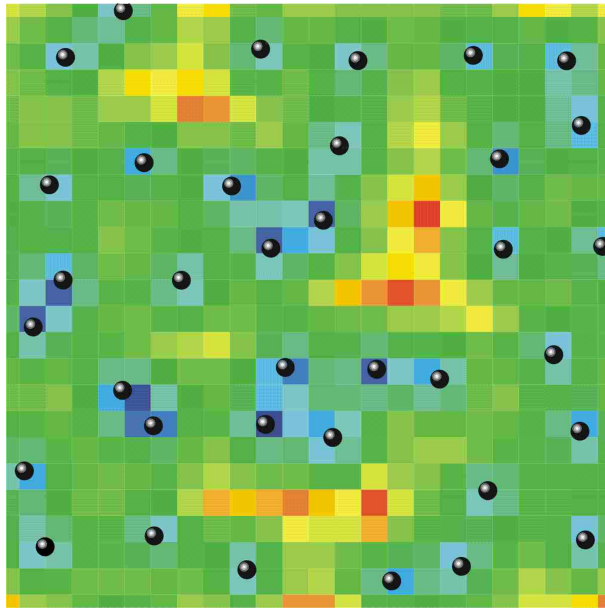


Figure 4.3: *The density map of the  $\text{CuO}_2$  plane, the black balls represent off plane dopants overlaid on top of the density map.*

states. With out of plane random ionic dopants, there is a modulation with many wave vectors comparable to the situation with the incommensurate density wave state. The electronic disorder can effectively pin down the low energy density wave state with multiple incommensurate scattering. Such freedom also allows us to have a Fermi surface with a more relaxed condition, in comparison with models based on Fermi surface nesting. Perfect nesting requires fine tuning of the hopping parameters such that the antinodal sections are parallel and nearly one dimensional [64] [61] [127] [128]. But in most of the cuprates materials exhibiting pseudogap phenomena, the antinodal sections of the Fermi surface are not perfectly parallel and nearly one dimensional. Since I do not require the Fermi surface to be perfectly nested to accommodate the single commensurate  $q$  condition, it is more generic and persuading to show the pseudogap phenomena is a common robust feature of underdoped cuprates.

## 4.2 Unified Theory of the Doping Induced Electronics Disorder and the Incommensurate Bond Density Wave Pseudogap States

In the remaining sections of this thesis I present a unified theory showing that the doping induced electronic disorder pins down the incommensurate bond centered charge density wave pseudogap states. I present this through an explicit calculation based on an extended t-J model including the dopant potential. I show that the pseudogap originates from disordered (or short-ranged ordered) bond-centered charge density waves with a distribution of wavevectors centered around  $q^*$ . This can be viewed as a state arising from the low-lying valence bond fluctuations pinned by electronic disorder and similar in spirit to the disorder induced glassy phases or the nematic liquid crystal of stipes [52].

The antinodal Fermi surface sections are gapped out by the disordered bond density waves, giving rise to a genuine normal state Fermi arc. Short range order is sufficient to produce a pseudogap because the latter is a feature of the quasiparticle excitation energy spectrum and long range coherence is not a prerequisite. As a consequence, there is no true thermodynamic phase transition at  $T^*$  in this approach, which is determined by thermal filling of the antinodal pseudogap. The incommensurate bond density wave pseudogap increases and the Fermi arc length shrinks with underdoping. I show that this is due to the weakening of the screening of the dopant potential and the increase of  $q^*$ . This doping dependence of the pseudogap is consistent with the experiments.

Our theory provides a microscopic realization of the generic two-gap scenario for the nodal-antinodal dichotomy of an electronic origin through the exchange interaction  $J$ . Below  $T_c$  the Fermi arc collapses as the d-wave superconducting gap opens and coexists competitively with the disordered bond density wave pseudogap. The evolution of the local and the momentum

space spectroscopy and the phase diagram as a function of doping and temperature captures the salient properties of the pseudogap phenomena and the electronic disorder revealed by recent ARPES and STM experiments, especially in the chemically substituted bilayer and single-layer Bi-based high  $T_c$  superconductors where the pseudogap and the pairing gap energy scales are well separated. I show that the superconducting gap and the pseudogap contain distinctly different information in many aspects. This is a strong support for the pseudogap picture that emerges from the generic two-gap scenario.

### 4.3 Extended t-J Model with Spatially Unrestricted Gutzwiller Approximation

Extending the original t-J model to adapt this disordered nature requires considering some new elements, different from the Hamiltonian I used in the last chapter. The first is to include the long-range coulomb interaction coming from both other electrons in the same plane and the dopants off the plane for an electron on a particular site. This inclusion of the long-range Coulomb interaction is necessary because the charge distribution is inhomogeneous due to the dopant potential. The second new element is to use a spatially unrestricted Gutzwiller approximation which depends on the local densities. Since there is inhomogeneity in the  $CuO_2$  plane, different sites and bonds have different renormalization factors [99].

First I introduce two Coulomb potential terms into the original t-J model:

$$H = H_{tJ} + \sum_{i \neq j} \hat{n}_i V_{ij}^c \hat{n}_j - \sum_i V_i \hat{n}_i \quad (4.2)$$

$$H_{tJ} = - \sum_{i \neq j} P_i t_{ij} C_{i\sigma}^\dagger C_{j\sigma} P_j + J \sum_{\langle i,j \rangle} (\mathbf{S}_i \cdot \mathbf{S}_j - \frac{1}{4} \hat{n}_i \hat{n}_j) \quad (4.3)$$

The long-range Coulomb interaction  $V_{ij}^c = \frac{V_c}{|r_i - r_j|}$  between the electrons in the  $CuO_2$  plane provides the important screening of the electrostatic potential from off-plane dopants. The local doping concentration is given by  $x_i = 1 - n_i$ , where  $n_i = \langle \hat{n}_i \rangle = \langle C_{i\sigma}^\dagger C_{i\sigma} \rangle$ . On a square lattice of  $N_s$  sites, the average doping is given by  $x = (1/N_s) \sum_i x_i$ . The long-range Coulomb interaction is treated by the Hartree approximation.

In addition to the in-plane long range Coulomb interactions, I include the electrostatic potential between the dopants and the electrons in the  $CuO_2$  plane. The total ionic potential, which is the summation of the coulomb potential from all the off plane dopants, is given by:

$$V_i = \sum_{l=1}^{N_d} \frac{V_d}{\sqrt{|r_i - r_l|^2 + d_s^2}} \quad (4.4)$$

In Eq. 4.4,  $N_d = xN_s$  is the number of dopants and  $d_s$  is the setback distances [96][99] (see Fig. 4.2 ). Summing over all lattice sites on the plane, one gets the last term in Eq. 4.2.

The projection operator  $P$  indicates that double occupation of a site must be removed due to the strong on-site Coulomb repulsion (or the large charge transfer gap). In order to account for the interplay between strong correlation and disorder, I consider the spatially unrestricted Gutzwiller approximation where  $P_i$  depends on the spatial density distribution. In this way, the t-J model in the projected Hilbert space is replaced by one in the unprojected space with renormalized hopping and the exchange parameters which take into account the basic physics of Mottness. In the Gutzwiller approximation, the effect of projection results in renormalizations of the hopping matrix and the superexchange,

$$\begin{aligned} t_{ij} &\rightarrow g_{ij}^t t_{ij} \\ J &\rightarrow g_{ij}^J J \end{aligned} \quad (4.5)$$

The spatially unrestricted Gutzwiller factors can be derived as I have discussed in the previous chapter:

$$\begin{aligned}
g_{ij}^t &= \frac{\langle \Psi | C_{i\sigma}^\dagger C_{j\sigma} | \Psi \rangle}{\langle \Psi_0 | C_{i\sigma}^\dagger C_{j\sigma} | \Psi_0 \rangle} = \sqrt{\frac{4x_i x_j}{(1+x_i)(1+x_j)}} \\
g_{ij}^J &= \frac{\langle \Psi | \mathbf{S}_i \cdot \mathbf{S}_j | \Psi \rangle}{\langle \Psi_0 | \mathbf{S}_i \cdot \mathbf{S}_j | \Psi_0 \rangle} = \frac{4}{(1+x_i)(1+x_j)}
\end{aligned} \tag{4.6}$$

In a disordered electronic state, the factors depend on the local dopings at the sites connected by the hopping and the superexchange processes. Since the strong correlation effects are taken into account by the Gutzwiller renormalization, it is now justified to decouple the exchange term by the valence bond in the particle-hole and the particle-particle channel in terms of the bond  $\chi_{ij}$  and the pairing  $\Delta_{ij}$ , as previously discussed. Finally I reach the renormalized mean-field Hamiltonian for the extended t-J model:

$$\begin{aligned}
H_{GA} &= - \sum_{i \neq j} g_{ij}^t t_{ij} C_{i\sigma}^\dagger C_{j\sigma} + \sum_i \varepsilon_i C_{i\sigma}^\dagger C_{i\sigma} - \sum_i \lambda_i n_i \\
&\quad - \frac{1}{4} J \sum_{\langle i,j \rangle} g_{ij}^\chi (\chi_{ij}^* C_{i\sigma}^\dagger C_{j\sigma} + h.c. - |\chi_{ij}|^2) \\
&\quad - \frac{1}{4} J \sum_{\langle i,j \rangle} g_{ij}^\Delta (\Delta_{ij}^* \epsilon_{\sigma\sigma'} C_{i\sigma}^\dagger C_{j\sigma'} + h.c. - |\Delta_{ij}|^2)
\end{aligned} \tag{4.7}$$

Where  $g_{ij}^\chi, g_{ij}^\Delta = g_{ij}^J$  are the Gutzwiller renormalization factor. The local energy for the electrons is  $\varepsilon_i = V_{sc}(i) + \lambda_i - \mu_f$ , where  $\mu_f$  is the chemical potential and  $\lambda_i$  is the fugacity. The chemical potential and the local fugacity together with the third term in the Hamiltonian ensure the equilibrium condition for local occupation  $n_i = \langle C_{i\sigma}^\dagger C_{i\sigma} \rangle$ .  $V_{sc}(i)$  is the screened Coulomb

potential:

$$V_{sc}(i) = V_i + V_c \sum_{j \neq i} \frac{x_i - x_j}{|r_i - r_j|}. \quad (4.8)$$

I use  $J = 120meV$  and up to the fifth nearest neighbor hopping in order to utilize the band structure in experiments [99] [98]. It does not require the fine tuning of parallel antinodal Fermi surfaces, since my results are not sensitive to this condition. I set  $V_c = V_d = 0.5$  eV and  $d_s = 1$  in units of the lattice constant [96]. To account for their Coulomb repulsion, the ionized dopant configurations are generated randomly with a hard-core condition of one to three lattice spacings.

The Hamiltonian in Eq. 4.7 can be diagonalized in real space by solving the corresponding Bogoliubov–de Gennes equations to obtain the eigenstates  $\gamma_n^\dagger$  and  $\gamma_n$  with energy  $E_n$ ,  $n = 1, \dots, 2N_s$ ,

$$\mathbb{H} = \sum_{ij} (C_{i\uparrow}^\dagger, C_{i\downarrow}) \begin{pmatrix} K_{ij} & F_{ij} \\ F_{ij}^* & -K_{ij}^* \end{pmatrix} \begin{pmatrix} C_{j\uparrow} \\ C_{j\downarrow}^\dagger \end{pmatrix} + H_0$$

where the matrix elements can be written as:

$$\begin{aligned} H_0 &= \frac{1}{4} J \sum_{\langle ij \rangle} g_{ij}^J (|\chi_{ij}|^2 + |\Delta_{ij}|^2) + \sum_i \lambda_i (x_i - 1) \\ F_{ij} &= \frac{1}{4} J g_{ij}^J \Delta_{ij} \sum_{\eta} \delta_{j, i+\eta} \\ K_{ij} &= [-g_{ij}^t t_{ij} - \frac{1}{4} J g_{ij}^J \chi_{ij}^*] \sum_{\eta} \delta_{j, i+\eta} + (V_{sc}(i) + \lambda_i - \mu_f) \delta_{ij} \end{aligned} \quad (4.9)$$

The fermion creation and annihilation operators can be expanded in this

basis according to:

$$\begin{aligned}
C_{i\uparrow}^\dagger(t) &= \sum_n u_n^*(i) \gamma_n^\dagger e^{iE_n t/\hbar} \\
C_{i\downarrow}(t) &= \sum_n v_n^*(i) \gamma_n^\dagger e^{iE_n t/\hbar}
\end{aligned}
\tag{4.10}$$

where  $[u_n(i), v_n(i)]$  is the wave function at site  $i$ . The order parameters and the local hole density can be expressed in terms of the wave functions as follows:

$$\begin{aligned}
\Delta_{ij} &= \sum_n [u_n(i)v_n^*(j)][1 - f(E_n)] - v_n^*(i)u_n(j)[f(E_n)] \\
\chi_{ij} &= \sum_n [v_n(i)v_n^*(j)][1 - f(E_n)] + u_n^*(i)u_n(j)[f(E_n)] \\
1 - x_i &= \sum_n [|v_n(i)|^2[1 - f(E_n)] + |u_n(i)|^2[f(E_n)]]
\end{aligned}
\tag{4.11}$$

where  $f(E_n)$  is the usual Fermi distribution function. I minimize the ground state energy of  $\langle H_{GA} \rangle$  through self-consistently determined  $(x_i, \lambda_i, \chi_{ij}, \Delta_{ij})$  on  $24 \times 24$  systems for different realizations of the dopant configurations.

Recall the relationship between the two mean field order parameters: the spin singlet pair  $\Delta_{ij} = \langle C_{i\uparrow} C_{j\downarrow} - C_{i\downarrow} C_{j\uparrow} \rangle$  and the orbital hybridization  $\chi_{ij} = \langle C_{i\uparrow}^\dagger C_{j\uparrow} + C_{i\downarrow}^\dagger C_{j\downarrow} \rangle$ . Away from half filling, the equivalence of these two order parameters no longer holds, although they are driven by the same superexchange  $J$ . The nature of  $\Delta_{ij}$  is considered solved by the short-range RVB theory. The spin-singlet valence bond pairs are mobilized by the doped holes and tend to condense into a d-wave SC state below  $T_c$  [91]. The nature of  $\chi_{ij}$  and its interplay with  $\Delta_{ij}$  is still unsettled.

To gain more insight, I decompose  $\chi_{ij}$  into low angular momentum ex-

tended s-wave and d-wave components:

$$\begin{aligned}\chi_s(i) &= \frac{1}{4}S_{ij}\chi_{ij} \\ \chi_d(i) &= \frac{1}{4}d_{ij}\chi_{ij}\end{aligned}\tag{4.12}$$

In Eq. 4.12, the form factors  $S_{ij} = 1$  are for the four bonds emanating from site  $i$ . The form factors  $d_{ij} = \pm 1$  are for the bonds along the  $x$  and  $y$  direction respectively. In momentum space, the fluctuation valence bonds are:

$$\begin{aligned}\chi_s(q) &= \sum_{k\sigma} \gamma_k C_{k+q,\sigma}^\dagger C_{k\sigma} + h.c. \\ \chi_d(q) &= \sum_{k\sigma} \beta_k C_{k+q,\sigma}^\dagger C_{k\sigma} + h.c.\end{aligned}\tag{4.13}$$

where  $\gamma_k = \cos k_x + \cos k_y$  are the extended s-wave factors and  $\beta_k = \cos k_x - \cos k_y$  are the d-wave form factors. In the uniform system, without considering the off-plane disorder,  $\chi_s(q = 0) = \chi_s(0) \neq 0$ .  $\chi_s(0)$  renormalizes the nearest neighbor hopping. It is the uniform Fermi liquid phase. At the same time  $\chi_d(q \rightarrow 0) = 0$ . No d-wave bond order can exist with both the translational and time-reversal symmetry preserved.

A non-vanishing d-wave component is allowed if translational symmetry and/or time reversal symmetry are broken. For example, if the imaginary part  $\chi_d''(q^*) \neq 0$  for  $q^* = (\pi, \pi)$ , it becomes the staggered flux phase [55] [56], also known as the DDW phase[57] or the orbital current phase.

I show here that without breaking the time reversal symmetry the ‘‘order parameter’’ of the pseudogap phase originates from the real part of the d-wave valence bond  $\chi_d'(q) \neq 0$ . In the presence of doping induced disorder, the pseudogap phase can be well described by a glassy d-wave valence

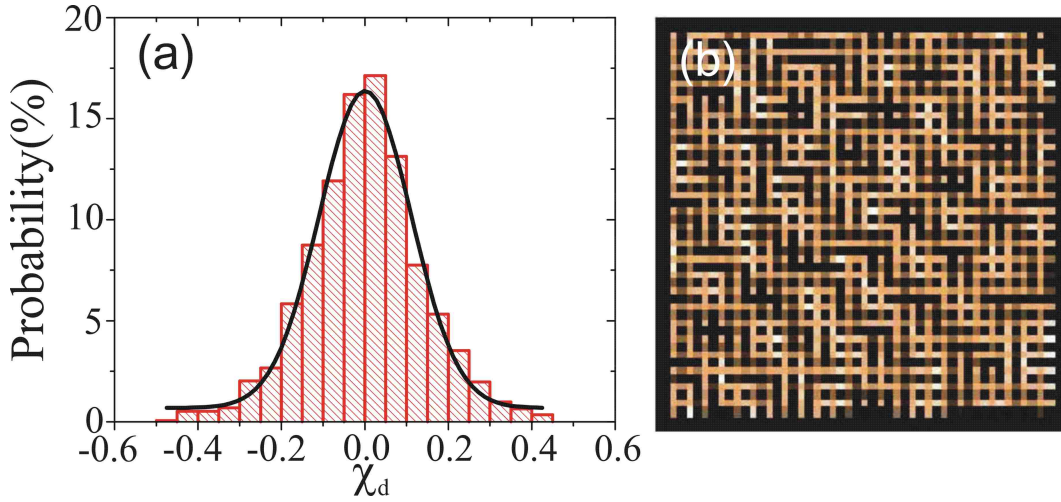


Figure 4.4: (a) Distribution of d-wave valence bond showing glassy order at doping level  $x=0.125$ . (b) A field of view of bond map  $\chi_{ij}$  in real space for a particular sample.

bond centered density wave with a distribution of  $q$  centered around the incommensurate ordering wave vectors  $q^*$  in the clean case as discussed in the previous chapter.

## 4.4 Normal State and Pseudogap Phase

### 4.4.1 The Fermi Arc and “V” Shaped Density of States

First I study the normal state pseudogap phase above  $T_c$  or the zero temperature pseudogap phase when the pairing is suppressed. I show that the glassy valence bond density waves produce the pseudogap phenomena. I achieve the normal state above  $T_c$  by setting  $\Delta = 0$ .

The valence bond is real and fluctuates due to the disordered dopant potential. A statistical study of the bond order is shown in Fig. 4.4. Unlike in the clean case without symmetry breaking where  $\chi_d$  is strictly zero, the disorder potential breaks translational symmetry and  $\chi_d$  becomes non

vanishing. The histogram of the valence bond order parameter  $\chi_d$  in the normal state at an average doping  $x = 0.125$  is shown in Fig. 4.4 (a). By summing different  $24 \times 24$  sites samples, the histogram shows the statistics of the bond order within a larger sample as measured in experiments. It follows a Gaussian distribution with a zero mean. The root-mean-squared fluctuation represents a nonzero glassy order parameter  $\delta_\chi = \sqrt{\sum_i \chi_d(i)^2}/N_s$  at this doping for the Valence Bond Glass phase.  $N_s$  is the size of the sample. I note that the glassy dynamics of the valence bond were studied in the weak-coupling metallic phase of the Hubbard-Heisenberg model at half filling [129]. In contrast, here I discuss the glassy nature of the state away from half filling. First, it is not a solid due to its disordered nature, this can be seen clearly in the bond map in Fig. 4.4 (b). Second, it is not a liquid because of the existing short-range order in the system, which I am going to discuss in detail in the later sections. This is a valence bond glass state (VBG state). It is an incommensurate bond density wave state pinned by the disordered dopant potential. It possesses a glassy order which is different from the valence bond solid (VBS). The most succinct feature of the valence bond glass is the emergence of the pseudogap and the Fermi arc. The average DOS in Fig. 4.5 shows a remarkable V-shaped pseudogap. The size of the gap is  $\Delta_{pg} \approx 32meV$  at doping  $x = 0.125$ . The gap is approximately symmetrically distributed around the Fermi level due to the d-wave nature of the VBG. Different from the line shape of the density of states plot in the commensurate case in Fig. 3.9(e) the particle-hole symmetry of the pseudogap is approximately restored as observed in the STM experiments.

The calculated spectral intensity at the Fermi energy is plotted in Fig. 4.6. Fig. 4.6(a) shows the intensity with full scale. It reveals a Fermi surface truncated near the antinodes by the pseudogap and a Fermi arc around the nodes which tracks the underlying Fermi surface. The more interesting feature of this pseudogap Fermi surface can be seen when I lower the intensity scale in Fig. 4.6(b). The Fermi arcs around the nodes remain prominent. In

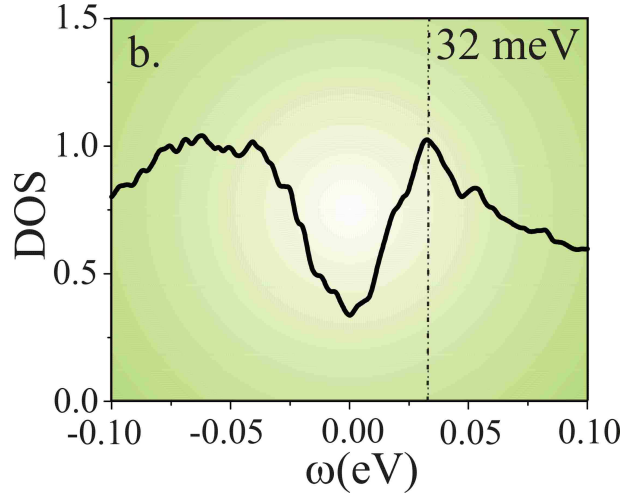


Figure 4.5: *Average density of states plot at  $x = 0.125$  showing the VBG pseudogap, it is symmetric around zero bias and has a clear “V” shape which resembles the d-wave symmetry.*

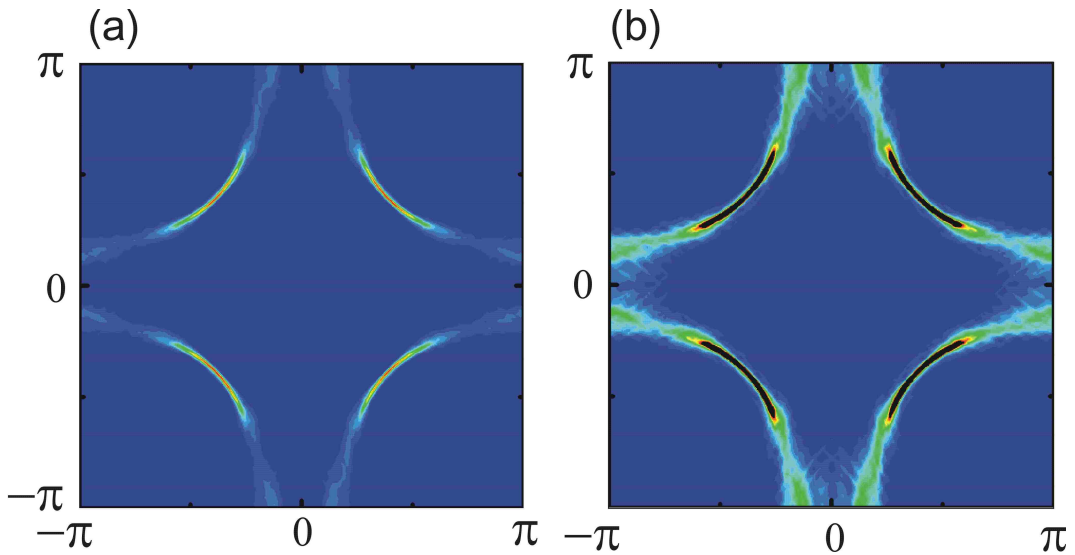


Figure 4.6: *Fermi surface spectrum intensity plot at doping  $x = 0.125$ . (a) Fermi arc with full intensity, the antinodal region is gapped out leaving the gapless nodal region intact. (b) Fermi arc with lower intensity comparing with (a), in the antinodal region no clear sign of band folding.*

the antinodal region there is no signs of band folding. The agreement with the experimentally established phenomenology such as the nodal-antinodal dichotomy strongly suggests that the emergence of the pseudogap is due to the short range order of the incommensurate bond density wave in response to the dopant potential.

## 4.4.2 Understanding the Role of Disordered Potential

The nodal-antinodal dichotomy in the underdoped regime highlights the non-Fermi liquid nature of the VBG pseudogap phase. Its emergence does not require the antinodal Fermi surface sections to be overly parallel and one-dimensional which my parameters relevant to the band structure [98] do not produce. It is sufficient for the quasiparticle dispersion to have a rather flat-band section near the antinodes. In this Fermi liquid limit, I found that the static susceptibility  $S_{\chi_d}^0(q)$  exhibits diverging sharp peaks at  $q^*$ . I have demonstrated that the Fermi surface becomes unstable to superlattice instabilities.

With the presence of the screened potential, the renormalized d-wave charge density wave susceptibility is given by an RPA-like expression:

$$S_{\chi_d}(q) = \frac{S_{\chi_d}^0(q)}{1 + V_{sc}(q)S_{\chi_d}^0(q)} \quad (4.14)$$

In my approach I have exposed the  $CuO_2$  plane to the off-plane dopant potential through  $H_{imp} = \sum_{k,q,\sigma} V(q)C_{k+q,\sigma}^\dagger C_{k,\sigma}$ . The disorder potential  $V(q)$  is generally finite for all  $q$  values with moderate features reflecting the average inter-dopant distance.  $V_{sc}(q)$  is the screened dopant potential by the itinerant carriers.  $V_{sc}(q)$  has substantially weaker spatial variations than the bare ionic potential  $V(q)$ . It is the driving force of the electronic disorder. The divergence of the static susceptibility  $S_{\chi_d}(q)$  is governed by the interplay between the screened potential and the bare susceptibility (joint density of states). This is why the disordered potential introduces a disordered bond density wave, which gaps out the antinodal region of the Fermi surface. My calculation shows the d-wave bond density wave parameter  $\chi_d(q)$  develops a distribution of  $q$ -values, since  $\chi_d(q) = S_{\chi_d}(q)V_{sc}(q)$ . The  $q$  dependence of bond order parameters is plotted for several doping levels in Fig. 4.7. The underlying mechanism of this is in the self-consistent theory, the electronic disorder pins the low-energy bond density wave fluctuations into a glassy

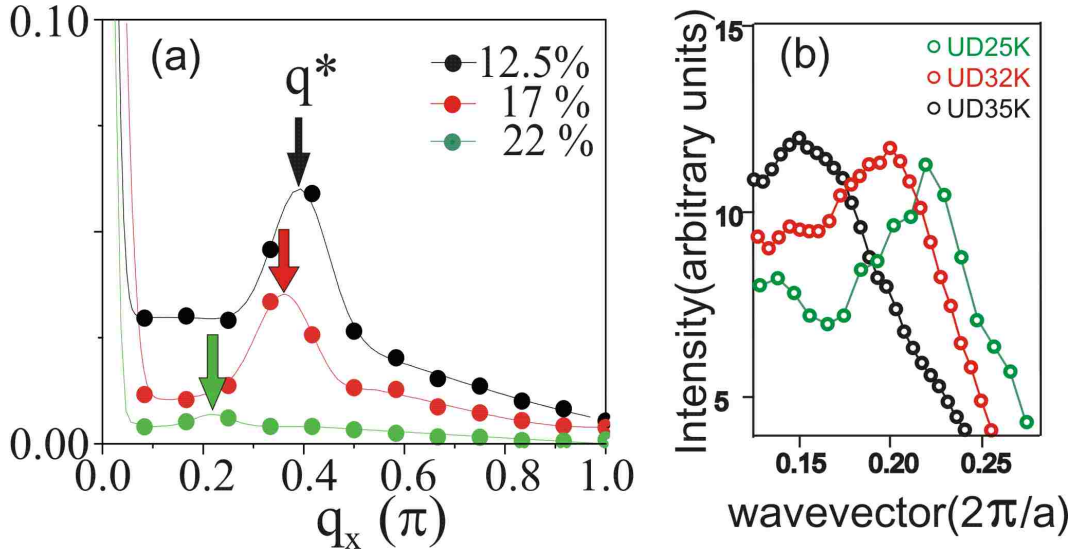


Figure 4.7: (a) 1D Fourier power spectrum  $|\chi_d(q)|$  along  $q_x$  direction at three different doping levels,  $x = 0.125, x = 0.17$  and  $x = 0.22$ . (b) Linecuts along the atomic lattice direction of the Fourier transform of the local density of states maps at three different dopings for  $Bi2201$ . Green is the underdoped sample with  $T_c = 25K$ , red is the underdoped sample with  $T_c = 32K$ , black is the optimally doped sample with  $T_c = 35K$ . The corresponding peak wavevectors are with the wavelengths of  $6.2a_0, 5.1a_0$  and  $4.5a_0$ , respectively. Figure (b) is modified from [26]

phase with distributions of  $\chi_d(q)$  around  $q^*$ . I show the Fourier power spectrum  $|\chi_d(q)|$  in Fig. 4.7(a) along the  $q_x$  direction, where the peak is located at a group of incommensurate wavevectors around  $q_x^* = 0.4\pi$ . The width of the peak indicates the short range nature of the d-wave valence bond order with approximate  $5a \times 5a$  checkerboard pattern. This can be connected to the checkerboard modulations observed by STM [26][130]. The Fourier transform of the local density of states is shown in Fig. 4.7(b). The characteristic instability wave vector  $|q|^*$  changes upon doping. This can be explained by a topology change of the Fermi arc as demonstrated from my calculation in the Fermi liquid regime. It is consistent with the current theoretical and experimental observational trends.

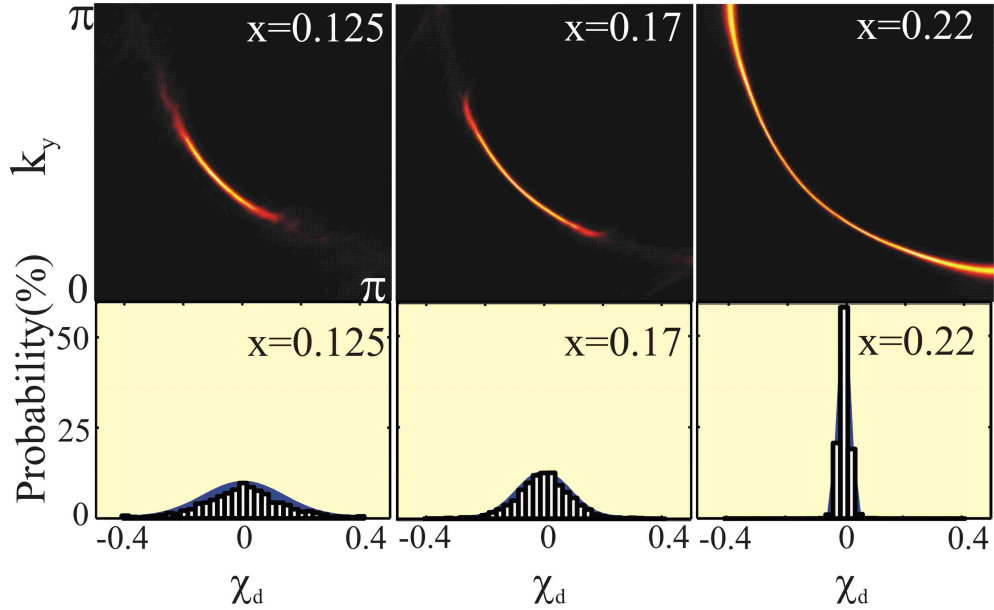


Figure 4.8: *Fermi arc doping dependence at three different doping levels.*

#### 4.4.3 Doping Dependence of the Pseudogap

I study the doping dependence of the disordered d-wave bond centered charge density wave state and the evolution of the pseudogap. This allows me to understand the interplay between the kinetic energy and the d-wave bond centered charge density wave formation in the presence of electronic disorder. The doping dependence of the pseudogap is shown in Fig. 4.8. From the underdoped to the overdoped region, the pseudogap and the Fermi arc give way to a more conventional disordered metal.

In the top three panels of Fig. 4.8 the calculated quasiparticle spectral intensities at their Fermi energy are shown for three ascending doping levels. In the underdoped regime, the spectral intensity reveals the antinodal truncated Fermi surface (Fermi arc). It also reveals that the Fermi arc length increases with increasing doping in agreement with ARPES. From my calculations in the uniform case, it is seen that the divergence in bare susceptibility has a

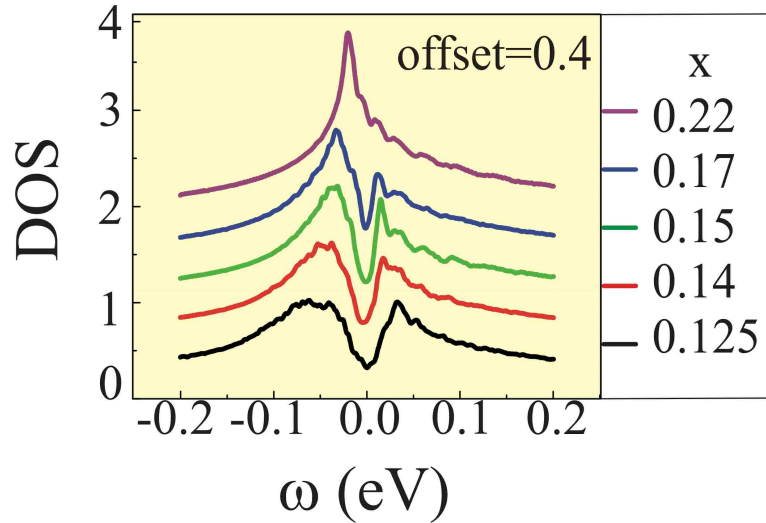


Figure 4.9: *Density of states doping dependence at different doping levels.  $x$  is the doping level.*

smaller and smaller  $q$  with increasing doping, this will result in the growth of the Fermi arc length in the absence of disorder. In the same way, the disordered bond density waves will also respond to the screened susceptibility derived from the bare susceptibility. In Fig. 4.7, with the increase of doping,  $q^*$  becomes smaller and smaller and the peak of  $q^*$  get weaker and weaker. This is one reason for the arc growth in the disordered case. On the other hand, while the density of dopants increases, the screened potential  $V_{sc}(q)$  decreases due to improved screening by more mobile carriers. This leads to weaker fluctuations of the potential, and as a result, the Fermi arc keeps growing with less and less scattering in the antinodal region.

The bottom three panels of Fig. 4.8 show the histograms of the dominant fluctuations in the d-wave component of the valence bonds for three different doping concentrations. They all follow the Gaussian distributions and the root-mean-square fluctuations increase with deepening underdoping. The same reasoning applies. While the density of off-plane dopants increases

for larger doping, the VBG order parameter decreases as a consequence of the improved screening due to higher density of doped carriers i.e. weakened  $V_{sc}(q)$ . The fluctuation strength of the order parameter  $\chi_d$  is closely tied to the pseudogap. The bigger the fluctuation is, the bigger the pseudogap is.

I show in Fig. 4.9 the integrated density of states for several doping concentrations. The pseudogap becomes smaller and shallower with increasing doping. The pseudogap becomes undiscernible beyond  $x = 0.22$  on the shoulder of the Van Hove peak. The phenomena can be explained following the same argument for the arc growth. We can view the density of states as the momentum average of the spectral intensity in k-space. With less quasiparticle scattering in the antinodal region with increasing doping, there will be less elimination of states in the low energy, resulting in a smaller pseudogap.

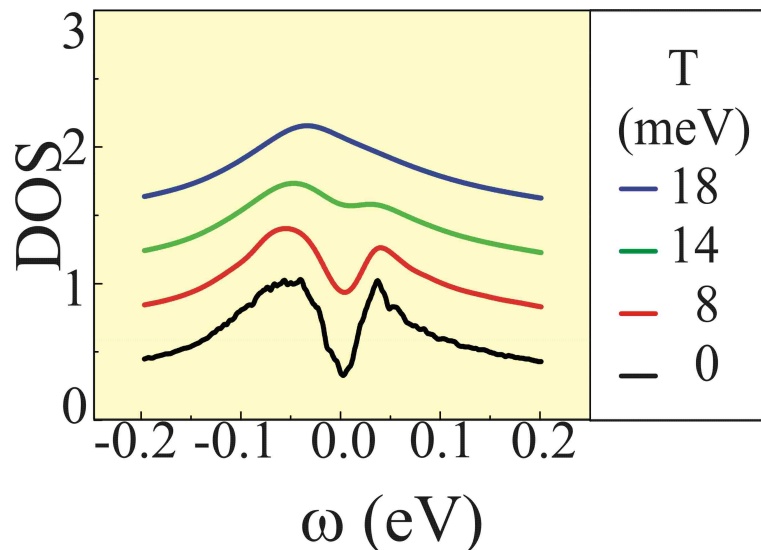


Figure 4.10: *Temperature evolution of VBG pseudogap at doping  $x = 0.125$ .*

#### 4.4.4 Temperature Dependence of the Pseudogap

The temperature evolution of the pseudogap is also studied using the spatially unrestricted Gutzwiller approximation. Compared to the variational Monte Carlo projection, the spatially unrestricted Gutzwiller approximation has its unique strengths. It allows me to study finite temperature properties by minimizing the free energy in the renormalized mean field theory [87] [131].

Rather than a gap closing, I find that upon the increase of temperature, the gap fills up. In Fig. 4.10, I show an example of the temperature evolution of the pseudogap at doping concentration  $x = 0.125$ . The pseudogap temperature  $T^*$  is clearly seen to be determined by the thermal filling of the pseudogap. This indicates that the pseudogap phenomenon is therefore not associated with the phase transition which involves long range order, although experimentally there is still controversy[132]. The thermal filling of the pseudogap is a unique feature of the glassy state.

### 4.4.5 Nodal Antinodal Dichotomy in the Spectral Function

Fig. 4.11(a) shows the momentum-dependence of the symmetrized single-particle spectral function as measured by ARPES at  $x = 0.14$ . It displays the evolution of the quasiparticles along the arc and the opening of the pseudogap at the arc tip which increases towards the antinodes. The signature of the nodal antinodal dichotomy is that the spectrum is gapless along the conducting arc, in comparison with the large gap in the antinodal region. This is consistent with the earlier ARPES observations. In order to scrutinize how the pseudogap opens up along the underlying Fermi surface, the angular dependence of the pseudogap extracted from the symmetrized spectrum function is plotted in Fig. 4.11(b). Away from the zero-gap Fermi arc, the pseudogap follows the d-wave form (dashed line). The Fermi arc can be correspondingly defined by the angles  $\phi$  that span the zero-gap region emanating from 45-degrees. Lee et al. have reported this angular dependence of the spectrum gap in Bi2212 and similar results have been found when the temperature is above the superconducting transition temperature  $T_c$  among three different samples at different dopings [133]. The pseudogap line-shape highlights one of the most significant predictions of the glassy phase: the pseudogap near the antinodes is a soft gap that opens approximately linearly in energy. There are in-gap states left. This is in fact consistent with the ARPES experiments which use the terminology "pseudogap" originally. It is in sharp contrast to the naïve picture of a hard gap that depletes all states near the antinodes below the pseudogap energy scale. This has very important consequences in the superconducting state.

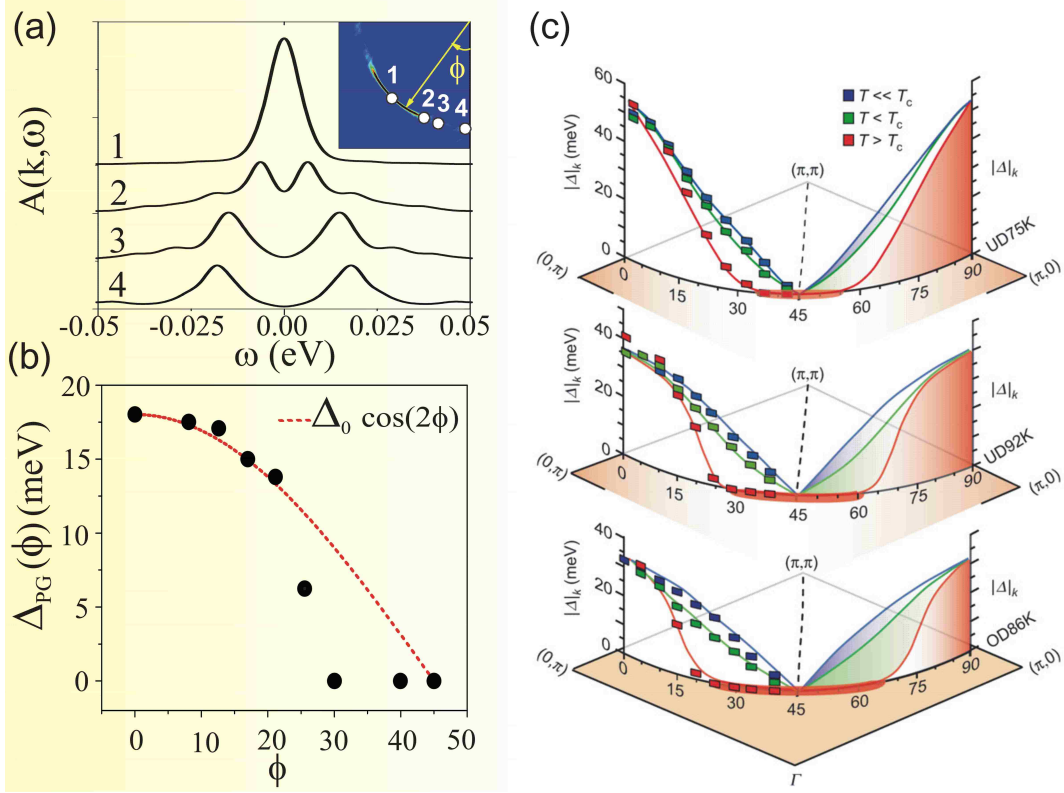


Figure 4.11: (a) Angular dependence of the symmetrized spectral function in momentum space. insert: the definition of angle ( $\phi = 0$  is the nodal point  $\phi = 45^\circ$  is the antinodal region). The white circles are the points where the spectrum function are plotted. (b) The angular dependence of the pseudogap is shown in black dots. The red curve is a d-wave fit used as a guide to the eye. (c) Schematic illustrations of the gap function evolution for three different doping levels of Bi2212, Figure is taken from [133]. (top panel), Underdoped sample with  $T_c = 75K$ . (middle panel), Underdoped sample with  $T_c = 92K$ . (bottom panel), Overdoped sample with  $T_c = 86K$ . At 10 K above  $T_c$  there exists a gapless Fermi arc region near the node; a pseudogap has already fully developed near the antinodal region (red curves). With increasing doping, this gapless Fermi arc elongates (thick red curve on the Fermi surface), as the pseudogap effect weakens.

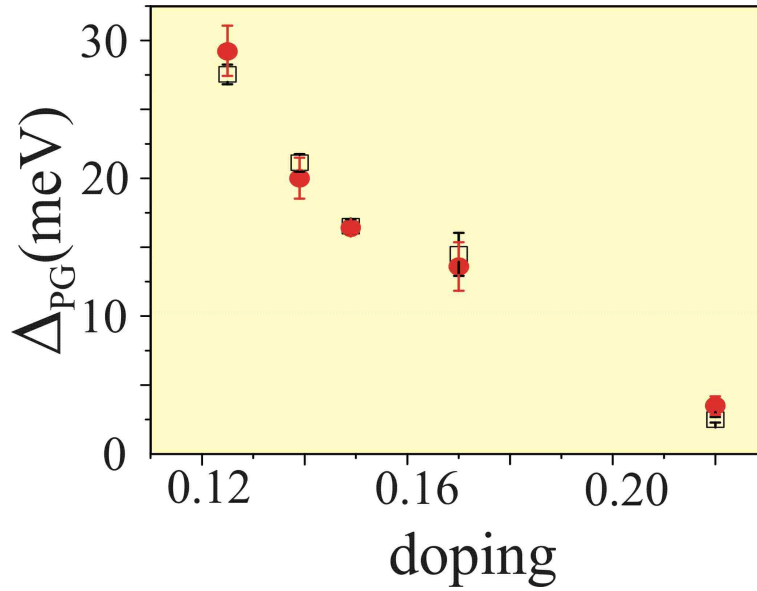


Figure 4.12: *Doping dependence of pseudogap extracted from DOS(circles) and d-wave valence bond order parameter(squares).*

#### 4.4.6 Quantitative Evaluation of the Glassy Bond Order and the Pseudogap

I have shown qualitative relations between the bond order parameter  $\chi_d$  and the strength of the pseudogap. With the doping dependence of the arc length and DOS gap size study, it is clear that the fluctuation of  $\chi_d$  is tied to the strength of the pseudogap. It is more convincing to establish this glassy bond order if I evaluate the order parameter more carefully and compare it with the size of the pseudogap. Fig. 4.12 demonstrates the connection more clearly.

Here I extract the size of the pseudogap in two different ways: the first way is to directly measure it from the integrated density of states calculation; The

other way is to calculate it from the order parameter following the relation:

$$\Delta_{pg} \simeq (J/8) \times \sqrt{\sum_i (\sum_j g_{ij}^x \chi_{ij} d_{ij})^2 / N_s} \quad (4.15)$$

It is clear that the results from these two methods are consistent with each other. This method is also used later to plot a phase diagram. From the doping dependence of the pseudogap size, I can see that without the presence of superconducting order, the valence bond glass gives us an increasing gap in energy scale with decreasing doping. Obviously the pseudogap is a separate energy scale in addition to the superconducting energy scale. This has been reported by ARPES performing a doping dependence study [21]. They find that the antinodal gaps and the nodal gaps show different trends with increasing doping. In earlier temperature and angular dependence studies [133] it has been hard to reconcile the differently positioned gaps emerging at different temperatures on the same sheet of the Fermi surface. Since they are not opening up at the same temperature they do not comprise a single gap. Instead they must be thought of as two distinct gaps.

Also Raman scattering has shown clear evidence for two gaps [33] as discussed previously. Having already established that the pseudogap and the superconducting gap have two distinct energy scales it is now useful to study the interplay between these two gaps. There are theories such as a bipolaron theory [134] which can also produce two energy gaps with distinct temperature dependence: one gap opens at  $T_c$  following BCS theory and the other is across  $T_c$ . It requires the two gaps to add in quadrature. However, it is contradicting with the angular dependence ARPES study in the underdoped Bi2212 where clearly there is no such quadrature relation.

## 4.5 Superconducting Phase

To examine the interplay between these two channels (both driven by the same superexchange  $J$ ) I now turn on the superconducting channel. Below  $T_c$  the glassy valence bond charge density waves coexist and compete with the inhomogeneous d-wave superconducting pairs. The present theory predicts two spectral gaps, originating from the particle-hole and particle-particle channels of the valence bond fluctuations, respectively. The Gutzwiller renormalization factors are identical  $g_{ij}^X = g_{ij}^\Delta$  at half filling, reflecting the  $SU(2)$  symmetry from the spin degrees of freedom. At finite doping concentrations, the charge fluctuations will break the balance. In particular, the pair-breaking effects induced by inter-site Coulomb repulsion  $V$  will effectively weaken the singlet pairing channel as compared to the paramagnetic density wave channel[119]. As a result, the pairing channel is suppressed at a fixed doping compared to its counterpart with zero Coulomb repulsion ( $V = 0$ ). The critical doping, where the pairing order vanishes, gets pushed back to a smaller value compared to its counterpart as well. Here I am only considering strong electron-electron correlations. However, more surveys show that the effects of the electron-phonon interaction cannot be overlooked either. It is reported that the electron-phonon interactions promote the d-wave charge density wave [60] [61]. Equivalently, the competing pairing channel is weakened due to the electron phonon interaction. To incorporate these effects into the renormalized mean field theory in Eq. 4.7, I use

$$\begin{aligned} g_{ij}^X &= g_{ij}^J \\ g_{ij}^\Delta &= pg_{ij}^J \end{aligned} \tag{4.16}$$

where  $p = 0.475$ .  $p$  is a phenomenological parameter which separates the two energy gap scales in the underdoped regime. With the coexistence of the glassy bond order and the superconducting order, the real space and the

momentum space properties are investigated to make connection with the STM and ARPES experiments. The competing nature of these two orders manifest themselves into the distinctive spatial, momentum, temperature and doping dependence in the underdoped regime. Thorough investigation is presented to show the supportive evidence for the two-gap scenario.

### 4.5.1 The First Glance of the Coexistence of Two Gaps

In Fig 4.13(a), the  $T=0$  integrated density of states is shown at doping  $x = 0.14$ . It clearly displays two gaps in agreement with STM experiments on  $La - Bi2201$  [26][22], the smaller superconducting gap  $\Delta_{sc} \simeq 10meV$  represents the spin singlet pairing and a large pseudogap  $\Delta_{pg} \simeq 22meV$  inherited from the normal state. Both gaps exhibit doping induced spatial inhomogeneity accompanied by the distributions of the corresponding order parameters  $(\Delta_d, \chi_d)$ (see Fig 4.13(b)). The gaps scale according to  $G_{pg} \sim \sqrt{\sum_i (\sum_j g_{ij}^x \chi_{ij} d_{ij})^2 / N_s}$  and  $G_{sc} \sim \sum_{ij} \Delta_{ij} \tau_{ij}^d / N_s$  respectively. We can see they both follow approximately the Gaussian distribution as a manifestation of the disorder nature of the system. The ARPES and STM results on very underdoped  $La - Bi2201$  both show the coexistence of a small gap and a big gap, as shown in Fig. 4.13(c)(d)(e). The coexistence of two gaps is also observed in underdoped  $Bi_2Sr_2Ca_{1-x}Y_xCu_2O_{8+\delta}(Bi - 2212)$  with  $T_c = 50K$ . [135].

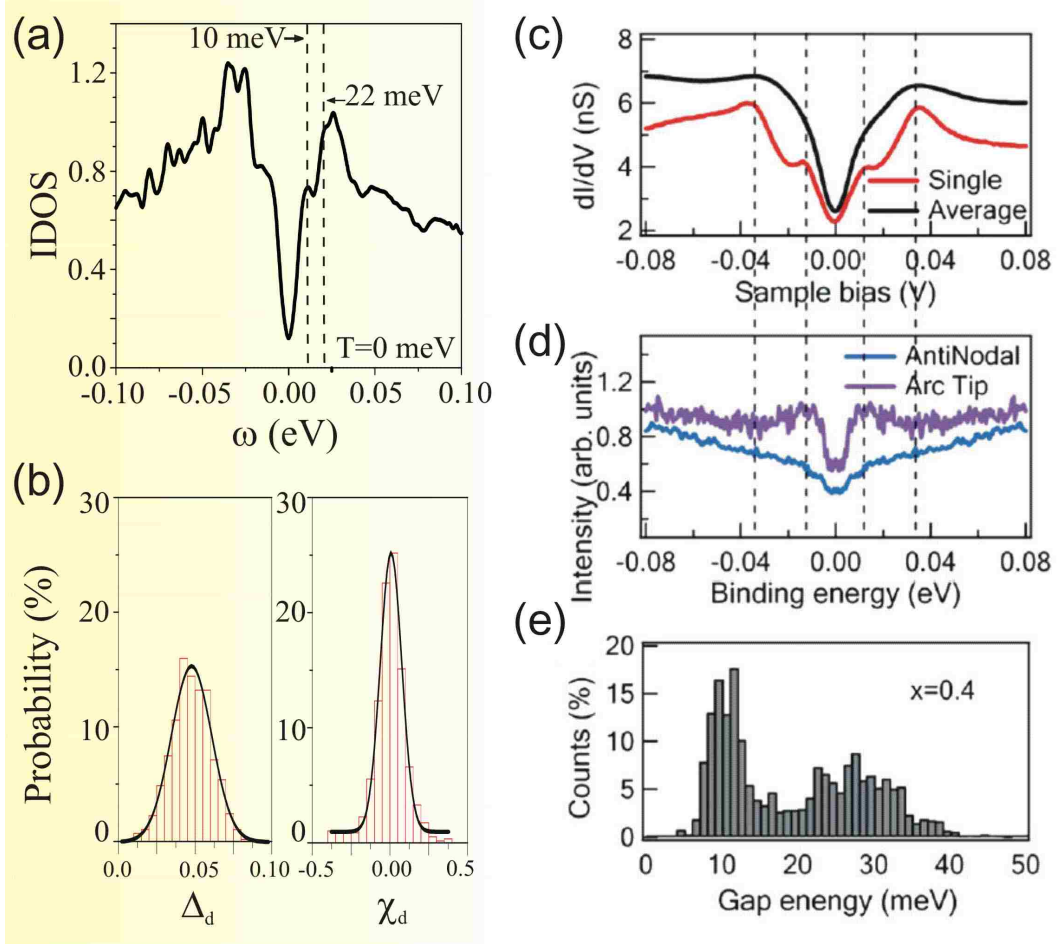


Figure 4.13: (a) The average density of states showing the coexistence of the pseudogap and the superconducting gap at doping  $x = 0.14$ . The pseudogap is the larger gap with the size being approximately 22 meV and the small gap is the superconducting gap with the size being approximately 10 meV. (b) The histogram of  $\Delta_d$  and  $\chi_d$ . They both follow the Gaussian distribution. (c)(d)(e) are experimental results on  $Bi_2Sr_{2-x}La_xCuO_{6+x}$  when  $x = 0.4$ , [22], they all show the coexisting of the two gaps. (c) Single STM spectrum (red) representative of the average small gaps and large gaps and a spatially averaged STM spectrum (black) from a  $240 \text{ \AA}$   $dI/dV$  map. (d) Symmetrized ARPES energy distribution curves (EDCs) taken at antinodal positions and at the arc tip near the antinodal region ( $\phi = 21^\circ$ ). (e) Gap histogram ( $237 \text{ A}^\circ$   $dI/dV$  map) with average small gap at  $10.50 \text{ meV} \pm 2.8 \text{ meV}$  and large gap average at  $27.2 \text{ meV} \pm 5.4 \text{ meV}$ .

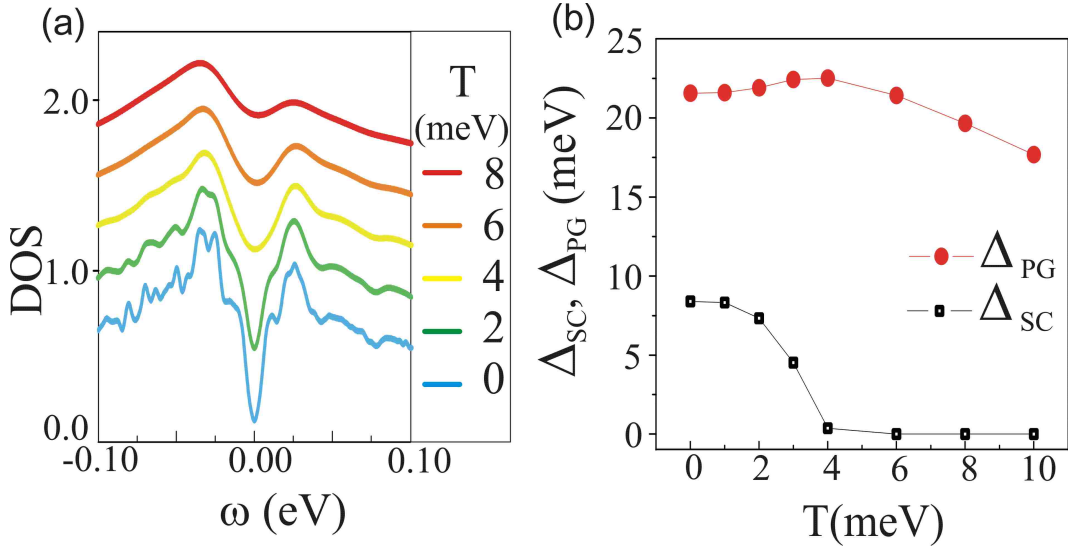


Figure 4.14: (a) Average density of states showing the temperature evolution of the superconducting gap and the pseudogap from  $T = 0\text{meV}$  to  $T = 8\text{meV}$ ,  $T_c = 4\text{meV}$ . (b) Temperature dependence of the superconducting gap size and the pseudogap size.

## 4.5.2 Temperature Dependence of the Pseudogap and the Superconducting Gap

I calculate the temperature evolution of the density of states shown in Fig. 4.14 by minimizing the free energy. The superconducting gap and the coherence peaks vanish above  $T_c \sim 4\text{meV}$ .  $T_c$  is determined by the vanishing pairing order parameter upon raising the temperature. As the system enters the pseudogap phase  $T > T_c$ , the large gap remains and behaves like a normal pseudogap with thermal filling upon further increasing temperature. Interestingly, as  $T$  is increased toward  $T_c$ , the pairing gap and the pseudogap show opposite temperature dependence, a typical feature of coexisting but competing order ( Fig. 4.14).

### 4.5.3 The Momentum Dependence of the Two Coexisting Gaps

To study the the momentum anisotropy of the two gaps, I calculated the single-particle spectral function  $A(k, \omega)$  as measured by ARPES. Fig. 4.15 shows the symmetrized energy distribution curve (EDC) on the underlying Fermi surface around the three characteristic locations: on the normal state Fermi arc near the nodes, at the tip of the Fermi arc, and near the antinode. A single gap due to d-wave pairing is seen on the Fermi arc which closes at  $T_c$ , but with signatures of an emerging pseudogap just above  $T_c$  which is filled up at moderately higher temperatures. The EDC becomes qualitatively different near the antinodes and exhibits coexisting pairing and the valence bond density wave gap at low temperatures. Thus, the theory predicts that d-wave pairing extends beyond the Fermi arc into the antinodal regime. This is a consequence of the softness of the normal state pseudogap discussed above which allows pairing of the antinodal state near the Fermi level below the gap energy. The pairing gap and the coherence peaks disappear above  $T_c$  as the system transitions into the normal state pseudogap phase. Although the large incoherent background and inelastic life time broadening observed by ARPES tend to suppress the coherent peaks and mask the pairing gap near the antinode, recent high resolution ARPES experiments performed on  $La - Bi2201$  indeed observed the pairing gap near the antinodes. [22][136].

Extracting the gap values from the spectral function, I plot the angular dependence of the pairing gap and the pseudogap in Fig. 4.16. It clearly displays the evolution of the d-wave pairing gap along the Fermi arc and the coexistence of the pairing and valence bond charge density wave gap off the arc. In general, I do not see a single gap formed by the quadrature of two underlying gaps because the origin of the two gaps are in the particle-particle and the particle-hole channels respectively. It is in good agreement with ARPES and Raman [33] experiments. It suggests that the d-wave pairing gap along the

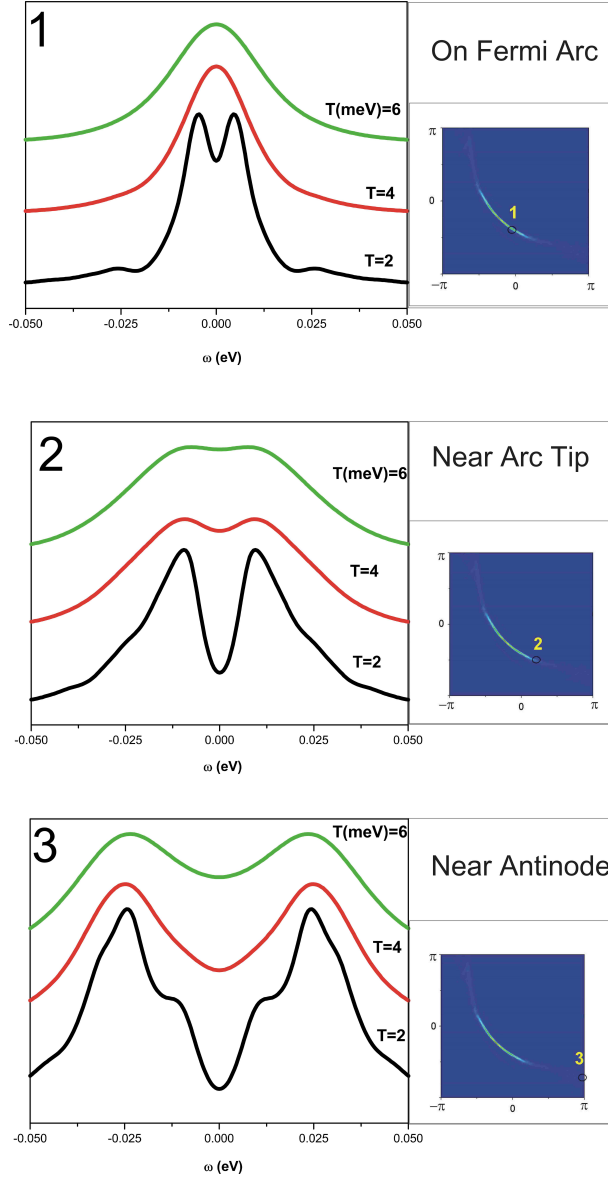


Figure 4.15: *Symmetrized spectral function at different locations in momentum space at three temperatures:  $T = 2\text{meV}$ ,  $T = 4\text{meV}$ ,  $T = 6\text{meV}$ , at doping  $x = 0.14$ ,  $T_c = 4\text{meV}$ . Location (1) on Fermi arc near the nodal region. Single  $d$ -wave pairing gap disappearing above  $T_c$ . (2) Near arc tip. Similar  $d$ -wave pairing gap and VBG pseudogap surviving above  $T_c$  (3) Near antinode. Coexisting large pseudogap and  $d$ -wave pairing gap below  $T_c$ .*

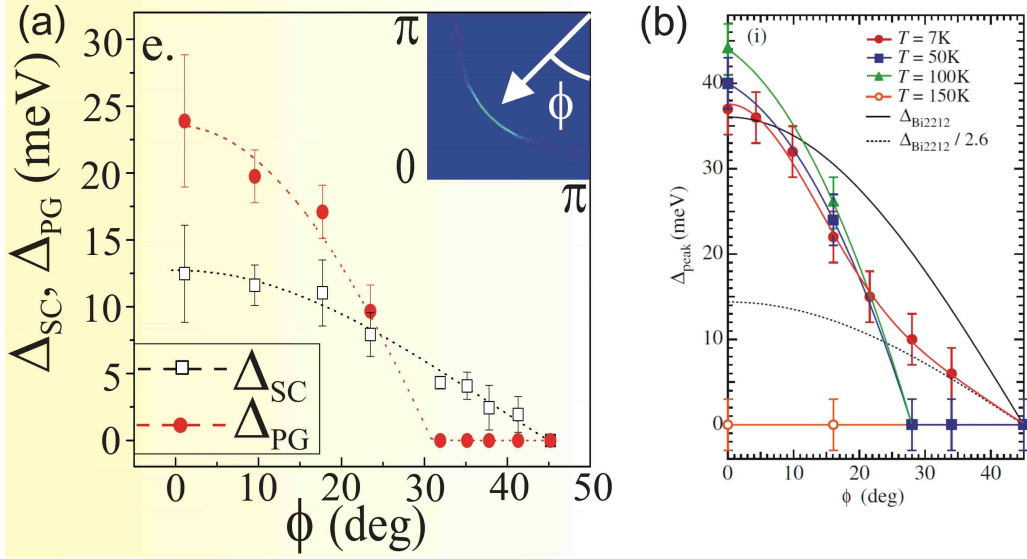


Figure 4.16: (a) Angular dependence of the superconducting gap and pseudogap. The angle  $\phi$  is defined in the insert. On the Fermi arc there is one single  $d$ -wave superconducting gap opens up in the BCS manner. From the arc tip to the antinodal region, two gaps are resolved to follow different trends while they both grow in value. A smaller gap continues to open up in the BCS manner and a bigger gap which emerges right off the arc tip and develops towards the antinodal region with a more dramatic increase (b) Angular  $\phi$  dependence of peak position of the symmetrized EDC ( $\Delta_{peak}$ ). Solid black line shows  $\Delta_{peak}$  for optimally doped Bi2212 [ $\Delta_{Bi2212} / \cos(2\phi)$ ]. Dashed black line shows  $\Delta_{Bi2212}$  divided by 2.6 [ $\approx T_c(Bi2212) / T_c(Bi2201) = 90K / 35K$ ].

Fermi arc evolves into the coexisting pairing and valence bond charge density wave gaps off the arc (when they are resolved). This can be compared very well with Kondo et al.'s result[73], on  $(Bi, Pb)_2(Sr, La)_2CuO_{6+\delta}$  (Bi2201), which has a low transition temperature  $T_c \sim 35$  K at optimal doping, where  $T_c$  is almost 3 times smaller than (Bi2212). In Bi2201 the superconducting gap and the pseudogap are well separated (see Fig. 4.16). Below the superconducting transition temperature the angular dependence of the gap deviates away from a single  $d_{x^2-y^2}$  once it is off the arc. In the antinodal region the value is much higher than just the extrapolated  $d$ -wave dependence of  $T_c$ .

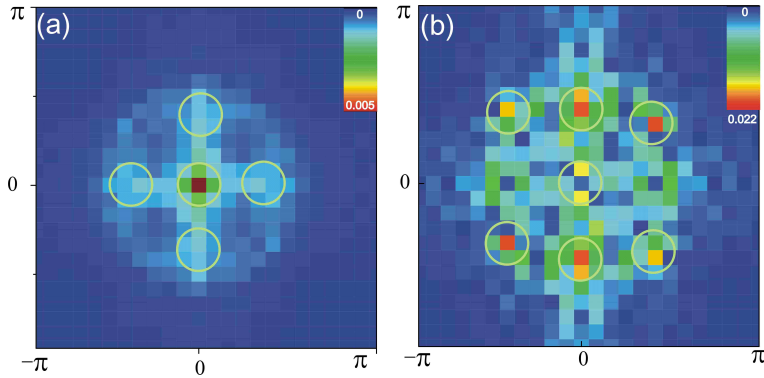


Figure 4.17: *Fourier transform of the power spectrum of (a) the pairing channel  $\Delta_d(q)$  and (b) the bond channel  $\chi_d(q)$  of one specific sample at doping  $x = 0.14$  in the coexisting phase.*

Thus the ground state below  $T_c$  is a coexisting state of glassy d-wave valence bond density waves and superconducting pairing, a mixture of a quantum paramagnet and spin singlets. They are competing with each other although they are driven by the same superexchange  $J$ . There are traces of glassy valence bond density waves in the pairing gap and pairing in the valence bond density wave gap near the antinodes. To uncover the finite- $q$  feature in the pairing channel and the bond channel, I plot the power spectrum of the Fourier transformed d-wave pairing order parameter  $\Delta_d(q)$  and the glassy bond order parameter  $\chi_d(q)$  in the coexisting phase in Fig. 4.17. In Fig. 4.17(a),  $\Delta_d(q)$  shows a bright spot at zero  $q$ . In addition to the main contribution at  $q = 0$  there are four very weak subdominant peaks representing finite-momentum pairing at  $|q|^*$  connecting the antinodal Fermi surface section. On the other hand, in the plot of  $\chi_d(q)$  there are several dominant  $\mathbf{q}$ s which show a clear tendency of disordered nematic patterns at finite wavevectors.

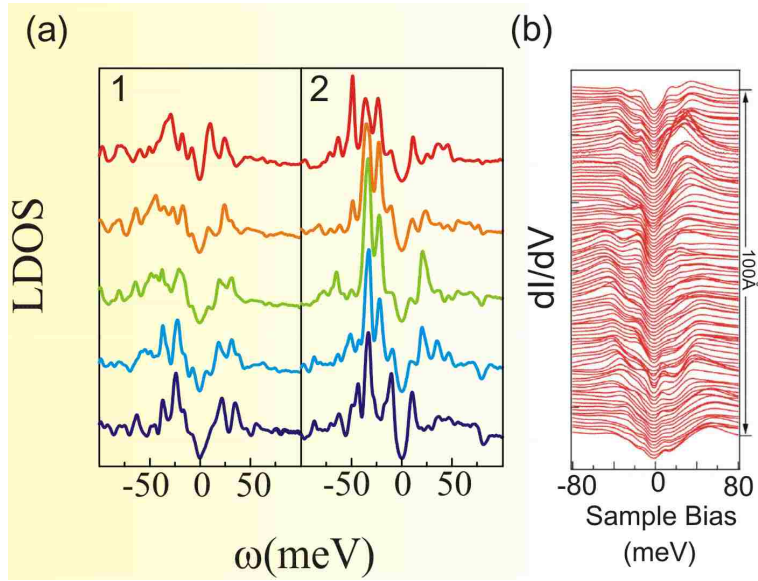


Figure 4.18: (a) Local density of states plot along two linecuts. The linecuts are chosen in the region where the local doping is around underdoped to the optimal doped range in order to see a well separated superconducting gap and pseudogap (b) Spectra along a  $100 \text{ \AA}$  line on underdoped  $\text{Bi}_2\text{Sr}_{2-x}\text{La}_x\text{CuO}_{6+x}$  (La-Bi2201) when La doping is  $x = 0.4$  [22])

#### 4.5.4 The Spatial Dependence of the Two Gaps

In order to see the two gaps directly in real space, like that which is measured by STM, I have calculated the the local density of states (LDOS) along two linecuts on one sample at the doping concentration  $x = 0.14$  shown in Fig. 4.18. The evolution of the line shape agrees with the STM conductance spectra [26][22]. There is one small gap which has a coherent peak representing the spin singlet pairing inside a large broader gap which is attribute to the pseudogap. Both the small gap and large gap are spatially inhomogeneous.

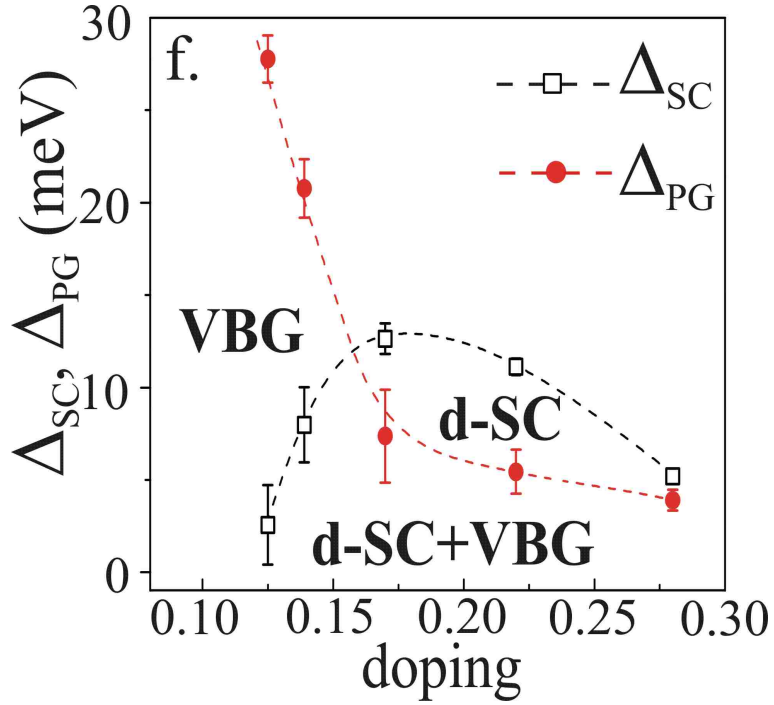


Figure 4.19: Superconducting gap  $\Delta_{SC}$  and pseudogap  $\Delta_{PG}$  as a function of doping

#### 4.5.5 The Theoretical Phase Diagram

In summary, due to the strong electronic correlation the valence bond fluctuations are strong and can be pinned by the disordered screened dopant potential. The quasiparticle pairing from the particle-particle channel and the incommensurate bond centered charge density waves from the particle hole channel are the key ingredients for understanding the superconducting and the pseudogap phases of the cuprates. I present a unified theory of glassy valence bond charge density wave describing the most essential features of the pseudogap phenomena and electronic disorder. I construct a theoretical phase diagram (see Fig. 4.19) using the doping dependence of the d-wave pairing gap and the pseudogap. It clearly captures the basic topology of the global phase diagram of the high  $T_c$  cuprates. In particular the dop-

ing dependence of the two gaps are opposite in the underdoped regime, but become similar in the overdoped part of the phase diagram. Although the present theory does not involve a precursor pairing induced pseudogap above  $T_c$ , it does not rule out such a possibility when fluctuation effects beyond the Gutzwiller projection are taken into account. However, it is likely that the partial gapping of the Fermi surface due to the glassy valence bond density wave order can account for most parts of the large Nernst signal at  $T_c$ . It is conceivable that suppression in the electronic disorder induced glassy valence bond order in the paramagnetic channel is a useful way to increase the superconducting transition temperature  $T_c$ .

# Appendix A

## From Hubbard Model to t-J Model

In the strongly-coupling limit the Hubbard model can reduce to t-J model[137][138]. The derivation follows P.Fulde's notation [139], and more detailed algebra can be found in reference [140]. Starting from the Mott insulator, there are three bands at present: the lower Hubbard band, the oxygen 2p band and the upper Hubbard band (see Figure 2.2). In order to consider the charge transfer insulator nature of the cuprate parent compounds the oxygen 2p band can be treated as the lower hubbard band and  $\Delta$  becomes  $U_{eff}$  in the Hubbard Model when  $\Delta$  is large enough.

The Hubbard model Hamiltonian can be written into two parts, the hopping part and the interaction part.

$$\begin{aligned} H &= - \sum_{i,j,\sigma} t_{ij} C_{i\sigma}^\dagger C_{j\sigma} + U \sum_i n_{i\uparrow} n_{i\downarrow} \\ H &= H_t + H_U \end{aligned} \tag{A.1}$$

There is a hopping matrix element  $t_{ij}$  between different sites and potential  $U$  on the same site (for the purpose of simplicity I limit the hopping to the

nearest neighbor  $t_{ij} \equiv t$ ). The strong coupling limit is when  $U$  is large in comparison with the system bandwidth, in this case  $U \gg t$ . The Hilbert space can be divided into two subspaces:  $P$  denotes states with no double occupancy, and  $Q$  denotes states with double occupancy .

$$\begin{aligned} H|\Psi\rangle &= H|\Psi\rangle \\ |\Psi\rangle &= |\Psi_p\rangle + |\Psi_Q\rangle \end{aligned} \quad (\text{A.2})$$

I write the Hamiltonian into four blocks. These four blocks act on different states.  $H_{PP}$  and  $H_{QQ}$  act within the subspace  $P$  and  $Q$ , respectively.  $H_{PQ}$  and  $H_{QP}$  connect these two.

$$\begin{aligned} H_{PP}|\Psi_p\rangle + H_{PQ}|\Psi_Q\rangle &= E|\Psi_p\rangle \\ H_{QP}|\Psi_p\rangle + H_{QQ}|\Psi_Q\rangle &= E|\Psi_Q\rangle \end{aligned} \quad (\text{A.3})$$

Simple algebra will give us the effective Hamiltonian for  $|\Psi_p\rangle$  and  $|\Psi_Q\rangle$  respectively (see Equation. A.5). This Schriffer-Wolff Transformation makes it possible to just work on the subspace  $P$  only and the doubly occupied subspace  $Q$  can be omitted from now on. I denote the effective Hamiltonian to be  $\tilde{H} = \tilde{H}_{PP}$ .

$$\begin{aligned} \tilde{H}_{PP}|\Psi_P\rangle &= E|\Psi_p\rangle \\ \tilde{H}_{QQ}|\Psi_Q\rangle &= E|\Psi_Q\rangle \end{aligned} \quad (\text{A.4})$$

$$\begin{aligned} \tilde{H}_{PP} &= H_{PP} - H_{PQ} \frac{1}{H_{QQ} - E} H_{QP} \\ \tilde{H}_{QQ} &= H_{QQ} - H_{QP} \frac{1}{H_{PP} - E} H_{PQ} \end{aligned} \quad (\text{A.5})$$

I define  $P$  to be a projection operator which projects states into reduced Hilbert space. It follows  $P = \prod_i (1 - n_{i\downarrow} n_{i\uparrow})$  and  $Q = 1 - P$  is the projector which projects onto the space of configurations with doubly occupied states. The effective Hamiltonian can be written as :

$$\tilde{H} = PHP - PHQ \frac{1}{QHQ - E} QHP \quad (\text{A.6})$$

Also in the limit of large  $U$ , I can approximate  $QHQ \approx U$ , and expanding gives A.7

$$\frac{1}{QHQ - E} \simeq \frac{1}{U - E} = \frac{1}{U} (1 + \frac{E}{U} + \dots) \simeq \frac{1}{U} \quad (\text{A.7})$$

The effective Hamiltonian in the limit of large  $U$  is

$$\tilde{H} = PHP - \frac{1}{U} PHQQHP \quad (\text{A.8})$$

From the definition of  $P$  and  $Q$ , I get the following relations:

$$\begin{aligned} PHP &= -t \sum_{ij\sigma} (1 - n_{i\bar{\sigma}}) c_{i\sigma}^\dagger c_{j\sigma} (1 - n_{j\bar{\sigma}}) \\ QHQ &= -t \sum_{ij\sigma} n_{i\bar{\sigma}} c_{i\sigma}^\dagger c_{j\sigma} n_{j\bar{\sigma}} \\ QHP &= -t \sum_{ij\sigma} n_{i\bar{\sigma}} c_{i\sigma}^\dagger c_{j\sigma} (1 - n_{j\bar{\sigma}}) \\ PHQ &= -t \sum_{ij\sigma} (1 - n_{i\bar{\sigma}}) c_{i\sigma}^\dagger c_{j\sigma} n_{j\bar{\sigma}} \end{aligned} \quad (\text{A.9})$$

I define the hole operator in analogy with the electron operator

$$\begin{aligned} \hat{c}_{i\sigma}^\dagger &= c_{i\sigma}^\dagger (1 - n_{i\bar{\sigma}}) \\ \hat{c}_{i\sigma} &= c_{i\sigma} (1 - n_{i\bar{\sigma}}) \end{aligned} \quad (\text{A.10})$$

After some algebra, I get the effective Hamiltonian, A.11

$$\begin{aligned}
\tilde{H} &= H_1 + H_2 + H_3 \\
H_1 &= -t \sum_{\langle ij \rangle \sigma} (\hat{c}_{i\sigma}^\dagger \hat{c}_{j\sigma} + h.c.) \\
H_2 &= -\frac{2t^2}{U} \sum_{\langle ijk \rangle \sigma} (n_{i\sigma} n_{j\bar{\sigma}} - c_{i\sigma}^\dagger c_{i\bar{\sigma}} c_{j\bar{\sigma}}^\dagger c_{j\sigma}) \\
H_3 &= -\frac{t^2}{U} (c_{i\sigma}^\dagger n_{j\bar{\sigma}} \hat{c}_{k\sigma} - c_{i\sigma}^\dagger c_{j\bar{\sigma}}^\dagger c_{j\sigma} \hat{c}_{k\bar{\sigma}} + h.c.) \tag{A.11}
\end{aligned}$$

The 3-site term  $H_3$  is usually not considered to be important, so it can be ignored from now on.  $H_2$  can be written into a more conventional form using the spin operator  $\mathbf{S}_i = \frac{1}{2} \sum_{\alpha\beta} c_{i\alpha}^\dagger \boldsymbol{\sigma}_{\alpha\beta} c_{i\beta}$ , where  $\boldsymbol{\sigma}$  is the Pauli matrix of a spin  $\frac{1}{2}$ .

$$\mathbf{S}_i \cdot \mathbf{S}_j - \frac{1}{4} n_i n_j = -\frac{1}{2} (n_{i\sigma} n_{j\bar{\sigma}} - c_{i\sigma}^\dagger c_{i\bar{\sigma}} c_{j\bar{\sigma}}^\dagger c_{j\sigma}) \tag{A.12}$$

Finally the t-J model arises:

$$\begin{aligned}
H_{tj} &= -t \sum_{\langle ij \rangle \sigma} (\hat{c}_{i\sigma}^\dagger \hat{c}_{j\sigma} + h.c.) \\
&\quad + J \sum_{\langle i,j \rangle \sigma} (\mathbf{S}_i \cdot \mathbf{S}_j - \frac{1}{4} n_i n_j) \tag{A.13}
\end{aligned}$$

This is exactly the same t-J model that was derived in chapter 2.

# Bibliography

- [1] W. Meissner and R. Ochsenfeld, *Naturwissenschaften* (1933).
- [2] F. H. London, *Proc. Roy. Soc.* **A149**, 71 (1935).
- [3] V. Ginzburg and L. Landau, *Zh. Eksp. Teor. Fiz.* **20** (1950).
- [4] J. Bardeen, L. N. Cooper, and J. R. Schrieffer, *Phys. Rev.* **108**, 1175 (1957).
- [5] W. S. Corak, B. B. Goodman, C. B. Satterthwaite, and A. Wexler, *Phys. Rev.* **96**, 1442 (1954).
- [6] J. G. Bednorz and K. A. Müller, *Z. Physik, B* **64**, 189 (1986).
- [7] M. K. Wu *et al.*, *Phys. Rev. Lett.* **58**, 908 (1987).
- [8] W. L. McMillan, *Phys. Rev.* **167**, 331 (1968).
- [9] Y. Kamihara, T. Watanabe, M. Hirano, and H. Hosono, *J. Am. Chem. Soc.* **130**, 3296 (2008).
- [10] N. F. Mott, *Proc. Phys. Soc.* **A**, 416 (1949).
- [11] W. W. Warren *et al.*, *Phys. Rev. Lett.* **62**, 1193 (1989).
- [12] R. E. Walstedt *et al.*, *Phys. Rev. B* **41**, 9574 (1990).
- [13] H. Alloul, *Phys. Rev. Lett.* **63**, 689 (1989).
- [14] M. Takigawa *et al.*, *Phys. Rev. B* **43**, 247 (1991).
- [15] K. Ishida *et al.*, *Phys. Rev. B* **58**, R5960 (1998).
- [16] D. C. Johnston, *Phys. Rev. Lett.* **62**, 957 (1989).
- [17] W. S. Lee *et al.*, *Nature* **450**, 81 (1996).
- [18] D. S. Marshall *et al.*, *Phys. Rev. Lett.* **76**, 4841 (1996).
- [19] A. G. Loeser *et al.*, *Science* **273**, 325 (1996).
- [20] M. R. Norman *et al.*, *Nature* **392**, 157 (1998).
- [21] K. Tanaka *et al.*, *Science* **314**, 1910 (2006).
- [22] J.-H. Ma *et al.*, *Phys. Rev. Lett.* **101**, 207002 (2008).
- [23] J. Bardeen, *Phys. Rev. Lett.* **6**, 57 (1961).
- [24] C. Renner, B. Revaz, J. Y. Genoud, and O. Fischer, *Journal of Low Temperature Physics* **105**, 1083 (1996).

- [25] M. Vershinin *et al.*, Science **303**, 1995 (2004).
- [26] M. C. Boyer *et al.*, Nature Physics **3**, 802 (2007).
- [27] K. K. Gomes *et al.*, Nature **447**, 569 (2007).
- [28] Y. Kohsaka *et al.*, Nature **454**, 1072 (2008).
- [29] Y. Kohsaka *et al.*, Science **315**, 1380 (2007).
- [30] J. W. Loram, K. A. Mirza, J. R. Cooper, and W. Y. Liang, Phys. Rev. Lett. **71**, 1740 (1993).
- [31] J. W. Loram, K. A. Mirza, J. R. Cooper, W. Y. Liang, and J. M. Wade, Journal of Superconductivity **7**, 243 (1994).
- [32] F. Slakey, M. V. Klein, J. P. Rice, and D. M. Ginsberg, Phys. Rev. B **42**, 2643 (1990).
- [33] M. Tacon *et al.*, Nature Physics **2**, 537 (2006).
- [34] F. C. Zhang and T. M. Rice, Phys. Rev. B **37**, 3759 (1988).
- [35] M. Platé *et al.*, Phys. Rev. Lett. **95**, 077001 (2005).
- [36] B. Vignolle *et al.*, Nature **455**, 952 (2008).
- [37] M. R. N. D. P. C. Kallinc, Advances in Physics **54**, 715 (2005).
- [38] T. Timusk and B. Statt, Rep. Prog. Phys. **62**, 61 (1998).
- [39] M. R. Norman, A. Kanigel, M. Randeria, U. Chatterjee, and J. C. Campuzano, Phys. Rev. B **76**, 174501 (2007).
- [40] S. A. K. V. J. Emery, Nature **374**, 434 (2002).
- [41] N. Trivedi and M. Randeria, Phys. Rev. Lett. **75**, 312 (1995).
- [42] G. Kotliar and J. Liu, Phys. Rev. B **38**, 5142 (1988).
- [43] M. Franz and A. J. Millis, Phys. Rev. B **58**, 14572 (1998).
- [44] A. V. Chubukov, M. R. Norman, A. J. Millis, and E. Abrahams, Phys. Rev. B **76**, 180501 (2007).
- [45] Y. Wang *et al.*, Phys. Rev. B **64**, 224519 (2001).
- [46] Y. Wang *et al.*, Phys. Rev. Lett. **88**, 257003 (2002).
- [47] Y. Wang *et al.*, Science **299**, 86 (2003).
- [48] Y. Wang *et al.*, Phys. Rev. Lett. **95**, 247002 (2005).
- [49] P. A. Lee and X.-G. Wen, Phys. Rev. B **63**, 224517 (2001).
- [50] S.-C. Zhang, Science **275**, 1089 (1997).
- [51] X.-G. Wen and P. A. Lee, Phys. Rev. Lett. **76**, 503 (1996).
- [52] S. A. Kivelson *et al.*, Rev. Mod. Phys. **75**, 1201 (2003).
- [53] A. Kanigel *et al.*, Nature Physics , 447 (2006).
- [54] A. Kanigel *et al.*, Phys. Rev. Lett. **99**, 157001 (2007).
- [55] I. Affleck and J. B. Marston, Phys. Rev. B **37**, 3774 (1988).
- [56] G. Kotliar, Phys. Rev. B **37**, 3664 (1988).
- [57] S. Chakravarty, R. B. Laughlin, D. K. Morr, and C. Nayak, Phys. Rev.

- B **63**, 094503 (2001).
- [58] C. M. Varma and L. Zhu, Phys. Rev. Lett. **98**, 177004 (2007).
  - [59] P. A. Lee, N. Nagaosa, and X.-G. Wen, Rev. Mod. Phys. **78**, 17 (2006).
  - [60] T. C. C. Newns, D. M., Nat Phys **3**, 184 (2007).
  - [61] J.-X. Li, C.-Q. Wu, and D.-H. Lee, Phys. Rev. B **74**, 184515 (2006).
  - [62] J. Schmalian, D. Pines, and B. Stojković, Phys. Rev. Lett. **80**, 3839 (1998).
  - [63] B. Kyung *et al.*, Phys. Rev. B **73**, 165114 (2006).
  - [64] C. Li, S. Zhou, and Z. Wang, Phys. Rev. B **73**, 060501 (2006).
  - [65] S. Sachdev, Rev. Mod. Phys. **75**, 913 (2003).
  - [66] K.-Y. Yang, T. M. Rice, and F.-C. Zhang, Phys. Rev. B **73**, 174501 (2006).
  - [67] T. D. Stanescu, P. Phillips, and T.-P. Choy, Phys. Rev. B **75**, 104503 (2007).
  - [68] T. D. Stanescu and G. Kotliar, Phys. Rev. B **74**, 125110 (2006).
  - [69] P. Phillips, Annals of Physics **321**, 1634 (2006), July 2006 Special Issue.
  - [70] A. J. Millis and M. R. Norman, Phys. Rev. B **76**, 220503 (2007).
  - [71] T. M. R. Wei-Qiang Chen, Kai-Yu Yang and F. C. Zhang, EuroPhys Lett **82**, 17004 (2008).
  - [72] G. Deutscher, Nature **397**, 410 (1997).
  - [73] T. Kondo, T. Takeuchi, A. Kaminski, S. Tsuda, and S. Shin, Phys. Rev. Lett. **98**, 267004 (2007).
  - [74] Y. Okada, T. Takeuchi, A. Shimoyamada, S. Shin, and H. Ikuta, Journal of Physics and Chemistry of Solids **69**, 2989 (2008), SNS2007, Spectroscopies in Novel Superconductors '07.
  - [75] M. L. Tacon, a. A. G. A. Sacuto, a. D. C. G. Kotliar, and Y. Gallais, and A. Forget, Nature Physics **2**, 537 (2006).
  - [76] V. J. Emery, Phys. Rev. Lett. **58**, 2794 (1987).
  - [77] C. M. Varma, S. Schmitt-Rink, and E. Abrahams.
  - [78] J. E. Hirsch, Phys. Rev. Lett. **59**, 228 (1987).
  - [79] H. F. Masao Ogata, Rep.Prog.Phys **71**, 036501 (2008).
  - [80] J. Zaanen, G. A. Sawatzky, and J. W. Allen, Phys. Rev. Lett. **55**, 418 (1985).
  - [81] P.W.Anderson, Science **235**, 1196 (1987).
  - [82] P. W. Anderson, Phys. Rev. **115**, 2 (1959).
  - [83] M. C. Gutzwiller, Phys. Rev. **137**, A1726 (1965).
  - [84] M. C. Gutzwiller, Phys. Rev. Lett. **10**, 159 (1963).

- [85] T. Ogawa, K. Kanda, and T. Matsubara, *Progress of Theoretical Physics* **53**, 614 (1975).
- [86] D. Vollhardt, *Rev. Mod. Phys.* **56**, 99 (1984).
- [87] T. M. R. F C Zhang, C Gros and H. Shiba, *Superconductor Science and Technology* **1**, 36 (1988).
- [88] Q.-H. Wang, Z. D. Wang, Y. Chen, and F. C. Zhang, *Phys. Rev. B* **73**, 092507 (2006).
- [89] C. Li, *Gutzwiller approximation in strongly correlated electron systems*, PhD thesis, Boston College, 2009.
- [90] I. Affleck, Z. Zou, T. Hsu, and P. W. Anderson, *Phys. Rev. B* **38**, 745 (1988).
- [91] P. W. Anderson *et al.*, *Journal of Physics: Condensed Matter* **16**, R755 (2004).
- [92] G. D.Mahan, *Many-Particle Physics* (, 2000).
- [93] M. Randeria *et al.*, *Phys. Rev. Lett.* **74**, 4951 (1995).
- [94] J.-C. C. Mohit Randeria, arXiv:cond-mat/9709107v1 (1997).
- [95] A. Damascelli, Z. Hussain, and Z.-X. Shen, *Rev. Mod. Phys.* **75**, 473 (2003).
- [96] Z. Wang, J. R. Engelbrecht, S. Wang, H. Ding, and S. H. Pan, *Phys. Rev. B* **65**, 064509 (2002).
- [97] J. M. Luttinger, *Phys. Rev.* **119**, 1153 (1960).
- [98] M. R. Norman and H. Ding, *Phys. Rev. B* **57**, R11089 (1998).
- [99] S. Zhou, H. Ding, and Z. Wang, *Phys. Rev. Lett.* **98**, 076401 (2007).
- [100] T. M. Rice and G. K. Scott, *Phys. Rev. Lett.* **35**, 120 (1975).
- [101] T. M. Rice and G. K. Scott, *Proceedings of the Physical Society* **80**, 489 (1962).
- [102] J. Lee *et al.*, *Science* **325**, 1099 (2009).
- [103] K. M. Shen and J. S. Davis, *Materials Today* **11**, 14 (2008).
- [104] C. Nayak, *Phys. Rev. B* **62**, 4880 (2000).
- [105] M. J. Lawler *et al.*, *Science* **466**, 347 (2010).
- [106] H. Yamase and H. Kohno, *Journal of the Physical Society of Japan* **69**, 2151 (2000).
- [107] H. Luo, L. Fang, G. Mu, and H.-H. Wen, *Journal of Crystal Growth* **305**, 222 (2007).
- [108] H. Eisaki *et al.*, *Phys. Rev. B* **69**, 064512 (2004).
- [109] K. Fujita, T. Noda, K. M. Kojima, H. Eisaki, and S. Uchida, *Phys. Rev. Lett.* **95**, 097006 (2005).
- [110] K. M. Shen *et al.*, *Science* **307**, 901 (2005).

- [111] S. H. Pan *et al.*, Nature **413**, 282 (2001).
- [112] C. Howald, P. Fournier, and A. Kapitulnik, Phys. Rev. B **64**, 100504 (2001).
- [113] K. M. Lang *et al.*, Nature **415**, 412 (2002).
- [114] K. McElroy *et al.*, Science **309**, 1048 (2005).
- [115] T. Hanaguri *et al.*, Nature **430**, 1001 (2004).
- [116] M. Vershinin *et al.*, Science **303**, 1995 (2004).
- [117] K. McElroy *et al.*, Phys. Rev. Lett. **94**, 197005 (2005).
- [118] K. McElroy *et al.*, Nature **422**, 592 (2003).
- [119] S. Zhou and Z. Wang, Phys. Rev. B **70**, 020501 (2004).
- [120] Q.-H. Wang and D.-H. Lee, Phys. Rev. B **67**, 020511 (2003).
- [121] D.-H. L. Henry C. Fu, J. C. Davis, arXiv:cond-mat/0403001v2 (2004).
- [122] H.-D. Chen, O. Vafek, A. Yazdani, and S.-C. Zhang, Phys. Rev. Lett. **93**, 187002 (2004).
- [123] Z. Tešanović, Phys. Rev. Lett. **93**, 217004 (2004).
- [124] P. W. Anderson, arXiv:cond-mat/0406038v1 (2004).
- [125] D. Podolsky, E. Demler, K. Damle, and B. I. Halperin, Phys. Rev. B **67**, 094514 (2003).
- [126] S. R. White and D. J. Scalapino, Phys. Rev. B **70**, 220506 (2004).
- [127] A. M. Tsvelik and A. V. Chubukov, Phys. Rev. Lett. **98**, 237001 (2007).
- [128] K. McElroy, Nat Phys **2**, 441 (2006).
- [129] M. Tarzia and G. Biroli, EPL **82**, 67008 (2008).
- [130] W. D. Wise *et al.*, Nat Phys **4**, 696 (2008).
- [131] S. Zhou and Z. Wang, Phys. Rev. Lett. **98**, 226402 (2007).
- [132] Y. L. et al, Nature **455**, 372 (2008).
- [133] W. S. Lee *et al.*, Nature **450**, 81 (2007).
- [134] A. S. Alexandrov and A. F. Andreev, arXiv:cond-mat/0005315v3 [cond-mat.supr-con]. .
- [135] I. M. Vishik *et al.*, arXiv:1009.0274v1 (2010).
- [136] J. Wei *et al.*, Phys. Rev. Lett. **101**, 097005 (2008).
- [137] J. S. K A Chao and A. M. Oles, Journal of Physics C: Solid State Physics **10**, L271 (1977).
- [138] C. Gros, R. Joynt, and T. M. Rice, Phys. Rev. B **36**, 381 (1987).
- [139] P. Fulde, *Electron Correlations in Molecules and Solids, Springer Series in Solid-State Sciences 100* (Springer-Verlag, 1991).
- [140] S. W. Haas, *Dynamical Properties of Strongly Correlated Fermionic System*, PhD thesis, The Florida State University, 1995.

★ This document was created in L<sup>A</sup>T<sub>E</sub>X★